

DEVELOPING NEW CHEMICAL-BASED SENSORS FOR THE DETECTION OF VOLATILE COMPOUNDS

MATTEO FOIS

A thesis submitted in partial fulfilment of the requirements of the University of the West of
England, Bristol for the degree of Master of Philosophy

Faculty of Health and Applied Science

May 2022

Summary

Abstract	4
Acronyms and Abbreviations	5
Acknowledgements	6
Chapter 1 - Introduction and aims of the work	7
1.1 Introduction	7
1.2 Volatile organic compounds (VOCs): definition and importance	8
<i>1.2.1 Importance of VOCs in environmental monitoring</i>	<i>9</i>
<i>1.2.2 Importance of VOCs in medical diagnosis</i>	<i>10</i>
<i>1.2.3 Importance of VOCs in safety applications: explosives detection</i>	<i>12</i>
1.3 Existing methods in VOCs detection	13
1.4 Metal Oxide Semiconductors (MOS) Gas Sensors	14
<i>1.4.1 Gas sensors: definition and classification</i>	<i>15</i>
<i>1.4.2 Zirconium Oxide (ZrO₂)</i>	<i>16</i>
<i>1.4.3 Europium-doped Zirconium Oxide (ZrO₂:Eu³⁺)</i>	<i>17</i>
<i>1.4.4 Tungsten Oxide (WO₃)</i>	<i>17</i>
<i>1.4.5 Zinc Oxide (ZnO).....</i>	<i>18</i>
<i>1.4.6 MOS nanoparticles gas sensors: working principles</i>	<i>19</i>
<i>1.4.7 Sensing mechanism for the n-type materials</i>	<i>22</i>
<i>1.4.8 Sensing mechanism for the p-type materials</i>	<i>23</i>
1.5 Cataluminescence (CTL)	24
<i>1.5.1 CTL: definition and overview</i>	<i>24</i>
<i>1.5.2 CTL-based gas sensors: an overview</i>	<i>26</i>
1.6. Multimodal sensing	27
1.7 . Aims of the work.....	28
Chapter 2 - Materials and Methods.....	29
2.1. Synthesis of zirconium oxide-based nanoparticles	29
<i>2.1.1 Synthesis of ZrO₂:Eu³⁺(5%)</i>	<i>29</i>
2.2. Volatile organic compounds (VOCs) and interferants.....	30
2.3. Volatiles concentration validation using Selected-ion mass spectroscopy (SIFT-MS).....	31
2.4 Nanoparticle characterisation	31
<i>2.4.1 Microscopy Techniques</i>	<i>31</i>
<i>2.4.2 X-Ray Diffraction</i>	<i>32</i>
<i>2.4.3 Spectroscopical techniques.....</i>	<i>32</i>
2.5 Sensor Preparation.....	33
2.6 Experimental.....	34

2.6.1 Heated metal oxide sensors	35
2.6.2 CTL measurements	37
2.6.3 UV-activated sensor	37
Chapter 3 - Results	39
3.1. Material Characterisation	39
3.1.1 X-Ray diffraction (XRD)	39
3.1.2 Transmission Electron Microscopy (TEM) and Scanning Electron Microscopy (SEM)	41
3.1.3 Energy Dispersive X-ray Analysis (EDX.)	44
3.1.4 Raman Spectroscopy, Photoluminescence and Cataluminescence	46
3.2 Concentration test: SIFT-MS	47
3.3. Sensing experiment: an overview	49
3.4 Zirconium oxide sensor (ZrO ₂)	53
3.4.1 ZrO ₂ - Resistance experiments	53
3.4.2 ZrO ₂ - Cataluminescence (CTL) experiments	60
3.5 Europium-doped zirconium oxide sensor (ZrO ₂ :Eu ³⁺ (5%))	70
3.5.1 ZrO ₂ :Eu ³⁺ (5%) - Resistance experiments	70
3.5.2 ZrO ₂ :Eu ³⁺ (5%) - Cataluminescence (CTL) experiments	75
3.6 Tungsten oxide sensor (WO ₃)	79
3.6.1 WO ₃ - Resistance experiments	79
3.6.2 WO ₃ - Cataluminescence (CTL) Experiments	81
3.7 Zinc oxide sensor (ZnO)	86
3.7.1 ZnO - Temperature activated resistance experiments	86
3.7.2 ZnO - UV-Light activated resistance experiments	92
Chapter 4 – Discussion	94
4.1 Introduction	94
4.2. Resistance	95
4.3 Cataluminescence (CTL)	99
4.4. Dual-modality	101
Chapter 5 - Conclusion	106
Chapter 6 Future Work	107
References	109
Index of Figures	122

Abstract

This research project aims to enhance the performance of a series of chemical-based sensor devices. In particular, metal oxide gas sensors. These materials are well known and primarily employed in several applications, thanks to their characteristic of interacting with volatile compounds, giving a response in terms of reversible change in the electrical resistance. Another exciting feature of metal oxide semiconductors, in particular rare earth-doped ones, is represented by their cataluminescence (a type of light emission when they interact with certain volatile compounds). We attempt to register simultaneously and combine the two different sensor responses (electrical resistance and light emission) to enhance sensor sensitivity and selectivity. This mode of operation can be defined as "dual-modality", and it represents a novel approach to sensor technology.

For this purpose, the first part of the research project involved the synthesis and the characterisation of metal oxide nanoparticles to be employed in the sensing experiments. Afterwards, the materials obtained were used as sensing elements in in-house made equipment, recording the electrical resistance and the cataluminescence simultaneously. We tested each material under investigation with the following volatile compounds: acetone, ethanol, hydrogen peroxide, nitroglycerine, ethylene glycol dinitrate, 2,3-dimethyl-2,3-dinitrobutane, 2,4-dinitrotoluene and triacetone triperoxide. The experiments were repeated at different sensor temperatures in the range of 150-400°C. These ensured a full screening of the operating conditions and, consequently, the possibility of identifying the best parameters to ensure optimal sensor performance.

The results obtained are encouraging in terms of sensor performances. In particular, the europium-doping of the zirconium oxide gas sensor allowed achieving a higher cataluminescence production, especially in the temperature range 250-275°C, and consequently a better sensor sensitivity. Recording the light emission simultaneously with the resistance response was shown to be very promising in terms of selectivity. If two given compounds showed a similar response in terms of resistance, discrimination is still possible thanks to their different cataluminescence response profiles.

This thesis work showed for the first time and promisingly the possibility of combining more than one response from a single sensor to enhance its performance. We found out that the dual-modality can increase the sensor's possibility to distinguish among different volatiles. Especially the doping with rare earth metals, such as europium, increased the general response and consequently, they represent a promising material for the employment of dual-modality sensing.

Acronyms and Abbreviations

Abbreviation	Definition
BBR	black-body radiation
CFCs	chlorofluorocarbons
CTL	cataluminescence
DM	Dual-modality
DMNB	2,3-dimethyl-2,3-dinitrobutane
DNT	2,4-dinitrotoluene
EDX	Energy Dispersive X-ray Analysis
EGDN	Ethylene glycol dinitrate
GC-MS	Gas Chromatography mass spectroscopy
HBFCs	hydro bromo fluorocarbons
HCFCs	hydrochlorofluorocarbons
HMEs	Home-made explosives
HMTD	Hexamethylene triperoxide diamine
HMX	1,3,5,7-Tetranitro-1,3,5,7-tetrazoctane
HPLC	High performances liquid chromatography
IMS	Ion-mobility spectrometry
MOX	Metal Oxide
NG	nitroglycerine
NOCs	Nitroaromatic compounds
ODSs	Ozone-depleting substances
ONP	Ortho Nitro Phenol
PCa	Prostate cancer
ppb	Part-per-bilion
ppm	Part-per-milion
PSA	Prostate-specific antigene
PTR-MS	Proton-transfer-reaction mass spectrometry
QTOF-MS	Quadrupole Time of Flight Mass Spectrometer
RDX	1,3,5-Trinitro-1,3,5-triazinane
SEM	Scanning Electron Microscopy
SIFT-MS	Selected ion-flow tube mass spectrometry
TATP	Triacetone triperoxide
TEM	Transmission Electric Microscopy
TNT	2,4,6-trinitrotoluene
UV	Ultraviolet
VOCs	Volatile organic compounds
WHO	World Health Organisation

Acknowledgements

I would like to express my appreciation and gratitude to all the beautiful people who accompanied me during this journey.

I thank my supervisor and friend Ben de Lacy Costello for all the help, the patience, the time and the wisdom he vested in me. Alongside I want to thank the other member of my supervisory team Norman Ratcliffe and Timothy Cox.

I want to thank David Patton and Sue Hula, The University of the West of England, for instruments usage and technical assistance relative to the Transmission Electron Microscopy, the Scanning Electron Microscopy and the Energy Dispersive X-ray Analysis. I would also like to thank Dr Mark Light, University of Southampton, for the X-Ray Diffraction data analysis. A special thank my colleagues Kelly, Phoebe, Ollie and Terry; it was great to be part of the team for a while.

Finally, I want to thank my girlfriend Natalia and my family for all the support they have given me all these years.

Chapter 1 - Introduction and aims of the work

1.1 Introduction

The research question which forms the basis of this MPhil is as follows: is it possible to enhance the sensor performance by combining the resistance and the light emission response, recorded simultaneously, from the same sensor, i.e. multi-modal sensing? There is a demand for practical, inexpensive, portable and user-friendly detection systems to detect volatile organic compounds (VOCs), and this research aims to fulfil that need. The detection of VOCs is important in areas such as environmental monitoring [1,2], medical diagnosis [3–5] and safety applications [6,7]. Therefore, several different analytical techniques and sensors found application in the detection of VOCs. In particular, sensor systems based on metal oxides have found a number of applications in the detection of VOCs [8–13] since they were first employed in the 1960s. Metal oxide sensor technology has made great advances since its inception, and recently this has involved the incorporation of nanomaterials to increase sensitivity and reduce the temperature of operation [14–16]. However, their fulfilment in real-life applications still presents a number of drawbacks, including a lack of selectivity and environmental sensitivity to changes in temperature and humidity [17,18].

This thesis looks to address this issue by increasing the sensitivity and the selectivity of metal oxide sensors by recording more than one physical quantity from the same device: i.e. the electrical resistance and the light emission (cataluminescence). A fundamental part of this thesis work was consequently the synthesis of several metal oxides and their characterisation. In particular, the focus was on doping with rare earth metals to increase the light emission response of these materials. Therefore, the metal oxide produced and tested during this project were $\text{ZrO}_2:\text{Eu}^{3+}$, and these were compared to undoped ZrO_2 and the conventional metal oxide-based materials WO_3 and ZnO .

In the case of the zinc oxide sensor, the UV-light activation at room temperature was explored instead of heating to elevated temperatures. Previous work had shown that this type of sensor as well as operating at room temperature, exhibited a higher selectivity to certain VOCs [19].

The resistance and the light emission response was measured following the interaction with different volatiles for all the sensor materials under test. The signals were recorded simultaneously and combined to obtain the dual-modality response of each sensor. The experiments were repeated at different sensor operating temperatures (150-400°C) and at a range of target compound concentrations. By analysing this large data set, the following questions were addressed. Firstly, which temperature was optimal for each sensor in terms of sensitivity and selectivity. Secondly, which sensor gave a better cataluminescence response to assess if doping with rare earth metals has a significant effect on the metal oxides light emission response. Finally, we assessed combining these responses to increase sensor sensitivity and selectivity under optimal operating conditions. The details of the dual-modality response are reported in section 1.6 of this thesis.

1.2 Volatile organic compounds (VOCs): definition and importance

Volatile organic compounds (VOCs) are a class of carbon-based chemical compounds that possess high volatility: the tendency of a solid to sublime or of a liquid to evaporate. This characteristic is typical of compounds with high vapour pressure so that those chemicals that tend to evaporate in certain conditions of temperature and pressure. A standard definition of VOC is as follows: a compound that at 293.15 K (20°C) presents a vapour pressure of 0.01 kPa. Also, they present a Reid vapour pressure of over 10.3 Pa again at 293.15 K of temperature and 101.325 kPa [20].

Volatile Organic Compounds, are an inseparable part of human life: anthropogenic and natural sources emit a large number of volatiles into the atmosphere and it is challenging to find a single

human activity that does not lead to a volatile emission: just to mention a few, driving a car, making a fire, painting a house, cutting the grass, building materials, using pesticides and even exhaling [21]. VOCs and their detection have a crucial role in different areas, such as environmental and air quality monitoring, medical diagnosis and safety applications [2]. These different fields of application are a matter of discussion in this section.

1.2.1 Importance of VOCs in environmental monitoring

Regarding the first aspect, environmental monitoring, we mainly refer to controlling the level of air pollution. A general definition of pollution is the one given in the Tenth Report of the Royal Commission on Environmental Pollution[22]:

"The introduction by man into the environment of substances or energy liable to cause a hazard to human health, harm to a living system, damage to structure or amenity or interference with legitimate use of the environment".

Nowadays, air pollution is inevitably a pillar of the environmental issue, and, as reported by Colls [23], each year, half a million people prematurely die because of exposure to air pollution (including volatile compounds). 30'000 in 2019 just referring to the United Kingdom, as estimated by the World Health Organization (WHO). In this context, VOCs play an important role, particularly the ones generated by anthropogenic sources, such as industries and refineries (bulk and fine chemicals), agriculture, vehicle emissions etc. Some critical aspects regarding the role of volatiles in air pollution are:

- their contributions in the ozone layer depletion
- their role as greenhouse gases
- their role as harmful compounds for the environment and human health.

Derived from both outdoor and indoor sources, VOCs in the atmosphere have a specific impact on human health and air quality [24,25]. In particular, indoor VOCs are a growing concern for public health. Schlink *et al.* reported the presence of 30 different compounds belonging to the classes of alkanes, cycloalkanes, aromatics, volatile halogenated hydrocarbons, and terpenes [26]. The problematic aspect is that their indoor concentration may be up to ten times higher when compared to the outdoor levels. As a matter of example, Lemer *et al.* reported an average level of benzene indoor of $12.837 \mu\text{g m}^{-3}$, almost twice the outdoor benzene concentration [27]. Among the other categories of compounds, aldehydes represent a class of harmful VOCs that is at higher concentrations indoors compared to outdoors [28]. Venn *et al.* underlined the dependence between indoor formaldehyde exposure and worsening of asthmatic children's wheezing symptoms [29], while long-term exposure can cause a number of health conditions, including cancer [30]. Other examples of indoor air pollutants are alcohols such as ethanol, ketones such as acetone, methacrylates (methyl or ethyl) and ethyl acetate. Acetone, in particular, is present in large concentrations in the indoor environment, with levels reported to be around $43.8 \mu\text{g m}^{-3}$ [31,32]. A study conducted in Mexico City reported that formaldehyde and acetone mean indoor air concentrations were the highest of the series of compounds analysed, reaching values of $97 \mu\text{g m}^{-3}$ and $89 \mu\text{g m}^{-3}$, respectively. These values are significantly higher if compared with the outdoor level, which ranges from 4 to $32 \mu\text{g m}^{-3}$ for formaldehyde and from 12 to $60 \mu\text{g m}^{-3}$ for acetone [33].

1.2.2 Importance of VOCs in medical diagnosis

Other than their importance in an environmental context, volatile organic compounds have a critical role as indicators of human health. More specifically, they have a potential role in the non-invasive early detection and diagnosis of several diseases. A vast number of biomarkers and metabolites are, in fact, volatile organic compounds. A review from de Lacy Costello *et al.* [34] of healthy human subjects and their associated VOCs showed that different VOC profiles were associated with different

bodily fluids. The combination of these profiles represents the current human volatilome. For example, in human breath, it was possible to identify 1488 different volatiles due to the body metabolic processes, and it is easy to imagine how the detection of these molecules is relevant for medical diagnosis [4].

Not least, altered acetone levels have a central role in diabetes-affected subjects, as do the other central ketone bodies acetoacetic acid and β -hydroxybutyric acid. These compounds presence derives from fatty acid utilisation (and then of ketone bodies as metabolites) instead of glucose as an energy source. Early-stage detection and monitoring can lower medical diagnostic costs and improve the quality of life of affected subjects [35]. Acetone detection in human breath, with a view to diabetes diagnosis and blood glucose monitoring, is a significant area of research [36–39]. Another strong correlation between volatiles and human health is diagnosing the second highest cause of death in men after heart disease, prostate cancer (PCa) [40]. The detection and analysis of volatiles to make an accurate diagnosis can help find an alternative to avoid the present biomarker test of prostate-specific antigen (PSA). The PSA test lacks accuracy, and this can lead to unnecessary prostate biopsies [41]. For example, the analysis of VOCs by a gas chromatography-mass spectrometry (GC-MS) system can represent a non-invasive, patient-friendly and more accurate option [42]. The detection of volatiles biomarkers collected from clinical samples represents a promising diagnostic tool. In fact, it is a non-invasive and, in most cases, inexpensive alternative in detecting altered metabolic conditions [43,44]. VOC detection has the potential to play a crucial role in diagnosing infectious diseases[45], metabolic disorders [46], poisoning[47], and other diseases, among which it is worth noting diabetes and diabetic ketoacidosis [48,49]and tumours, in particular lung [50–53] and colorectal cancer [54,55].

1.2.3 Importance of VOCs in safety applications: explosives detection

Many explosives are volatile or contain volatile marking agents or volatile by-products from their synthesis. Terrorism involving the use of explosives has increased due to the ease of manufacture of some improvised explosive devices, ease of deployment and the widespread damage and disruption caused by these explosive-based weapons [56]. Another concern is the location of landmines in current and former warzones [57]. Different analytical techniques can detect nitroaromatic compounds (NOCs), such as those using supramolecular ligands[58], micelles [59,60] and fluorescent conjugated polymers[61–63]. Nitroglycerine (NG), cyclotrimethylenetrinitramine (RDX), octahydro-1,3,5,7-tetranitro-1,3,5,7-tetrazocine (HMX), and 2,4,6-trinitrotoluene (TNT, one of the main components in landmines) are nitroaromatic compounds. 2,4-dinitrotoluene (DNT), an impurity present in TNT, has a headspace concentration of 148 parts-per-billion (ppb) compared to 6 ppb for TNT at room temperature, making 2,4-DNT a more realistic target for volatile detection methods [64].

Regarding plastic explosives, these commonly have a very low vapour pressure, but all commercially manufactured explosives have a more volatile taggant added to aid in detection via headspace sampling. One of these taggant compounds is 2,3-dimethyl-2,3-dinitrobutane (DMNB), which presents a vapour pressure of $2700 \mu\text{g m}^{-3}$ (2.7 ppm). This compound is a convenient compound since it allows the detection of the explosive to whom it is associated without affecting the shelf life and explosives stability [65].

Another challenge is the detection of explosives that do not contain nitro groups, most notably triacetone triperoxide (TATP). TATP and hexamethylene triperoxide diamine (HMTD) fall into the category of home-made improvised explosives (HMEs) and have considerable vapour pressure at room temperature and also contain volatile by-products such as acetone and hydrogen peroxide, which are constituents used in their synthesis.

1.3 Existing methods in VOCs detection

Against the background underlined in section 1.2, there is a high demand for effective methods to monitor VOCs for atmospheric environmental measurement and human diseases diagnosis and safety applications. Also, there is a current need to improve security screening methods for explosive detection.

Different techniques have been used for the accurate quantification of VOCs. One of these methods is spectrophotometry, definable as the quantitative measurement of a material's reflection or transmission properties as a wavelength function. Spectrophotometry can be utilised to detect VOCs, and an example is the one given by Khan *et al.*, which describes the detection of airborne toluene with good sensitivity by a deep-ultraviolet (UV) absorption spectrophotometer [66].

Gas Chromatography-Mass Spectrometry (GC-MS) is another vastly studied and well-established technique in detecting volatiles, especially in medical diagnosis, for example, in the case of Woollam *et al.*, which used a quadrupole time-of-flight (QTOF) gas spectrometer to study compounds related to breast cancer [67].

Ratiu *et al.* employed an aspiration-type ion mobility spectrometer (a-IMS) to analyse volatiles from microorganism strains. They could detect compounds such as the marker ortho-nitrophenol (ONP) produced by an enzyme-substrate reaction [68]. Gas chromatography-ion mobility spectroscopy has also been shown to be promising in VOCs detection for routine diagnosis applications [69].

Selected-ion flow tube mass spectrometry (SIFT-MS) was used to measure BTEX compounds (benzene, toluene, ethylbenzene, and the xylenes) in soil, water and air. One of the advantages of SIFT-MS is the faster analysis time when compared with the classical GC-MS systems [70].

Proton-transfer-reaction mass spectrometry (PTR-MS) has been used in VOC detection, especially in applications that require trace level detection in complex gaseous matrices [71].

All these analytical techniques present high precision and accuracy, but at the same time, are characterised by high power demand, most are not portable and are expensive. As a consequence of these factors, they are usually not suitable for field detection. Hence, over the last decades, sensor systems have been a possible answer to the considerable and unfulfilled need for compact, inexpensive and portable devices for infield use that enables quick detection of volatile organic compounds. Consequently, a wide variety of VOCs sensor systems have been developed, and among those, the ones based on metal oxide semiconductor materials are one of the most promising. They combine good sensitivity, a rapid response time [72] and a detection limit at ppb level [73], with small dimensions, compact size, and ease of use [74].

1.4 Metal Oxide Semiconductors (MOS) Gas Sensors

This section introduces the metal oxide semiconductors (MOS) materials studied during this research project concerning their feature as sensing substrates: ZrO_2 , $\text{ZrO}_2:\text{Eu}^{3+}$, WO_3 , and ZnO .

The theoretical aspects behind the MOS sensing mechanism and a possible explanation of the phenomena occurring on their surface following the interaction with a given volatile are presented. Following this, the two different conductivity types (n-type and p-type) are described, and a possible sensing mechanism is proposed for the two cases. Finally, this section presents how an n-type and a p-type MOS respond to oxidising and reducing volatile compounds.

1.4.1 Gas sensors: definition and classification

As seen in Section 1.3, sensors systems represent a promising area of interest in VOCs detection. On a general note, it is possible to define a sensor as a device that converts a physical or chemical phenomenon into an electrical signal [75]. Different categories of sensors exist: acoustic, biological, chemical, electrochemical, magnetic, mechanical, optical, radiation (particle), and thermal [76].

Herein we focus on chemical sensors, which can be defined as devices that transform chemical information into an analytically valuable signal [77]. In other words, chemical sensors present a material (i.e. metal oxides) as a receptor, which is a material that can change its chemical-physical properties following the interaction with a volatile. A possible classification of chemical sensors is the one reported in Fig.1 proposed by Wang [78]. We focused on gas sensors and, in particular, the one based on metal oxide semiconductors (MOS). The materials herein presented are zirconium oxide (ZrO_2), Europium-doped zirconium oxide ($ZrO_2:Eu^{3+}$), tungsten oxide (WO_3) and zinc oxide (ZnO).

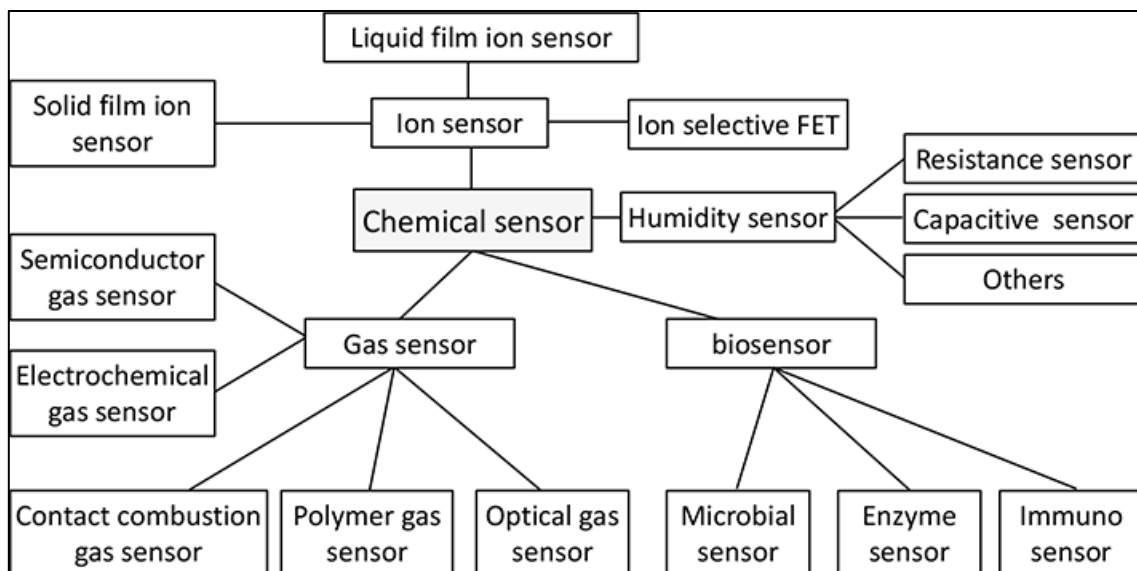


Fig. 1 Possible classification of chemical sensors. The materials herein presented are semiconductor gas sensors

1.4.2 Zirconium Oxide (ZrO₂)

The decision to study zirconium oxide as sensing support lies in the fact that it is a convenient candidate to be employed in multi-modal applications. In fact, it is widely used in sensing applications both as resistance and light emission sensors. A recurring theme in the various studies on pure ZrO₂ as a sensor is the notable increase in performance when employed as a nanomaterial [79–81]. Whereas bulk ZrO₂ used as a thick film has shown to be less sensitive to different gases [82–84]. Lobo *et al.* successfully used ZrO₂ nanotubes to detect a series of greenhouse gases (CFCl₃, CO₂ and CH₄) [85]. Husain *et al.* recently reported the possibility to employ zirconium oxide nanocomposites for the selective detection of ethane [80], while Zhou *et al.* incorporated ZrO₂ in a graphene-like nanofiber for sensing applications [86]. In general, applying zirconium oxide as a thin film in sensing devices is of pivotal importance [86–88].

Zirconium oxide is a white crystalline oxide, also known as zirconia. The pure material, at room temperature, presents a monoclinic crystalline phase, which has a transition to a tetragonal and cubic phase at higher temperatures [82,89–91]. In particular, the tetragonal phase is stable for temperatures in the range 1170-2370°C, while the cubic for temperatures above 2370°C [92]. Since the first studies on solid electrolytes based on stabilised zirconia by Nernst at the end of the XIX century [93] and the first applications of zirconium oxide as a gas sensor in the 1980s [94], this material has attracted interest due to its features: hardness, refractive index, optical transparency, chemical stability, high coefficient of thermal expansion, and high resistance to corrosion [95–97]. Thus, it finds application in different fields such as fuel cell membranes [98], catalyst support [99] and, over the last thirty years, as a sensing substrate.

1.4.3 Europium-doped Zirconium Oxide (ZrO₂:Eu³⁺)

Pure zirconium oxide thin films produce luminescence [100–102] and also cataluminescence (CTL) [103,104]. However, it is possible to enhance the light emission of ZrO₂ by including in its structure rare earth metal ions such as Y³⁺ [84], Er³⁺ [105], and Sm³⁺ [106]. The Europium-doping is also of great interest since Eu³⁺ complexes are characterised by narrow light emission bands and long lifetimes [95]. These aspects are possible thanks to the introduction of f-electrons in a zirconia-based material [107]. In addition, these light emission characteristics make ZrO₂:Eu³⁺ a likely candidate as a highly sensitive gas sensor. Rosa *et al.* showed the potential of this material in oxygen detection [95]. Zhang *et al.* underlined the promising characteristic of the europium-doped zirconia sensor, particularly as regards CTL: high selectivity, high stability and simplicity of apparatus [108]. In addition to sensing applications, the europium-doped zirconium oxide is currently employed in optical thermometers [109], and photonic applications such as optical communication [110,111]

1.4.4 Tungsten Oxide (WO₃)

Tungsten oxide is a widely studied n-type MOS, largely employed as a resistance-based sensor. In addition, it is a heavily used commercial sensing material. Consequently, it was included in this research work as reference material for the resistance measurement.

Tungsten oxide is a yellow/bronze-like powder whose crystals can be found primarily in the monoclinic crystalline phase (stable in the temperature range 17-330°C) and triclinic, orthorhombic, tetragonal, and cubic phases [112]. Among the different possible applications, WO₃ has been profoundly studied as a resistive gas sensor substrate. In recent years, Yu *et al.* reported a highly sensitive and selective WO₃ sensor for H₂S in the temperature range 20-160°C [113]. Lei *et al.* also

reported the possibility of detecting NO₂, H₂ and NH alongside hydrogen sulphide. Currently, WO₃ is a heavily used commercial sensing material.

As regards VOCs, an ultra-high selective tungsten oxide-based sensor for the detection of acetone was recently presented by Zhang *et al.* [114]. At the same time, Ramanavičius *et al.* underlined the possibility to detect a series of alcohol-based VOCs (methanol, ethanol, isopropanol) by a WO₃/WO_{3-x}-based sensing surface [115]. Tungsten oxide sensors have been reported to have performance improvement when constructed from nanomaterials. [103,104]. Consequently, different WO₃ nanostructures are used in sensing applications: a WO₃ hollow-sphere gas sensor was fabricated by Li *et al.* to detect with good sensitivity alcohol, acetone, CS₂, and other organic gases [116]. A p-type sub-tungsten-oxide based urchin-like nanostructure was presented by Yao *et al.* for the detection of ethanol [117,118].

1.4.5 Zinc Oxide (ZnO)

Zinc oxide nanostructures (nanowires, nanoparticles, nanorods, thin films, etc.) have been widely studied. They find applications in different areas such as optoelectronics, sensors, transducers and biomedical sciences such as microbiology, toxicology and virology [119–122]. This material, commonly found as a white powder, usually presents tetrahedral coordination almost exclusively in the wurtzite type structure [123]. ZnO is also characterised by a wide bandgap (3.37 eV), large exciton binding energy (60 meV), and excellent thermal and chemical stability [124]. ZnO is also a widely established gas sensing material [125–127]. Devices based on ZnO nanostructures play an essential role due to their simplicity of the detection method [128], energy-saving, accessible auxiliary materials and unsophisticated equipment [129].

1.4.6 MOS nanoparticles gas sensors: working principles

MOS can be employed in sensing applications as nanoparticles since the nanoscale presents a series of advantages: high stability, easy surface functionalization and potentially low operating temperature [130]. In addition, nanoparticles exhibit excellent optical and electrical properties due to electron and phonon confinement, high surface-to-volume ratios, modified surface work function, high surface reaction activity, high catalytic efficiency and strong adsorption ability [131].

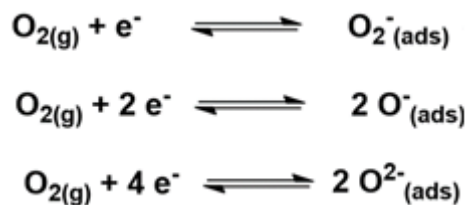
A key parameter in sensing applications is sensitivity. It is well known that if the particle size is comparable to double the thickness of the space charge layer, the sensitivity will be considerably enhanced [132]. In addition, the sensor sensitivity is directly proportional to the sensor surface area exposed since a higher surface area can enable more contact with analytes [133]. Thus, nanomaterials are often considered the best solution for gas sensor applications compared to bulk materials since the specific surface area increases with decreasing particle size. As an example, a commercial-grade zinc oxide shows surface areas between 2.5 and 12 m²/g, while ZnO nanoparticles can show surface areas of 54 m²/g [134]

In the same way as the Silicon based semiconductors, it is possible to identify both MOS nanoparticles in which the majority charge carriers are electrons (n-type) or holes (p-type). The origin of the two different types of conductivities can be traced back either to doping aliovalent cations or oxygen non-stoichiometry. An example of an n-type material is ZrO₂. The n-type conductivity corresponds to a surplus of electrons representing the majority charge carriers. According to Batzil *et al.*, this type of material present an excess of electrons due to the generation of electrons following the formation of oxygen vacancies [135].

On the other hand, an example of p-type material is NiO, whose conductivity can be explained due to the introduction of Ni²⁺ vacancies occurring in conditions of oxygen excess [136]. Both p-type and n-type metal oxides present different sensing mechanisms. Analogously, they give a different and diametrically opposite sensing response in the presence of reducing and oxidising gases. Devices

based on n-type MOS present are the most used in sensing applications, due to their relatively high sensitivity, even though they present environmental sensitivity to changes in temperature and humidity[136]. Regarding p-type materials, the main advantageous aspect underlined in the literature is the possibility to reduce the dependence of the gas-sensing characteristics on humidity [136–138]. Nevertheless, p-type sensors showed an overall lower response when compared to n-type. Hübner *et al.* suggested that when the morphological configurations of both sensor materials were identical, the p-type showed a response equal to the square root of the n-type[139].

The adsorption and desorption of gases on a semiconductor materials' surface, causing a change in the conductivity, has been well known for sixty years [140]. In clean air conditions, at a temperature $150^{\circ}\text{C} < T < 450^{\circ}\text{C}$, molecular oxygen adsorbs on the metal oxide surface as negatively charged ions: O^{2-} , O^{-} , O_2^{-} , since it traps electrons from the metal oxide bulk at the surface layer. A description of the phenomena occurring on the material surface is presented in *Equation 1*.



Equation 1

At the typical sensor operating temperatures above 150°C , O^{-} is the prevalent species. This phenomenon occurs for both n-type and p-type metal oxides, resulting in an increase in the sensor resistance (n-type) or a decrease (p-type). The sensor signal corresponds to a change in the electrical resistance results from the interaction between these oxygen ions and an incident gas [74].

With reference to MOS nanoparticles, the core-shell model is a satisfactory way to describe the response of a MOS nanoparticle when exposed to a compound in the gaseous state [136]. Thus, for

both n-type and p-type materials, the ionosorption of oxygen forms a core-shell configuration in the MOS nanoparticles. In particular, for n-type materials, the formation of an *electron depletion layer (EDL)* occurs, representing the nanoparticle shell. This EDL is characterised by high electrical resistance since the oxygen ions have captured the electrons. In contrast, the core of the nanoparticle is characterised by a comparatively low electrical resistance, as shown in Fig. 2(a). On the other hand, in p-type materials, we see the depletion of electrons by oxygen ions results in a *hole accumulation layer (HAL)*. In this case, the nanoparticles' shell is characterised by a comparatively low electrical resistance. Whereas the core presents a high electrical resistance: the holes have moved to the shell, shown in Fig. 2(b).

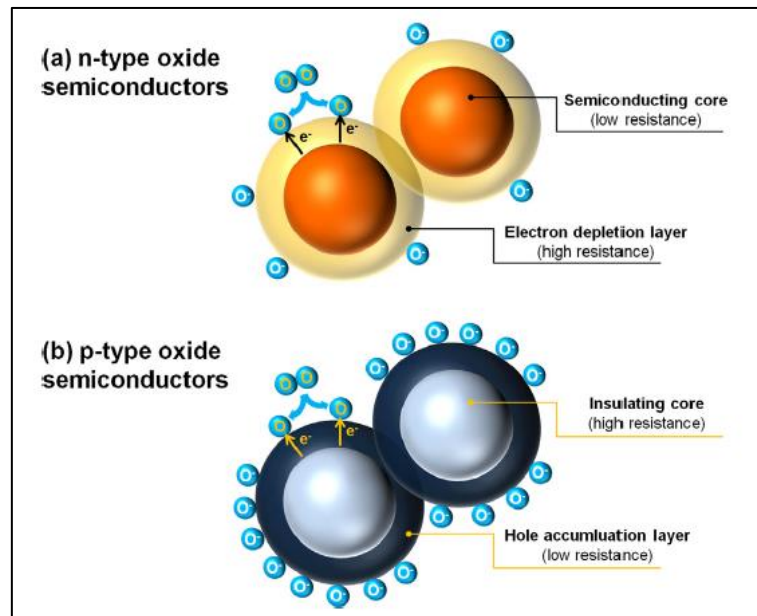


Fig. 2 Both in n-type (a) and p-type (b) semiconductors nanoparticles, the interaction with oxygen brings to a core-shell configuration

In quantistic terms, O⁻ adsorption on the metal oxide surface brings about the formation of a space charge region, to which is associated a surface band bending qV_s , described in *Equation 2*.

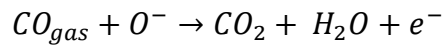
$$qV_s = \frac{q^2 N_O^2}{2\epsilon\epsilon_0 n_D}$$

Equation 2

In the above equation, N_O is the surface density of oxygen ions, n_D is the donor density, q is the elementary charge, ϵ and ϵ_0 represent the absolute and the relative value of the dielectric constant. In general terms, surface band bending magnitude under gas exposure is a measure of surface reactivity. Changes of qV_s can be measured by the Kelvin probe method.

1.4.7 Sensing mechanism for the n-type materials

From what has been said so far, it must be understood that n-type and p-type materials give diametrically opposed responses to oxidising and reducing gases. Let us start with the case of an n-type material, such as the well-studied SnO_2 or the materials analysed in this work, such as ZnO and WO_3 . When a reducing gas like CO approaches the surface of the MOS, it reacts with the ionosorbed oxygen (*Equation 3*).

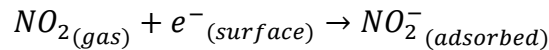


Equation 3

A combustion reaction occurs involving the reducing gas and the oxygen and producing H_2O and CO_2 , which are desorbed to the gas phase. Consequently, the electron formally trapped by the surface oxygen ions is now released back to the bulk. In quantistic terms, this process causes the space charge layer to shrink.

The macroscopic consequence is a decrease in the sensor's electrical resistance. The change in resistance (the sensor's response) indicated the presence of a reducing gas on its surface, in this case, CO. On the other hand, this aspect can represent a drawback in terms of selectivity since most reducing gases react on the sensor surface, giving approximatively the same effect. This phenomenon is even more relevant when the gases reacting on the surface have different concentrations[17].

On the other hand, an oxidising gas (NO₂) can also be defined as an acceptor since it subtracts further electrons from the MOS surface. This results in an increase in sensor resistance (fewer electrons are available for the conduction). As an example, *Equation 4* describes the electrons transfers occurring when NO₂ reacts with the metal oxide.



Equation 4

1.4.8 Sensing mechanism for the p-type materials

In p-type materials, as discussed above, the conduction is via holes, positively charged pseudo-particles representing the vacancy of an electron. Consequently, the interactions with oxidising and reducing gases bring opposite results if compared with those of n-type materials. As we have seen, a reducing gas (such as H₂) has the apparent ability to inject an electron into the hole accumulation layer (HAL), causing an increase in sensor resistance. In contrast, an oxidising gas that is able to subtract further electrons from the HAL corresponding to the formation of new holes and to a reduction in resistance. The behaviours described in this section can be summarised in *Table 1*.

Table 1 Overview of the sensing behaviour (in terms of electrical conductivity) of n-type and p-type semiconductors when exposed to oxidising and reducing gases

Sensing material	Interaction with:	
	Oxidising Gases (NO ₂ , ozone, N ₂ O)	Reducing Gases (H ₂ , CO, H ₂ S, NO, CH ₄)
n-type (SnO ₂ , In ₂ O ₃ , WO ₃ , ZnO, ZrO ₂)	Resistance INCREASE	Resistance DECREASE
p-type (CuO, Co ₃ O ₄)	Resistance DECREASE	Resistance INCREASE

1.5 Cataluminescence (CTL)

1.5.1 CTL: definition and overview

The cataluminescence (CTL) is a specific type of luminescence produced when a molecule is oxidised through a catalytic process [141]. The term cataluminescence was first presented by Breysse, which observed that the catalytic oxidation of carbon dioxide (CO₂) on a thoria (ThO₂) surface could produce light emission [142]. It is possible to treat the light emission production process as an adsorption-reaction-desorption process, as shown in Fig. 3 [143]. In more detail, the oxygen (O₂) and a reactant (R) diffuse from the gaseous phase to the surface of the catalyst resulting in the production of chemisorbed reactant (R_{ad}) and chemisorbed oxygen (O_{2ad}). Following the catalytic reaction, the desorbing process generates the chemisorbed product RO_{ad}, which desorbs into the gaseous phase.

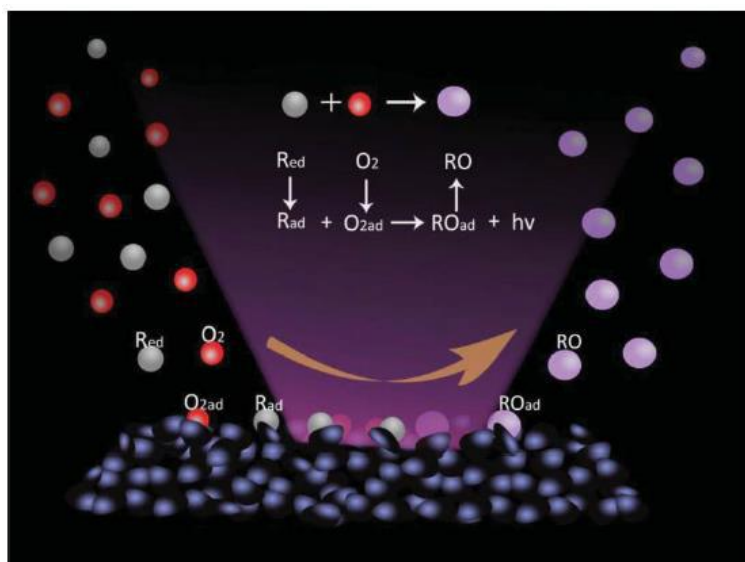
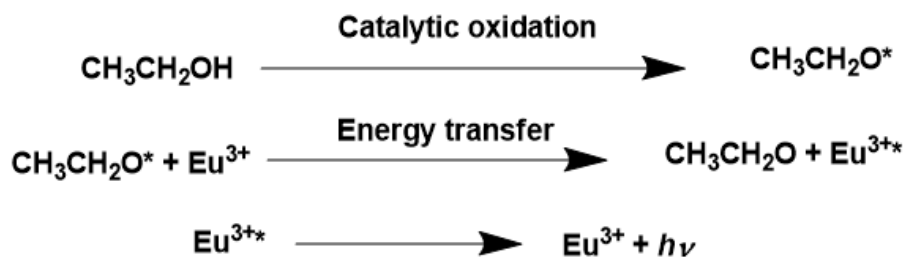


Fig. 3 Schematic diagram of the basic principle of CTL as modelled by Hu et al., 2019 [143]

The exact mechanism is still under investigation, but up to this point, three different pathways have been identified to explain how the generation of CTL occurs [144], including recombination radiation, radiation from the excited species [145], and energy transfer emission[108]. In particular, for the rare-earth ion-doped MOS, the energy transfer occurs between the excited intermediates and these doped rare-earth ions, such as Eu^{3+} or Tb^{3+} leading to excitation of the rare-earth ions and release of luminescence.

It is possible to explain the last case by studying the emission spectrum of acetaldehyde: indicating an energy transfer process due to the overlap of the CTL emission spectrum of CH_3CHO^* and the absorption spectrum of the rare-earth ions. A schematic description of the process is as follows:

- (1) $\text{CH}_3\text{CH}_2\text{OH}$ catalytically oxidises into CH_3CHO^* on the surface of the catalyst;
- (2) the energy transfer process between CH_3CHO^* and Eu^{3+} takes place to form CH_3CHO , and Eu^{3+*}
- (3) Eu^{3+*} returns to the ground state (Eu^{3+}) accompanied by the emission of light, as shown in Equation 5. Thus, the rare-earth ion presence leads to higher light emission.



Equation 5

1.5.2 CTL-based gas sensors: an overview

The light emission produced in the catalytic process described above can be employed for high sensitivity gas sensor systems. Even though the electrical-based gas sensors (i.e. conductometric) are the most studied worldwide, sensing devices based on cataluminescence can present different advantages such as tolerance from electronic noise and independence from the electrical properties of the material [146]. In addition, CTL-based sensors are characterised by rapid response [147], high portability [148], and low detection limit and the instrument employed are usually user-friendly [149]. Nevertheless, cataluminescence sensors present several limitations. In the first place the lack of selectivity when exposed to complex mixture of volatiles. At present, different CTL-based MOX sensors have been developed for the detection of VOCs such as formaldehyde [150,151]. Hu *et al.* reported a ratiometric CTL sensor for the detection of different volatiles [152], while Li *et al.* reported the successful detection of carbon monoxide through an energy-transfer CTL process [153] Another interesting outlook is the use of metal-organic framework (as highly effective adsorbents in the gas capture and preconcentration) in combination with a sensing substrate able to produce CTL to achieve

a high sensitivity response [149,154]. It is possible to obtain the CTL sensing also from metal-free material, such as the porous boron nitride (p-BN) presented by Bian *et al.* [155].

1.6. Multimodal sensing

In the sensor technology, when two (or more) responses from a single sensor are combined to improve the performance, we are talking about *multimodal sensing*. The critical advantage of multimodal sensing is the possibility of achieving the needed selectivity through a single sensor device. This option is consequently a portable, user-friendly, relatively low cost, and energy-saving solution.

Over the last few years, different multimodal sensing techniques have been developed to enhance selectivity in detecting volatiles from a single sensor substrate. Wong *et al.* employed a nanocomposite fiber within a quartz tuning fork, obtaining a sensor capable of detecting H₂ selectively, combining chemo-mechanical sensing for sensitivity and electrochemical sensing for selectivity. [156]. Another possibility is the one introduced by Bouvet *et al.*, which included the combination of conductivity and the reflected microwave measurement [157].

The combination of the resistance and the cataluminescence signal from a single sensor substrate, which is the main object of this thesis work, represents another suitable possibility to obtain highly sensitive and selective multimodal detection of volatiles. Even though sensors based on the resistance and on the cataluminescence singularly have been widely studied (as underlined in the sections above, their combination is a novel approach, firstly published as a patent by de Lacy Costello (P123791GB) [158]. The work presented in the patent has been successively implemented and published [159].

1.7 . Aims of the work

The need for highly responsive devices arises because sensors are not always capable of guaranteeing a high degree of efficiency in real-life applications (i.e. mixed gas environment) [160]. Several methods exist in the MOS gas sensors field to detect a specific target compound within a homogenous mixture of volatiles. In the first place, the introduction in the MOS structure of metal particles may increase the selectivity to a target gas. As an example, Gong *et al.* reported that the Cu doping of ZnO nanoparticles enhanced the selectivity to CO [161]. However, this type of doping has been found to guarantee only in part an enhancement in selectivity [132]. Selective gas detection can also be achieved by the gas mixture pretreatment, i.e. using catalytic filters to remove interferants from the mixture of gas containing the target compound before reaching the sensor device [162,163]. In addition, another common possibility is to combine a series of different sensors (different materials) in an array [164–166]. As outlined in Chapter 6, multimodal sensing presents several advantages.

This research project mainly intends to look into the possibility of combining the electrical resistance and the cataluminescence responses from a single sensor to achieve better performance (i.e. selectivity and sensitivity). To achieve this outcome, the following steps will be taken: Synthesis and characterisation of a series of metal oxide semiconductors.

- Test of the synthesised material recording simultaneously the resistance and the light emission with different volatiles. The experiments are repeated at different concentrations of the tested compounds and in a range of operating temperatures, to identify the best operating conditions for each of the materials under investigation.
- Combination of the resistance and the light emission response to achieve the multimodal sensing and evaluate the possible advantages in terms of sensor performance (particularly sensitivity and selectivity).

Chapter 2 - Materials and Methods

2.1. Synthesis of zirconium oxide-based nanoparticles

The route followed for the synthesis of the metal oxides was a wet chemical method analogous to the one reported by Zhang *et al.* [108]. The materials synthesised for use in the fabrication of the sensing devices were as follows: $\text{ZrO}_2\text{:Eu}^{3+}$, $\text{ZrO}_2\text{:Y}^{3+}$, $\text{ZrO}_2\text{:Tb}^{3+}$ and $\text{ZrO}_2\text{:Er}^{3+}$. Fig. 4 shows the nanopowders obtained.



Fig. 4 The metal oxide nanopowder synthesised: from left to right $\text{ZrO}_2\text{:Eu}^{3+}$, $\text{ZrO}_2\text{:Y}^{3+}$, $\text{ZrO}_2\text{:Tb}^{3+}$ and $\text{ZrO}_2\text{:Er}^{3+}$

2.1.1 Synthesis of $\text{ZrO}_2\text{:Eu}^{3+}$ (5%)

The chemicals utilised in the synthesis of the mixed metal-oxide $\text{ZrO}_2\text{:Eu}^{3+}$, (Europium five atomic per cent of molar fraction in respect to Zirconium) were of analytical grade and used as received from the suppliers: $\text{ZrO}(\text{NO}_3)_2$ (Aldrich); $\text{Eu}(\text{NO}_3)_3(\text{aq})$; $\text{NH}_4\text{OH}(\text{aq})$ (5M) (Fluka).

The preparation method involved the addition of 2.5 mL of a 0.02M $\text{Eu}(\text{NO}_3)_3(\text{aq})$ solution to 10 mL of a 0.1 M $\text{ZrO}(\text{NO}_3)_2(\text{aq})$ solution with rapid stirring. Different concentrations of the $\text{Eu}(\text{NO}_3)_3(\text{aq})$ solution led to different atomic percentages of Europium in the final material. Analogously, using

different rare earth precursor solutions, the other doped materials were obtained. Subsequently, a 0.1M NH₄OH (aq) solution was added dropwise until the reaction mixture reached pH 8. The pH was constantly monitored through a pH meter. The precipitate formed was filtered and washed three times with deionised water. The precipitate was first dried in an oven at 60°C for 1 hour, and finally calcined in a muffle furnace for 3 hours at 600°C.

2.2. Volatile organic compounds (VOCs) and interferants

All the chemicals utilised for the preparation of the VOC sensor testing standards were of analytical grade and used as received from the suppliers; NG and EGDN were supplied by the MOD as 10% by weight immobilised and phlegmatized on Kieselguhr (diatomaceous earth). The concentration range utilised for acetone ranged between tens of ppb (29.6) up to approximately three hundred ppm.

Table 2 Volatile organic compounds (VOCs) tested and relative sample vapour concentration (ppm)

Sample	Concentrations (ppm)
Acetone	0.0296 – 296
Ethanol	0.05871 – 58.71
Water	312
Hydrogen Peroxide	1.92
Ethylene Glycol Dinitrate (EGDN) 75°C	0.63
Nitroglycerine (NG) 75°C	0.64
2,4-Dinitrotoluene (DNT) 75°C	0.50
2,3-Dimethyl-2,3-Dinitrobutane (DMNB) 75°C	2.76
Triacetone Triperoxide (TATP)	0.55-55

2.3. Volatiles concentration validation using Selected-ion mass spectroscopy (SIFT-MS)

In the sensing experiments, different volatile concentrations were obtained using a 10 mL gas-tight syringe and undertaking serial dilutions of the test VOC headspace within the syringe. The concentrations reported were validated by selected ion flow tube (SIFT) mass spectrometry to check the method's accuracy.

The SIFT-MS used for all the experiments is a Voice 200 (Syft technologies, New Zealand). The sample inlet was set to the default flow rate of 30 mL/min, with the inlet capillary and operating at 120°C. The dwell time for each mass was set to 1000ms or 100,000 counts depending on which was achieved first. The selected compound for this method was acetone. The detection limit was of 50 pptv and the accuracy +/- 10% in ppbv range.

Serial dilutions were carried out using a 10 mL gas-tight glass syringe. For example, 1 mL of acetone headspace was taken from the vial and to obtain a dilution of 1/10, this 1 mL headspace sample was diluted with lab air to 10 mL in the syringe and returned to 1 mL. By repeating this operation, a second time this allowed a concentration of 1/100 of the headspace concentration of acetone, repeating three times gave a concentration 1/1000 of the headspace concentration of acetone and so on. The 1 mL sample was then interfaced with the SIFT-MS sampling head and analysed to obtain the concentration in ppm.

2.4 Nanoparticle characterisation

2.4.1 Microscopy Techniques

Transmission electron microscope (TEM) images were captured using a Philips CM10 TEM, 100kV, with a Gatan Orius SC100 (model 832) digital camera.

The metal-oxide nanoparticles were also characterised using a scanning electron microscope (SEM), operating at 30kV, combined with EDX using a FEI. Quanta 650 field emission SEM Three different detectors were used: Large Field Detector (LFD), Gaseous Secondary Electron Detector (GSED) and Gaseous Back Scattered Electron Detector (GBSD).

The nanoparticle materials' composition was determined using Energy Dispersive X-Ray Microanalysis (EDX), using an Oxford Instruments AZtec Energy EDX system. The voltage used was between 7.5-20 kV.

2.4.2 X-Ray Diffraction

X-Ray Powder Diffraction (XRD) patterns were recorded on a Bruker D2 Phaser in theta-theta geometry using Cu ($K\alpha_1/K\alpha_2 \lambda = 0.15418$ nm) radiation and a Ni $K\beta$ filter (detector side). Additional beam optics and settings: primary and secondary axial Soller slits (2.5°), fixed 0.6 mm divergence slit, 1mm anti-scatter-screen, Detector: 1D LYNXEYE with a 5° window, Generator: 30kV, 10mA. The software used for data analysis was DIFFRAC.SUITE COMMANDER, Bruker A.X.S. DIFFRAC.EVA 2.1, Bruker AXS (2010-2012).

2.4.3 Spectroscopical techniques

Vibrational Raman spectra and photoluminescence spectra of sensor surfaces were recorded using a Horiba LabRAM HR Evolution Raman Microscope using an Olympus M Plan x5, NA 0.15 objective lens. For Raman scattering measurements, a 785nm laser, ~30mW, was used. For the photoluminescence spectra, excitation was with a 532nm laser, ~0.3mW.

For Cataluminescence and Photoluminescence measurements, the sensor was packaged in a dye cast box with an optical window; vapour samples were input to the sensor chamber to obtain cataluminescence spectra.

Cataluminescence spectra were recorded using an EG&G 1460 OMA system including a 0.25m Jarrell Ash 82-497 polychromator, 300 lines/mm grating, and 1254 intensified silicon detector cooled to -20°C and an accumulation time of 20 seconds. The sensor was placed immediately in front of the polychromator entrance slit. The experimentally determined black body radiation (BBR) from the heated sensor was subtracted from the total emission spectrum to yield the cataluminescence spectrum.

2.5 Sensor Preparation

The sensor substrate was a 3 mm x 3mm square alumina tile. On the front face of the sensor, two gold interdigitated electrodes (four pairs of interpenetrating bars, electrode gap 100 µm) were screen printed. Screen printing was undertaken at ESL Europe (8 Commercial Road, Reading, Berkshire, RG2 0QZ), with John Whitmarsh and Karen Jones Williams. A Dec 1202 screen printing machine was used for all screen-printing work. On the reverse face, a platinum heater track was screen printed which also served as a temperature sensor. The sensor/heater assembly was wire bonded to a TO39 transistor can. The platinum heater's resistance at different temperatures (150-400°C) was determined by placing the sensor in an oven whose temperature could be varied. The temperature was calculated from the temperature coefficient of resistance (TCR) and the R_0 value. In operation, a feedback control loop was used to maintain the sensor at the required preset temperature.

All the sensors were fabricated using a drop-coating method to apply the sensor material to the interdigitated electrodes: a small amount (0.2g) of the metal oxide was placed in a glass vial, and sufficient water (0.4 g) was added to produce a thick slurry by stirring. The sensor was prepared by

drop coating the oxide paste onto the sensor substrate's top surface (3 x 3 mm alumina tile) to completely cover the interdigitated gold electrodes. The sensor was then allowed to dry at room temperature for 12 hours before use. Fig. 5(a) shows the sensor uncoated, while Fig. 5(b) the sensor coated with ZrO₂ and ready to be employed in the sensor system.

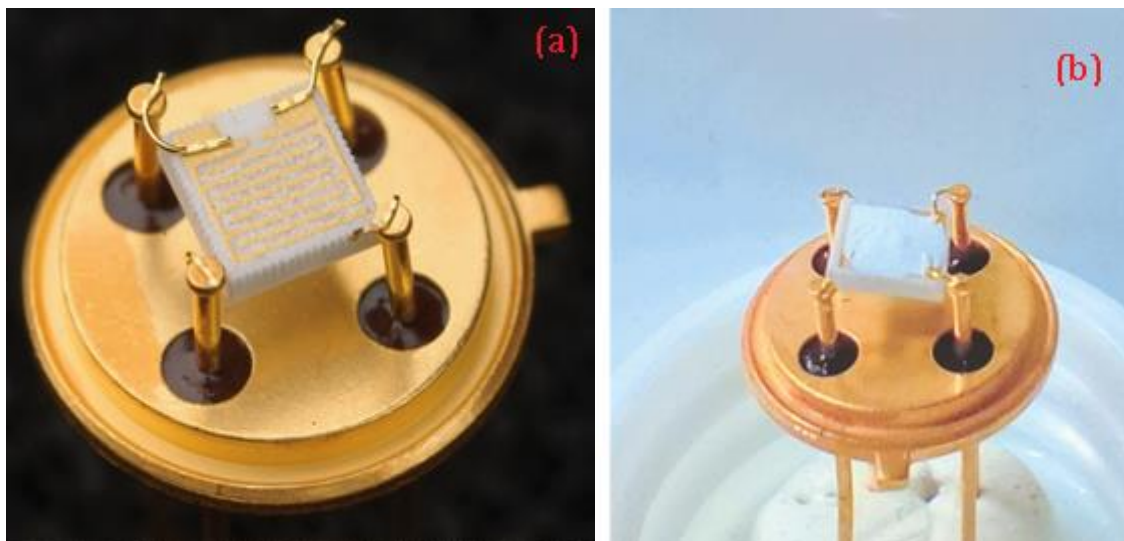


Fig. 5 Sensor uncoated: it is possible to observe the gold wires and the interdigitated electrodes (a). The sensor used during the experiments; it was drop-coated with ZrO₂ nanopowder (b).

2.6 Experimental

Two different sensor system embodiments were used during the project: the heated sensor and the UV-activated sensor. Regarding the first type, the critical aspect was testing three different semiconductor metal oxides: ZrO₂, ZrO₂:Eu³⁺ and WO₃. Each of these sensors was tested for the target compounds at an increasing concentration to explore which compounds a given sensor has the best sensitivity and selectivity. Each experiment consists of the simultaneous recording of both the resistance and the light emission sensor response following the interaction with a particular target VOC. In this way, it is possible to have a complete screening in terms of resistance and cataluminescence response and study these materials in dual-modality. The sensor substrate is

temperature-activated. Consequently, all the experiments were repeated at different temperatures, in the range 180-400°C.

Regarding the UV-activated sensor, the material studied was ZnO. In this case, the changes in resistance following the interaction with a volatile was registered. The sensor was activated using a UV-LED, and the incident light intensity was varied by adjusting the voltage supplied to the LED. This enabled the selectivity of the sensor to be tuned compared to operating at maximum UV intensity.

2.6.1 Heated metal oxide sensors

The sensor substrate is an alumina tile 3mmx3mm, which has interdigitated gold electrodes on the obverse side, as in Fig. 6(a), and a platinum resistance heater on the reverse reported in Fig 6(b). There are gold wires bonded to the electrodes and heater pads, and the whole structure is mounted onto a transistor can to produce a stable sensor substrate. The sensor comprises a thick film paste of the metal oxide, which is coated onto sensor substrates, Fig. 6(c)

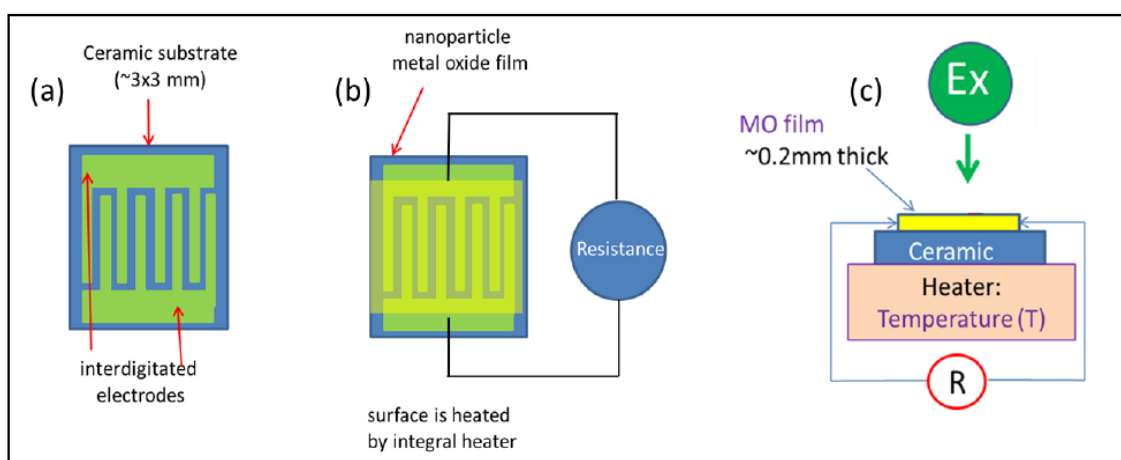


Fig. 6 Schematic representation of the sensors substrate: details of the ceramic substrate and the interdigitated gold electrodes(a), the platinum resistance heater(b), the sensor system (c)

The sensor is generally heated in the range of 180-400°C using a platinum resistance heater on the sensor substrate's reverse. A schematic representation of the sensor system is reported in Fig. 7.

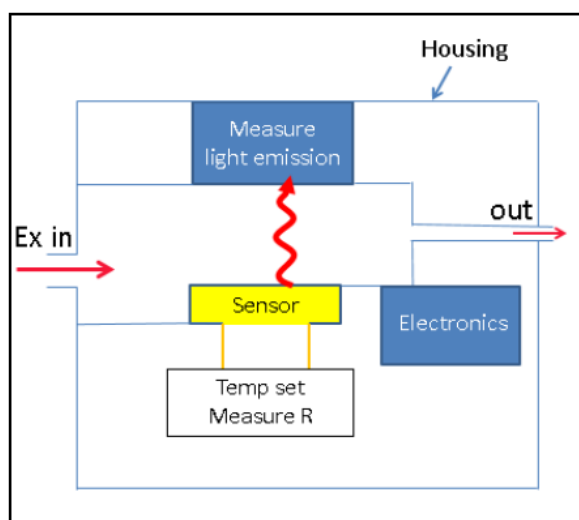


Fig. 7 Schematic representation of the temperature-activated sensor system

The sensor is located inside a chamber, 100 mL volume approximately, and inside a light-tight box that eliminates background light which would interfere with the measurement of cataluminescence. Air is drawn consistently through the chamber and across the sensor at a rate of 100 mL/min using a micro diaphragm pump (K.N.F. Neuberger). The volatile compounds of interest are diluted from headspace concentrations and injected using a 10mL gas-tight syringe via a silicone rubber septum attached to the sensor chamber's inlet tubing. The constant flow rate mixes and transports the volatiles to the sensor chamber within a few seconds. The final concentration in the chamber is calculated, and the dual-modality response is measured. Several controls are run, such as injecting air or water headspace to ensure that the response is due to the target and not just due to humidity, background volatiles, syringe contamination or oxygen partial pressure, *et cetera*.

As previously mentioned, the tests on a given sensor are conducted at different temperatures (180°C to 450°C, for example) and different concentrations of the target volatile compound (low ppb to high ppm).

2.6.2 CTL measurements

The light (cataluminescence) produced following the reaction occurring on the sensor's surface is detected by a Hamamatsu photomultiplier with a photon-counting mode. The photomultiplier gives a signal related to the number of photons emitted by the sensor, and it is detected by an ASCEL Electronic AE20401 5.8 GHz Frequency Counter. Then, the light emission, expressed in photons per second, was plotted against time to obtain a cataluminescent response profile. Regarding the resistance, the sensor is linked to a voltage source (1V applied), and the change in current in response to the presence of a volatile compound is monitored via a Keithley Electrometer model 617 and connected through a suitable PicoLog analogue to digital converter interface to a computer.

2.6.3 UV-activated sensor

An alternative approach developed at UWE and more widely in the literature [19] is replacing the substrate's heating with UV illumination, which photoexcites the oxide material, having a similar effect and giving sensitivity at room temperature. A diagram of this embodiment is shown in Fig. 8.

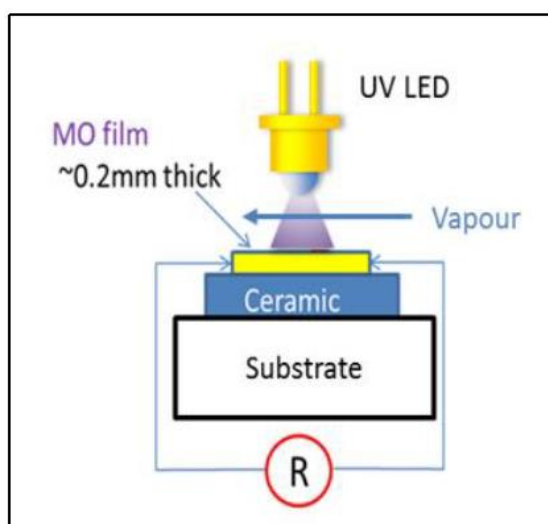


Fig. 8 Diagram of the UV-activated resistance sensor

The sensor system was analogous to the one described above for the temperature-activated sensor, but in this case, external heating was not required. Since, in this case, the cataluminescence produced by the sensor was not registered, this embodiment did not include a photomultiplier. At the same time, UV-light emitting diodes (LEDs, RS Components, Corby, Northants, NN17 9RS) were utilised as the UV source in all the experiments. They had a quoted peak wavelength of 400 nm and a measured maximum intensity of 30 mW/cm². This value was selected based on the material properties. In fact, this value was selected based on the material properties. In fact, zinc oxide shows a band gap of 3.44 eV. The wavelength of 400 nm as the UV absorption maximum is close to this band gap value. The LED incorporated a lens to give a focussed source of light. These were incorporated into the rig so that they were 1mm above the sensor surface, and the UV light was focused directly onto the oxide surface. The UV level was adjusted and not operated at peak intensity.

Chapter 3 - Results

3.1. Material Characterisation

3.1.1 X-Ray diffraction (XRD)

The powder X-Ray Diffraction experiments were performed on the ZrO_2 and $\text{ZrO}_2:\text{Eu}^{3+}(5\%)$ nanoparticles (NPS). Fig. 9 shows the diffraction pattern for the undoped zirconium oxide.

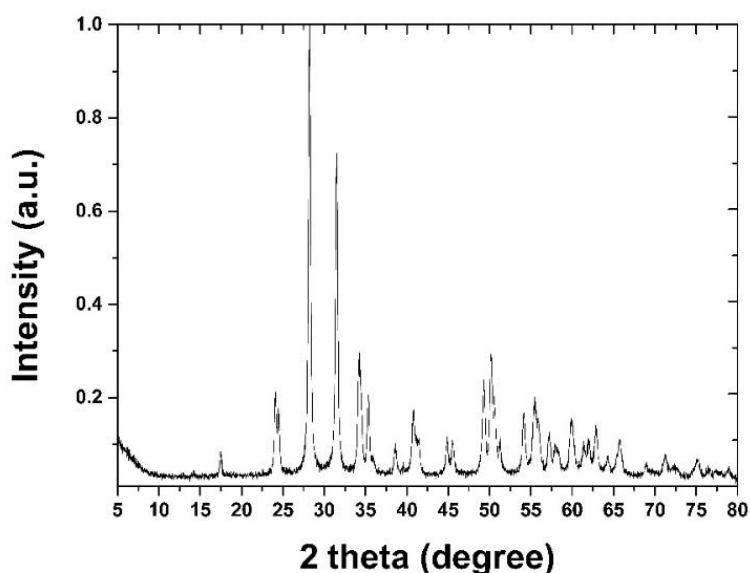


Fig. 9 X-Ray Diffraction (XRD) pattern of the undoped zirconium oxide

The data are reported as 2 theta (two times the incidence angle) value vs the signal intensity, registered as an absolute value by reference with the most intense peak. The software *Match3!* was used to fit the experimental data to a library diffraction pattern and to attribute the crystalline phase. The same pattern with the corresponding fit is shown in Fig. 10.

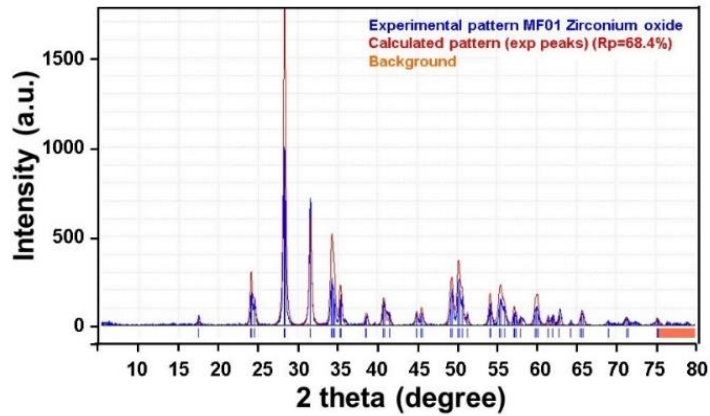


Fig. 10 XRD pattern of the undoped zirconium oxide and relative phase attribution fitting. The blue trace refers to the experimental data, while the red trace corresponds with the library diffraction pattern.

The XRD pattern is well fitted, and a monoclinic phase was attributed to the ZrO_2 . Analogously, in Fig. 11, the $\text{ZrO}_2:\text{Eu}^{3+}(5\%)$ diffraction pattern is shown, while Fig. 12 presents the fit-pattern that allowed the crystalline phase attribution.

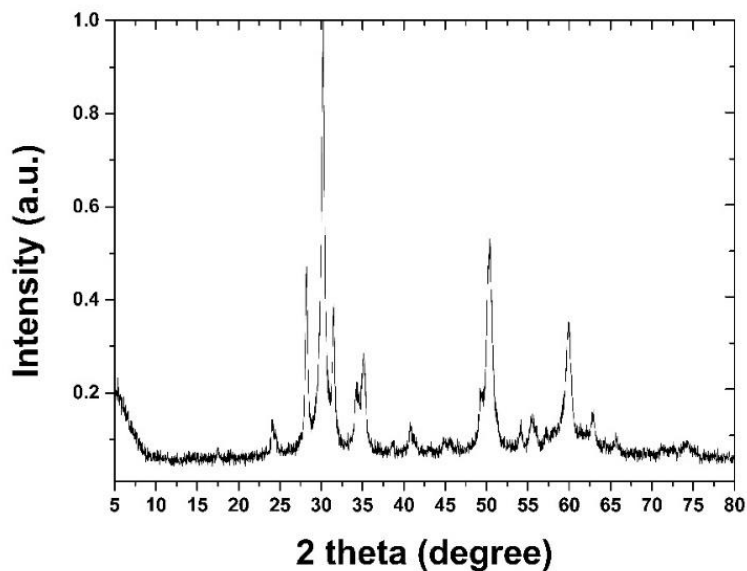


Fig. 11 X-Ray Diffraction (XRD) pattern of the $\text{ZrO}_2:\text{Eu}^{3+}(5\%)$

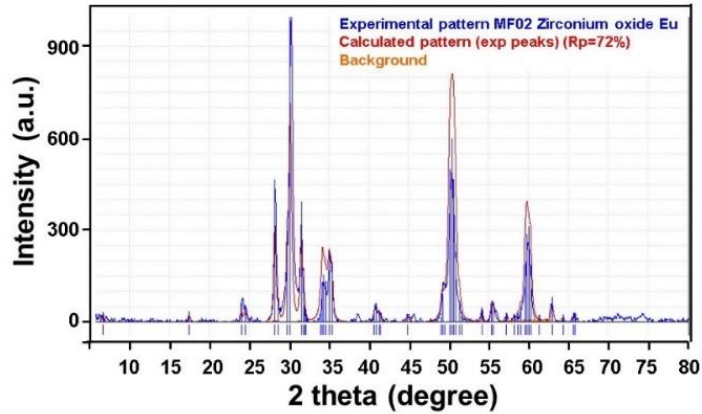


Fig. 12 XRD pattern of the $ZrO_2:Eu^{3+}$ (5%) and relative tetragonal phase attribution. The blue trace refers to the experimental data, while the red trace corresponds with the library pattern

It was also possible to calculate the average particle size through the Debye-Scherrer formula (Equation 6):

$$D_c = \frac{K\lambda}{\beta \cos\theta}$$

Equation 6

Where D_c is the average particle size, K is the Scherrer constant taken to be equal to 0.94; the X-Ray source wavelength is 0.15418 nm, and β is the full-width half-maximum of the peak at a diffraction angle of θ . The average particle size calculated for the undoped oxide was 17 nm, and that for the Europium-doped was 21 nm.

3.1.2 Transmission Electron Microscopy (TEM) and Scanning Electron Microscopy (SEM)

The transmission electron microscopy experiments were performed on ZrO_2 and the $ZrO_2:Eu^{3+}$ (5%) nanoparticles. The ZrO_2 nanoparticles image is reported in Fig. 13, where it is possible to observe a uniform distribution in terms of particle size, that the nanoparticles are monodispersed and have a spherical shape. The particle size distribution calculated by the software *ImageJ* was 22 nm which

agrees well with the theoretical calculation based on the Debye-Scherrer equation. Fig. 14 refers to the $\text{ZrO}_2:\text{Eu}^{3+}$ synthesised in the laboratory.

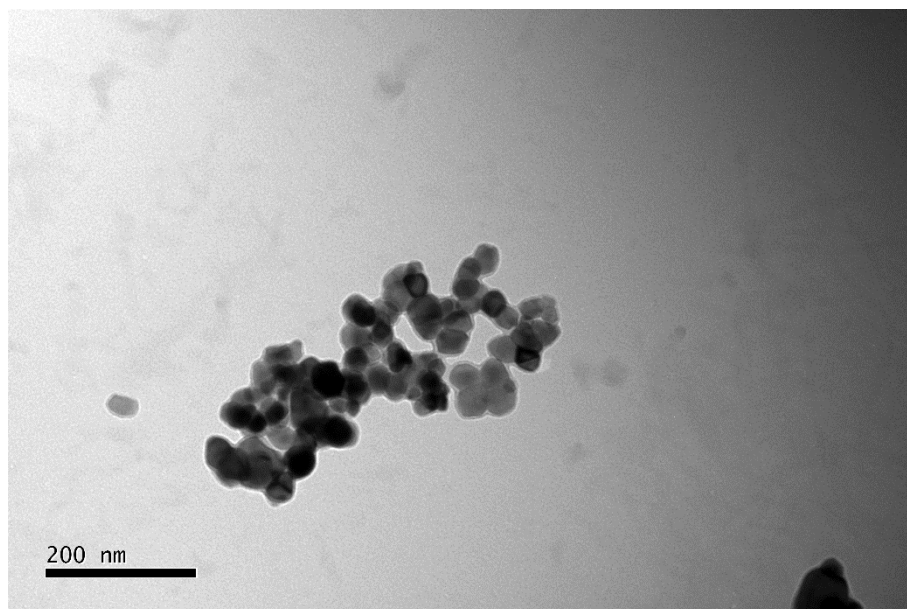


Fig. 13 Transmission Electron Microscopy (TEM) image for ZrO_2

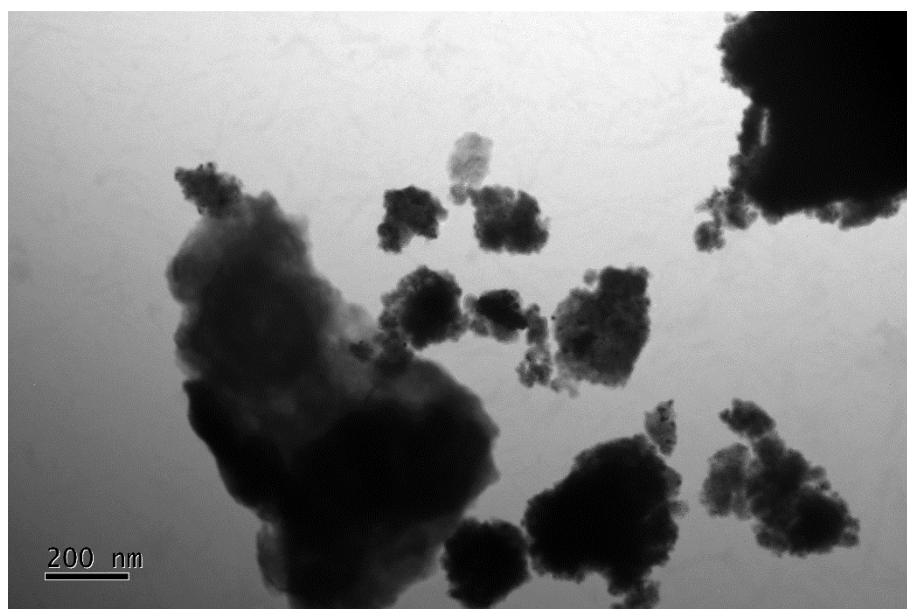


Fig. 14 Transmission Electron Microscopy (TEM) images for $\text{ZrO}_2:\text{Eu}^{3+}$ (5%)

In this case, the first aspect that it is possible to underline is the formation of different clusters. The particles seem to have maintained the spherical shape, even if the size reduced considerably. This aspect is also confirmed by the average particle size of 15 nm, also calculated with *ImageJ*. Again, this is in good agreement with the theoretical calculations based on the Debye-Scherrer equation.

The same nanoparticles were also investigated with scanning electron microscopy (SEM). This technique has previously been employed for the characterisation of zirconium oxide nanoparticles [167–169]. In our case, it was possible to make an imaging study both for the undoped and for the Europium-doped zirconium oxide. Fig. 15 shows the ZrO_2 , while Fig. 16 refers to $ZrO_2:Eu^{3+}(5\%)$.

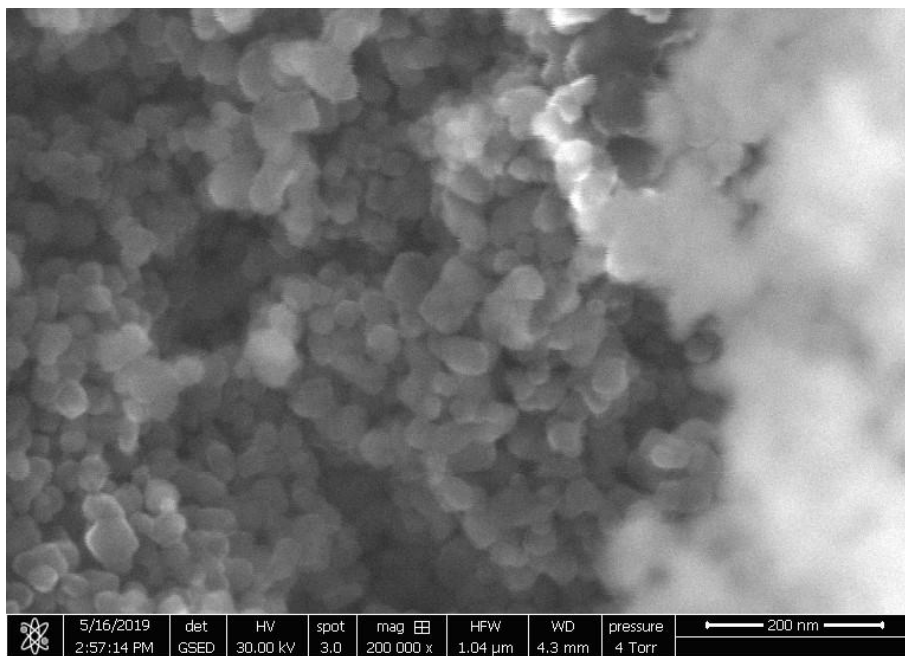


Fig. 15 Scanning Electron Microscopy (SEM) images for the ZrO_2 nanoparticles

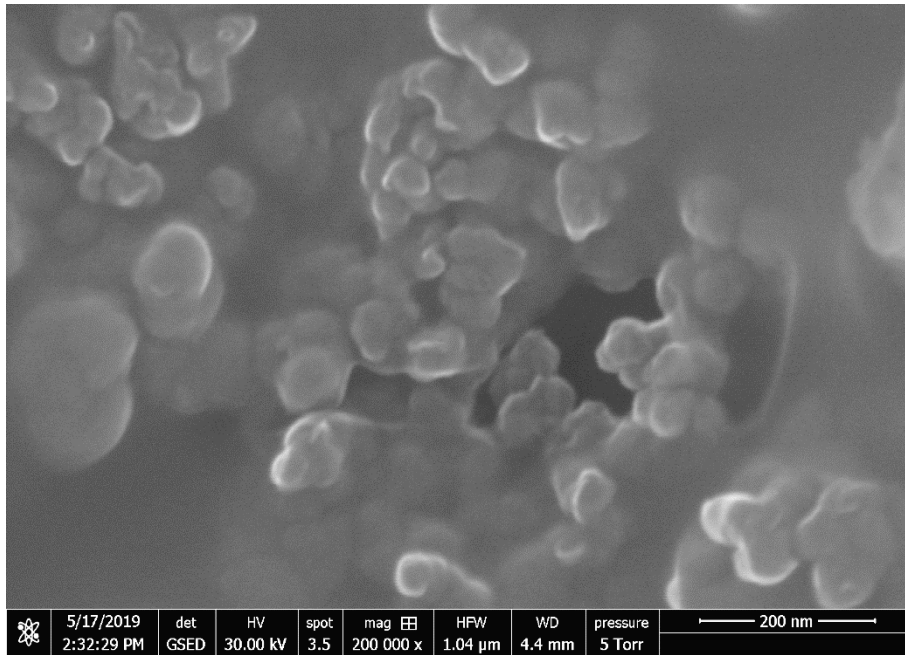


Fig. 16 Scanning Electron Microscopy (SEM) images for $ZrO_2:Eu^{3+}(5\%)$ nanoparticles

3.1.3 Energy Dispersive X-ray Analysis (EDX.)

The elemental composition of ZrO_2 and the $ZrO_2:Eu^{3+}(5\%)$ was studied and confirmed by energy dispersive X-ray analysis, and the spectra are reported in Fig. 17 and Fig. 18, respectively. In particular, Fig. 18 shows three prominent peaks attributable to the presence of europium in the material. The experiment utilised a beam acceleration voltage of 20 kV.

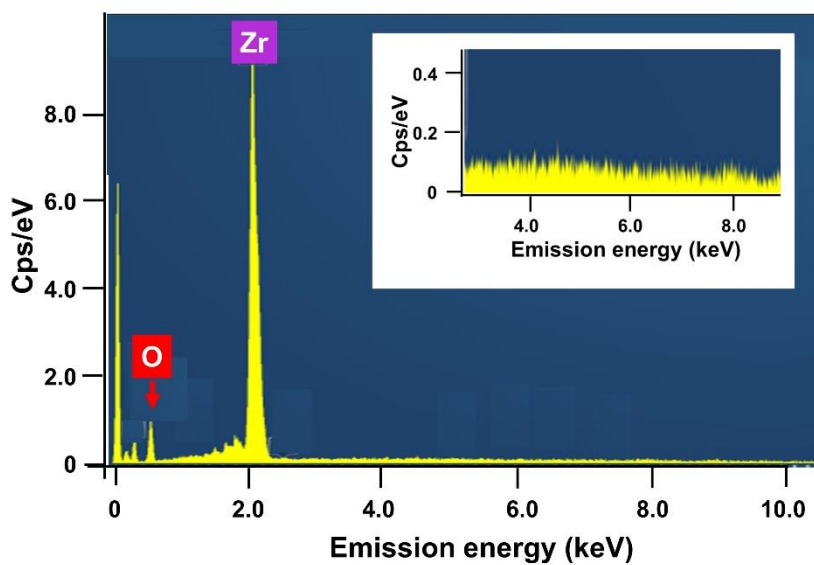


Fig. 17 EDX spectrum for undoped ZrO_2 material. The peak positions for zirconium and oxygen are marked.

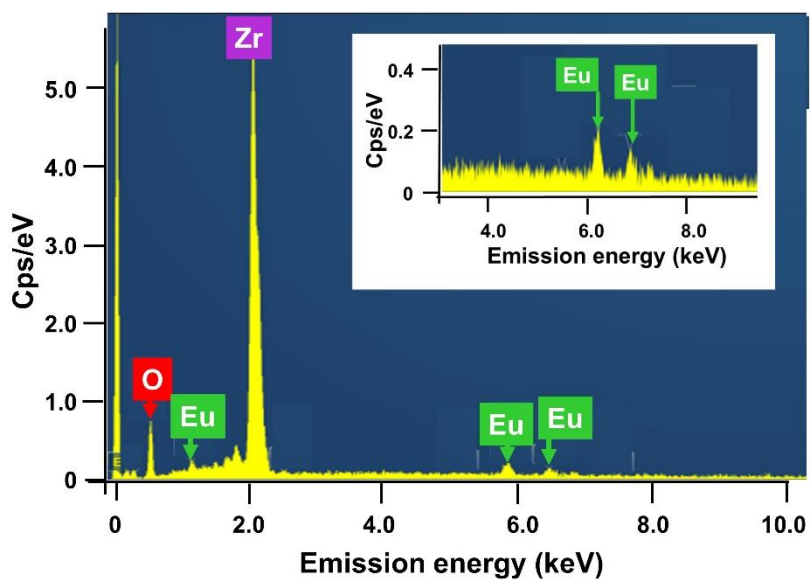


Fig. 18 EDX spectrum for $ZrO_2:Eu^{3+}$ (5%). The peak positions for zirconium, oxygen, and europium are marked.

3.1.4 Raman Spectroscopy, Photoluminescence and Cataluminescence

The Raman spectra are shown in Fig. 19 for the undoped ZrO_2 and the europium doped ZrO_2 materials for an excitation wavelength of 785 nm. The ZrO_2 (blue trace) was attributed to a monoclinic phase (m), while the $\text{ZrO}_2:\text{Eu}^{3+}$ (red trace), to a tetragonal phase (t). The peaks' positions are marked following Hui *et al.*[170]: monoclinic at 179 and 190 cm^{-1} and tetragonal at 147, 264, 319, 462 and 642 cm^{-1} .

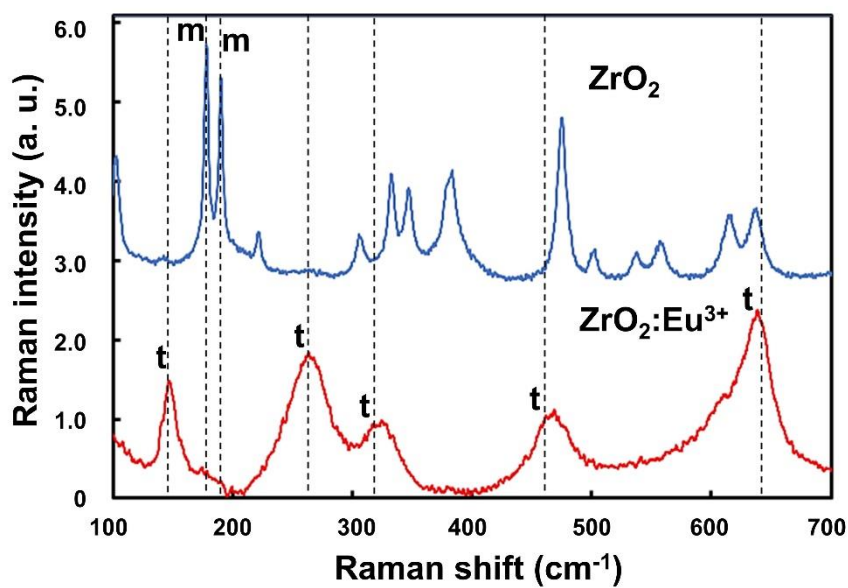


Fig. 19 Raman spectrum of the undoped ZrO_2 nanoparticles (upper trace) and $\text{ZrO}_2:\text{Eu}^{3+}$ nanoparticles (lower trace).

The photoluminescence (PL) spectrum for the $\text{ZrO}_2:\text{Eu}^{3+}$ material is shown in Fig. 20(c), recorded at a sensor temperature of 450°C. The two major PL peaks are at 592 and 607 nm. Hui *et al.* recorded PL spectra for ZrO_2 doped with Eu^{3+} with concentrations in the range of 0.5 to 5%. Reference to Fig. 19 of Hui *et al.*[170] shows that, for PL excitation at 254 nm, they observed principal PL peaks at similar positions, i.e. 593 and 608 nm. When their material was doped with at least 3% Eu^{3+} , their PL line shapes were similar to those we found for our europium doped zirconium dioxide.

Cataluminescence spectra shown in Fig. 20 regarding the interaction of acetone vapour (2 parts per thousand) with (a) undoped ZrO_2 and (b) $\text{ZrO}_2:\text{Eu}^{3+}$ also at a sensor temperature of 450°C . The cataluminescence spectrum from $\text{ZrO}_2:\text{Eu}^{3+}$ is similar to that of the corresponding photoluminescence spectrum recorded at the same temperature (Fig. 20(c)). The cataluminescence spectrum from the undoped ZrO_2 is a broad featureless response over the 400 – 700 nm region.

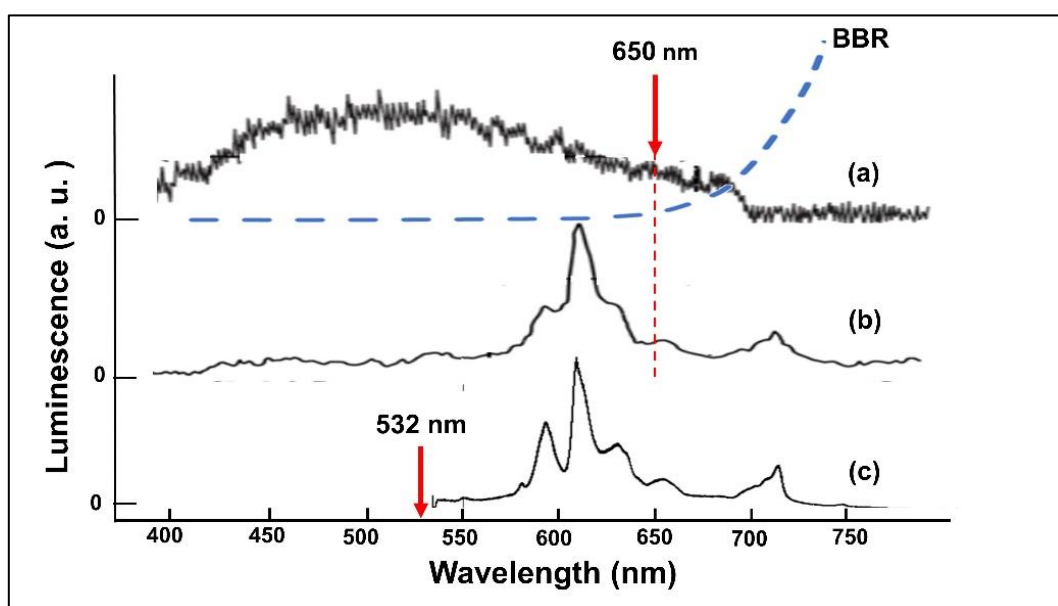


Fig. 20 Photoluminescence and cataluminescence spectra at 450°C : (a) cataluminescence from undoped ZrO_2 for acetone at 2 parts per thousand (ppth). The blue dotted line indicates the calculated form of black body radiation (BBR). (b) cataluminescence from $\text{ZrO}_2:\text{Eu}^{3+}$ for acetone at 2 ppth and (c) photoluminescence from $\text{ZrO}_2:\text{Eu}^{3+}$ with 532 nm excitation.

3.2 Concentration test: SIFT-MS

This section presents the Selected Ion Flow Tube - Mass Spectrometry performed to validate the syringe dilution method. Fig. 21 shows that diluting the acetone's headspace concentration by a factor of ten using the syringe corresponds to a drop-in concentration in the SIFT response and that this drop-in concentration corresponds to a *circa* 10-fold decrease in the measured concentration of acetone in ppm.

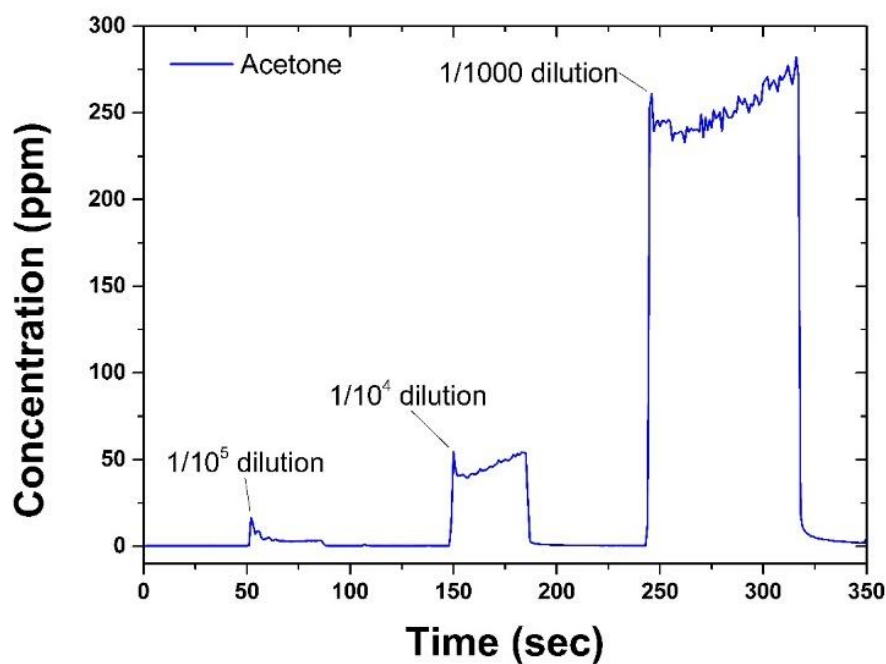


Fig. 21 Different dilution levels, starting from acetone's headspace concentration, were registered by selected ion flow tube (SIFT) mass spectrometry

It is also possible to compare the expected values of acetone concentration for a given dilution and the concentration effectively registered by the SIFT-MS. The slope obtained by linear regression of the SIFT-MS measured data vs the theoretical values of acetone concentration is reported in Fig. 22. Four dilutions have been considered. The data measured by the SIFT-MS gives a good correlation with the theoretical values calculated.

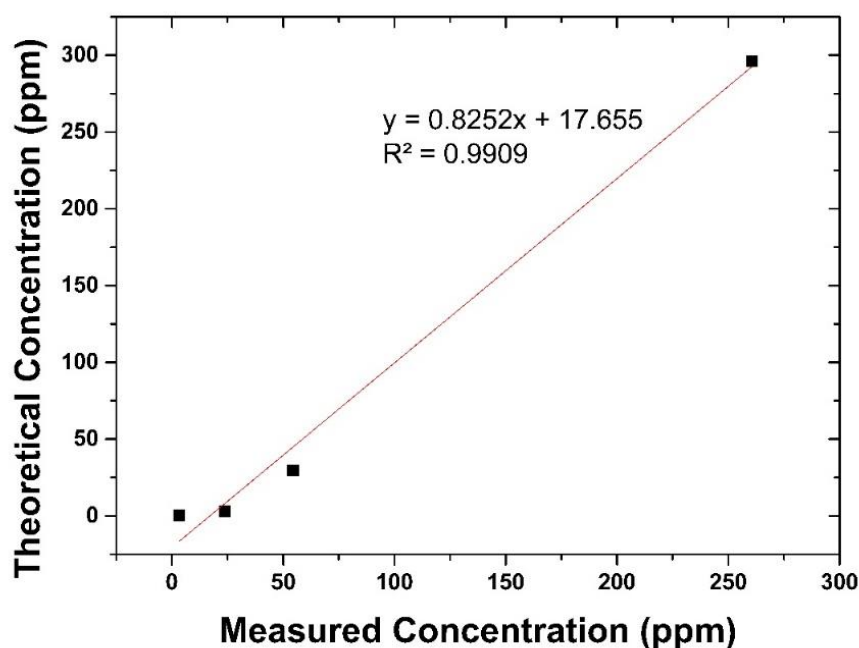


Fig. 22 Theoretical acetone concentration as a function of the concentration measured by SIFT-MS when using the glass syringe-dilution method.

3.3. Sensing experiment: an overview

The following sections (3.4-3.7) present the results in terms of electrical resistance and CTL for the four sensing materials included in this research project: ZrO_2 , $\text{ZrO}_2\text{:Eu}^{3+}(5\%)$, WO_3 and ZnO . Regarding the ZnO sensor, the cataluminescence experiments were not carried out, and these measurements will be the object of future studies. A series of volatile organic compounds (VOCs) and interferants were analysed with the sensing apparatus described in the *Materials and Methods* section: acetone, ethanol, water, hydrogen peroxide, ethylene glycol dinitrate (EGDN), nitroglycerine (NG), 2,4-dinitrotoluene (2,4-DNT) and 2,3-dimethyl-2,3-dinitrobutane (DMNB). All the experiments were conducted at room temperature and humidity conditions (RH = 40-60%). Each sensor was tested at the temperatures 150°C, 180°C, 200°C, 250°C, 275°C, 300°C, 350°C and 400°C.

Regarding the electrical resistance, the response was measured in Ohms as a function of the time (seconds). The sensor performances were characterised in terms of percentage response, as defined in *Equation 7*.

$$R\% = \frac{(R_{gas} - R_{air})}{R_{air}} \times 100$$

Equation 7

In *Equation 7*, R_{air} is the sensor resistance value in the presence of laboratory air, while R_{gas} refers to the sensor response when a target gas (for example, ethanol) is injected into the system. In particular, the R_{gas} value corresponds with the maximum of the response peak.

The light emission signal is expressed in photons per second as a function of time (second). The CTL response is determined by subtracting the baseline (black body radiation, BBR) from the peak value. In fact, the baseline is associated with the black body radiation, and consequently, it increases with temperature, as it is possible to see in Fig. 23. It is possible that the increase in the BBR with temperature masks the cataluminescence response, and additional filters could be used to reduce the BBR and observe the true CTL response at higher temperatures.

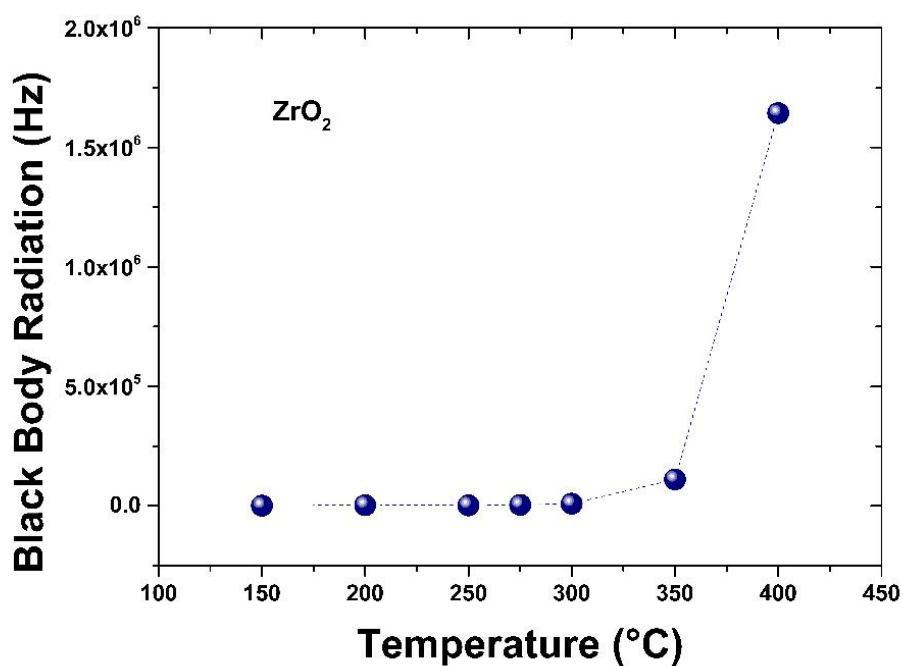


Fig. 23 Increase of the background (black body radiation) as a function of the temperature

To assess the multimodal sensing characteristics of the synthesised materials, the resistance and the cataluminescence were measured simultaneously. As an example, Fig. 24 shows the dual-modality profile of the europium-doped zirconium oxide at a sensor operating temperature of 300°C. The device was tested with three consecutive injections of acetone at a concentration of 296 ppm. The figure shows a peak in the light emission (cataluminescence) which corresponds with an increase in the electrical resistance of the sensor when exposed to acetone vapour.

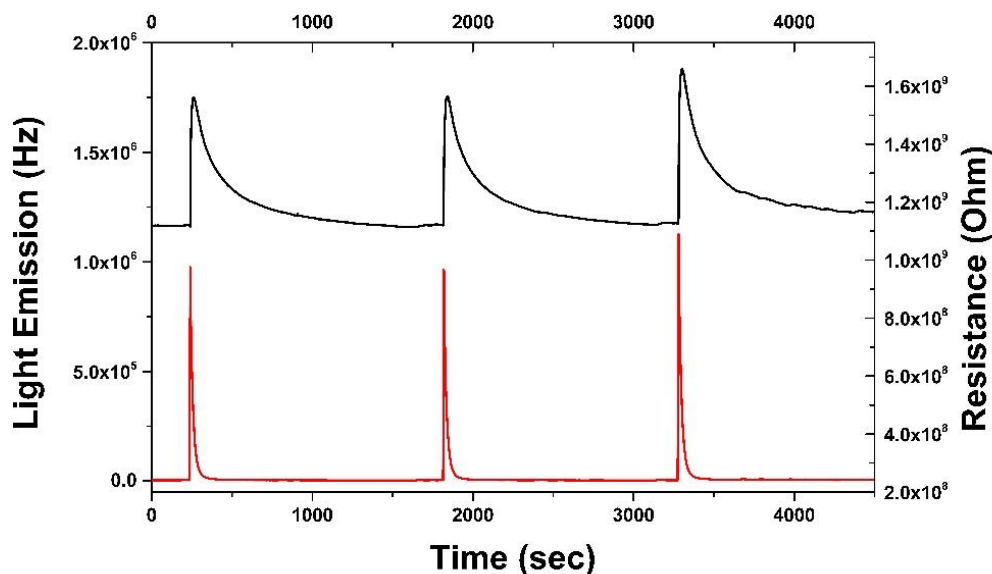


Fig. 24 Dual-modality profile for the $ZrO_2:Eu^{3+}(5\%)$ at the operating temperature of $300^\circ C$, following three subsequent injections of acetone (296 ppm), It is possible to notice the high repeatability of the resistance (black trace) and CTL (red trace) responses. Both responses occur simultaneously (multimodal response) but with different kinetics.

The above graph shows the raw data of the dual-modality experiments: the light emission (CTL) response expressed in Hertz (photons per second) and the resistance in Ohms versus the time displayed in seconds. The first aspect to point out is that the Europium-doped zirconium oxide gave a p-type response (the resistance increase following the interaction with acetone), while the undoped ZrO_2 showed an n-type behaviour in the experiments with acetone.

In addition, the graph allows us to underline several characteristics of the dual-modality experiment. First and foremost, the simultaneity of the resistance and the CTL response, without which it would be meaningless to talk of dual-modality. Secondly, the high reproducibility of the response signal for both the modalities ($\pm 5\%$). Thirdly the response time for the injected pulse is analogous for both the modalities ($\sim 10s$); on the other hand, the recovery time is significantly different: in the experiment reported in Fig. 23, the average recovery time for the resistance was ~ 1400 seconds (23 minutes) versus ~ 180 seconds (3 minutes) in the case of the cataluminescence response. The definition used

for the recovery time was the time required for the signal to recover fully to the pre-exposure background level.

The dual-modality response was expressed with a ratio between the light emission (cataluminescence) and the percentage resistance response (*Equation 8*).

$$\text{Dual – modality} = \frac{\text{Light Emission}}{\text{Resistance response (\%)}}$$

Equation 8

The error computation in the following sections was calculated as in *Equation 9*, so that as the ratio (e) between the standard deviation (σ) and the square root of the number of repeated measures (n).

$$e = \frac{\sigma}{\sqrt{n}}$$

Equation 9

3.4 Zirconium oxide sensor (ZrO₂)

3.4.1 ZrO₂ - Resistance experiments

The volatiles analysed during the research project were tested at a range of concentrations. In acetone's case, the range investigated was from 29.6 ppb up to 296 ppm Fig. 25 shows the sensor response following the interaction with three consecutive acetone injections at an operating temperature of 150°C. Even at this temperature, the lowest investigated, the sensor showed a significant response to acetone. The mean response to acetone was circa 75%. Also, Fig. 26 shows a concentration reduced by a factor of ten when compared with Fig.25, still at 150°C (resistance response of 30%).

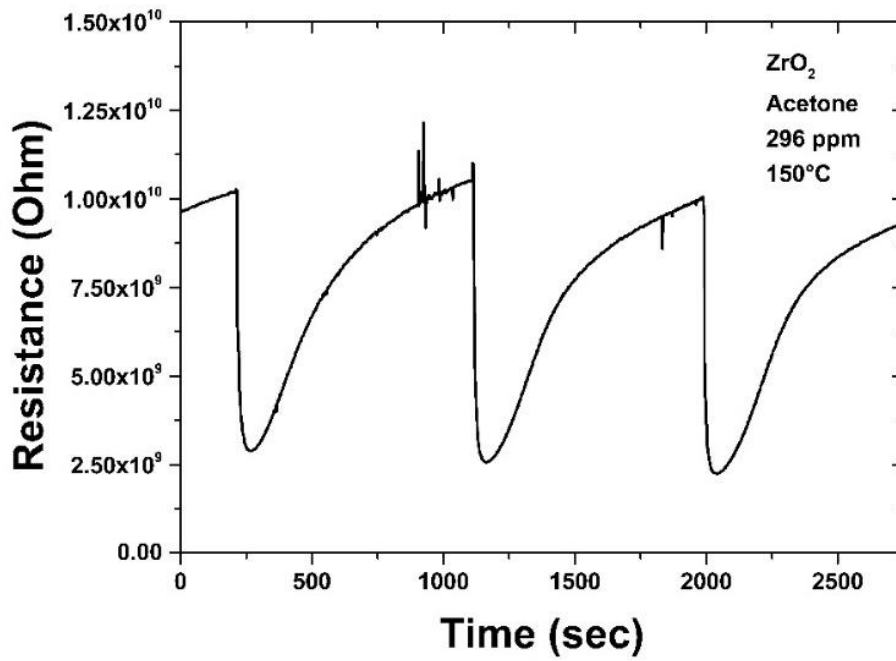


Fig. 25 Zirconium oxide resistance response to acetone (296 ppm). Temperature set to 150°C

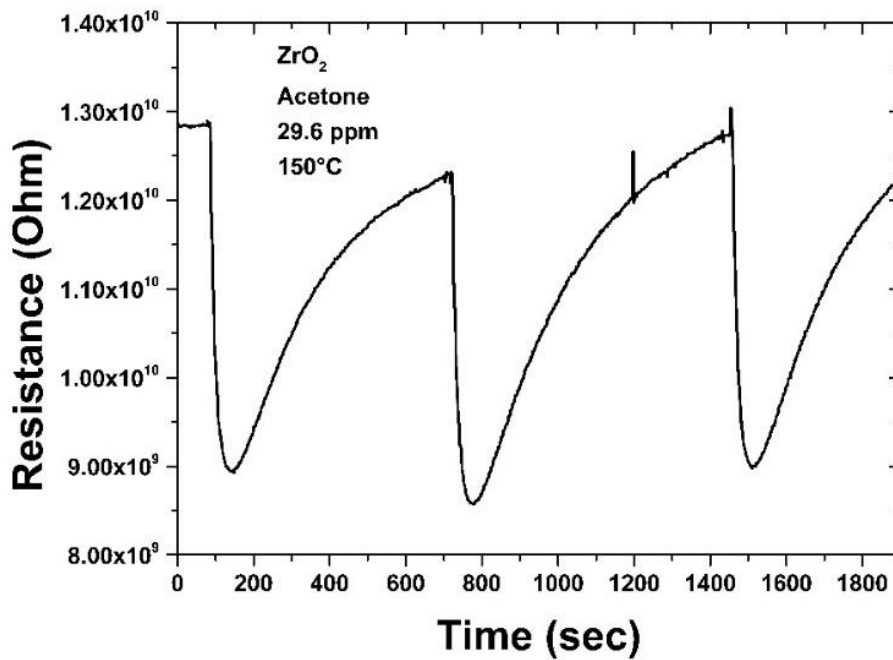


Fig. 26 Zirconium oxide response to acetone, for a concentration of 29.6 ppm and a sensor temperature of 150°C

Analogous results were found for higher operating temperatures. Fig. 27 shows a similar pattern of response following the interaction with acetone, at 300°C. In this case, the acetone concentration was 296 ppm, and the volatile was injected three times into the sensor system.

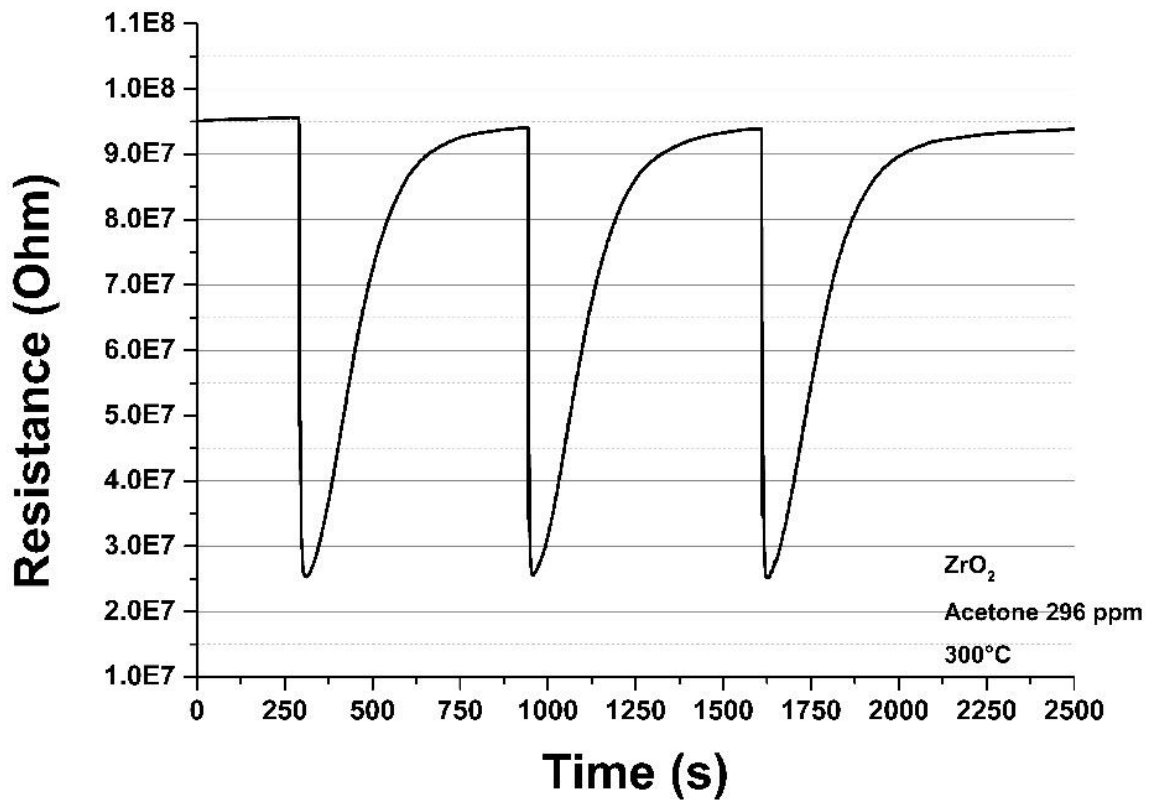


Fig. 27 ZrO_2 response to three injections of acetone (296 ppm). In this case, the operating temperature was set at 300°C

An overview of the sensor percentage resistance response to acetone (still at 296 ppm) as a function of the temperature is reported in Fig. 28. The error bars reported in this figure (as well as the one in the following sections) refer to the error value calculated according to Equation 9.

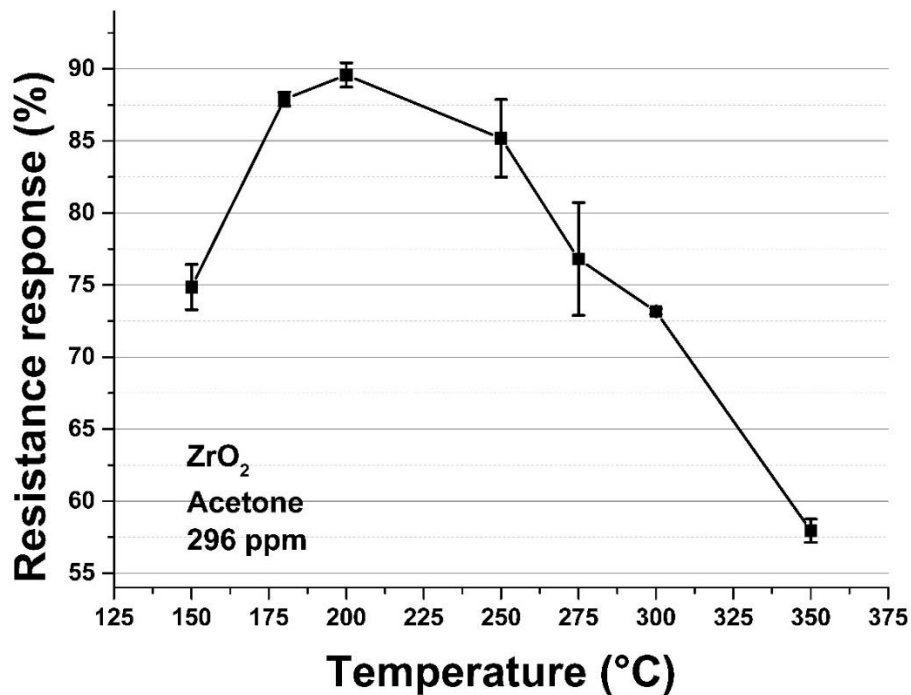


Fig. 28 The resistance response showed a great dependence to the temperature. The resistance behaviour as a function of the operating temperature showed that the best sensor performances, in terms of sensitivity, corresponded with 200°C. The graph refers to 296 ppm of acetone.

This graph is of particular importance since it allows us to estimate the ideal operating temperature; in other words, to establish at which temperature the sensor gave the best response to acetone. In the undoped zirconium oxide case, this temperature (T_{MAX}) was 200°C. The zirconium oxide sensor showed an analogous behaviour towards acetone at lower concentrations. Fig.29 shows the sensor response as a function of the temperature when testing to a concentration of 2.96 ppm.

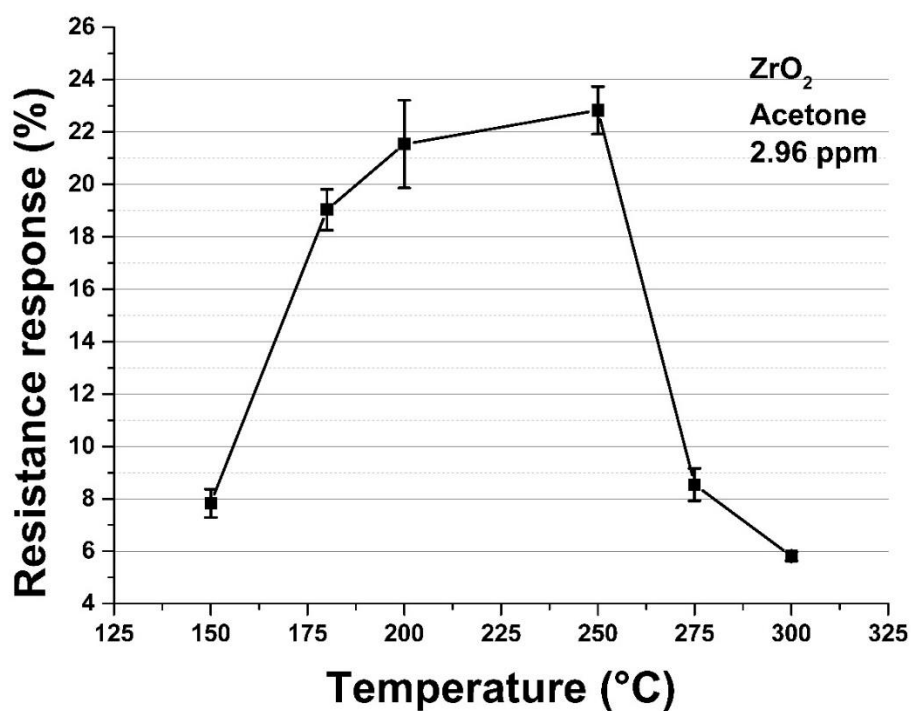


Fig. 29 Temperature dependence of the ZrO₂ response following the interaction with acetone. In this case, the concentration was lower (2.96 ppm).

Although the magnitude of response is small as expected, we can observe that the T_{MAX} was reached in the range 200-250°C, in agreement with the results presented in Fig. 28. Similar comparisons were made for ethanol. The sensor response to ethanol as a function of the temperature is shown in Fig.

30.

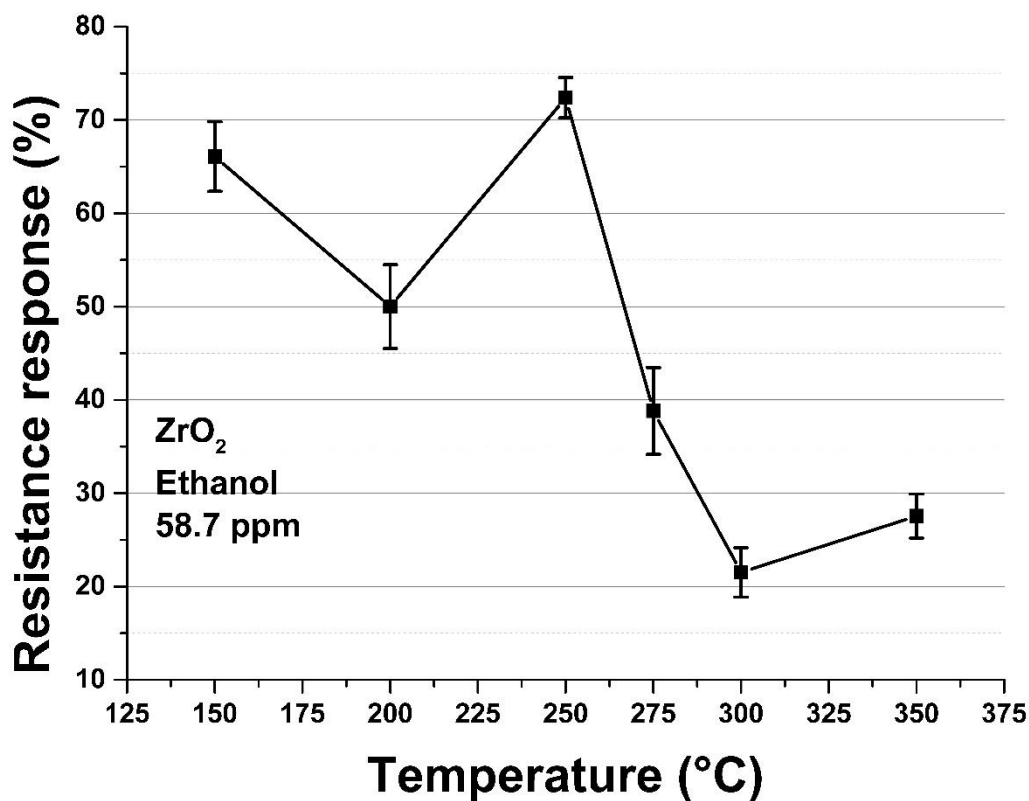


Fig. 30 ZrO₂ response to 58.7 ppm at the different operating temperatures at which the sensor was tested

Also, zirconium oxide showed a higher response to ethanol than acetone in terms of resistance change. Fig. 31 makes a comparison between the temperature profile of the response for acetone (29.6 ppm, black trace), ethanol (58.7 ppm, red trace), and water (31.2 ppm, blue trace). These specific dilutions of acetone and ethanol were obtained from headspace concentrations of these volatiles. These values are relatively close dilutions of the same magnitude.

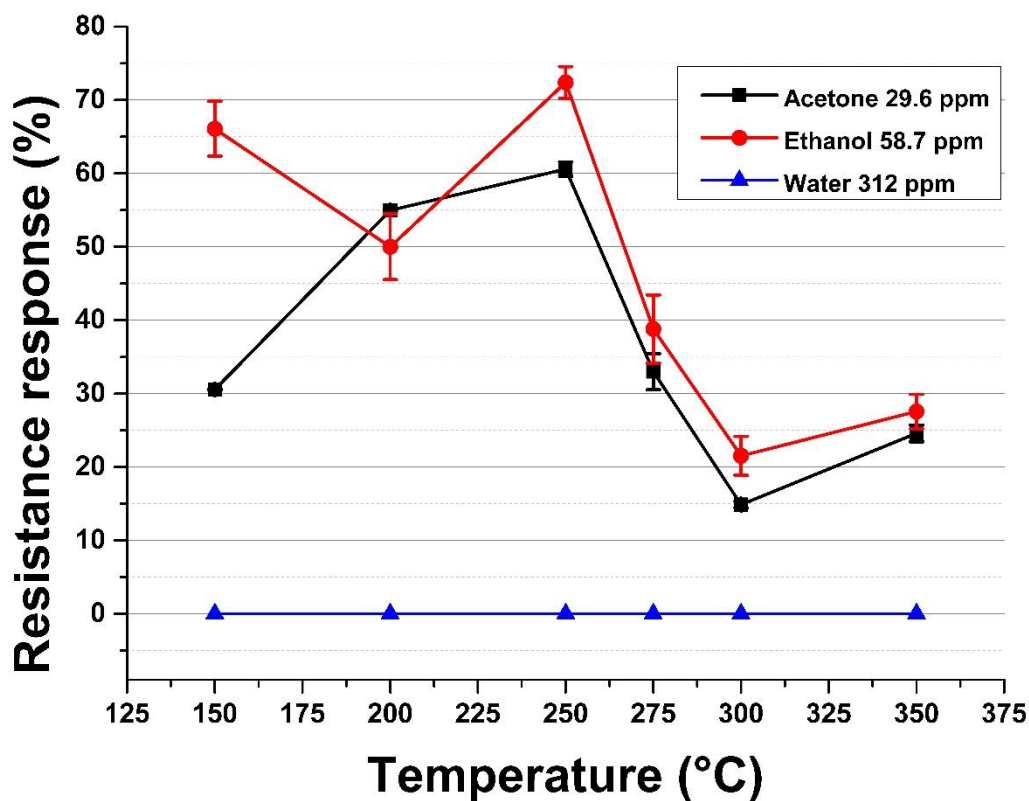


Fig. 31 Comparison of the temperature dependence of the sensor response when tested to acetone, ethanol, and water.

The series of volatiles related to explosives were also tested, and their response at various temperatures (range 150-250°C) is shown in Fig. 32. In this case, the sign of the resistance response was also reported. In particular, the interaction of the zirconium oxide sensor with nitroglycerine (0.63 ppm, reported in yellow in the graphic) and ethylene glycol dinitrate (0.63 ppm, grey) was followed by an increase in the sensor resistance. On the other hand, 2,4-dinitrotoluene (0.54 ppm, orange) and 2,3-dimethyl-2,3-dinitrobutane (blue) both caused a decrease in the resistance response. The best overall performances corresponded with the temperature range of 180°C, while the sensor did not show significant changes of resistances for $T > 250^{\circ}\text{C}$ for these four compounds.

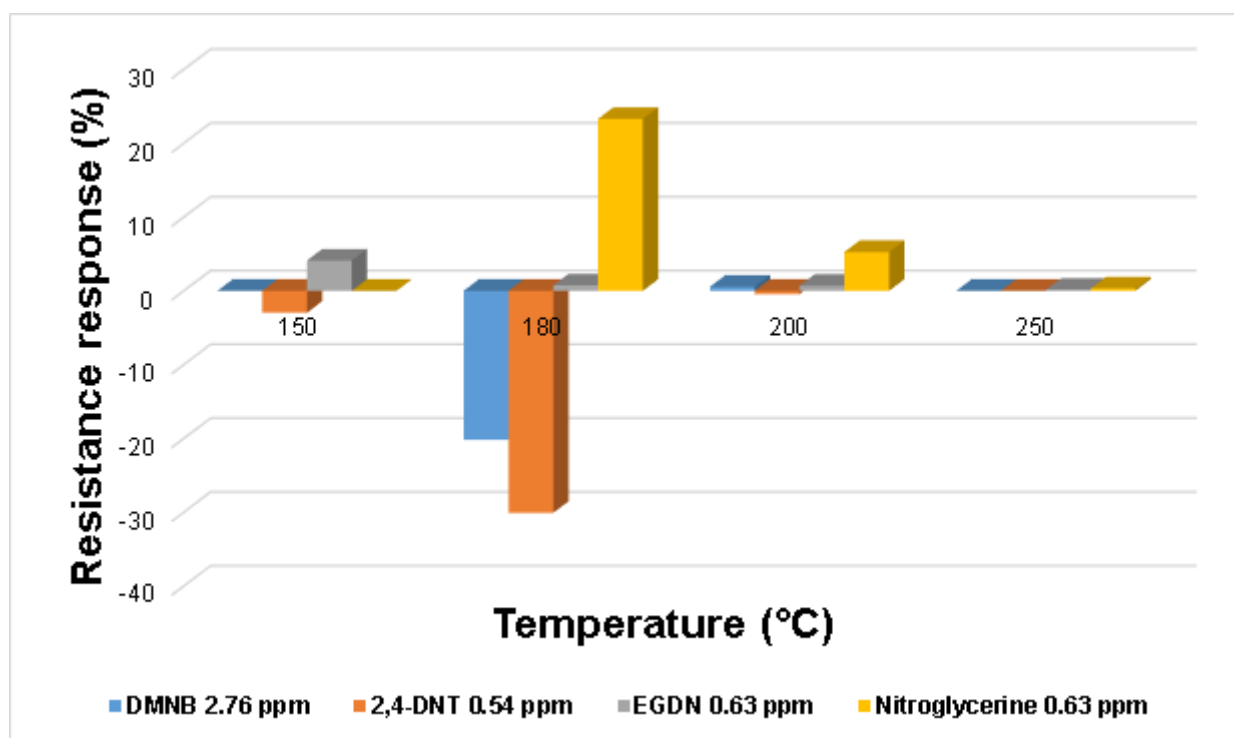


Fig. 32 Zirconium oxide response to some explosive linked compounds at different operating temperatures. ZrO₂ showed the best response to 2,4-DNT at 180°C

3.4.2 ZrO₂ - Cataluminescence (CTL) experiments

Fig. 33 shows the sensor response to acetone at the operating temperature of 150°C: The graph shows the fast response time and the high repeatability of the response. These characteristics are regular features of the cataluminescence experiments. Similarly, to the resistance experiments, the CTL signal increases with an increase in the analyte concentration, as Fig. 34 shows

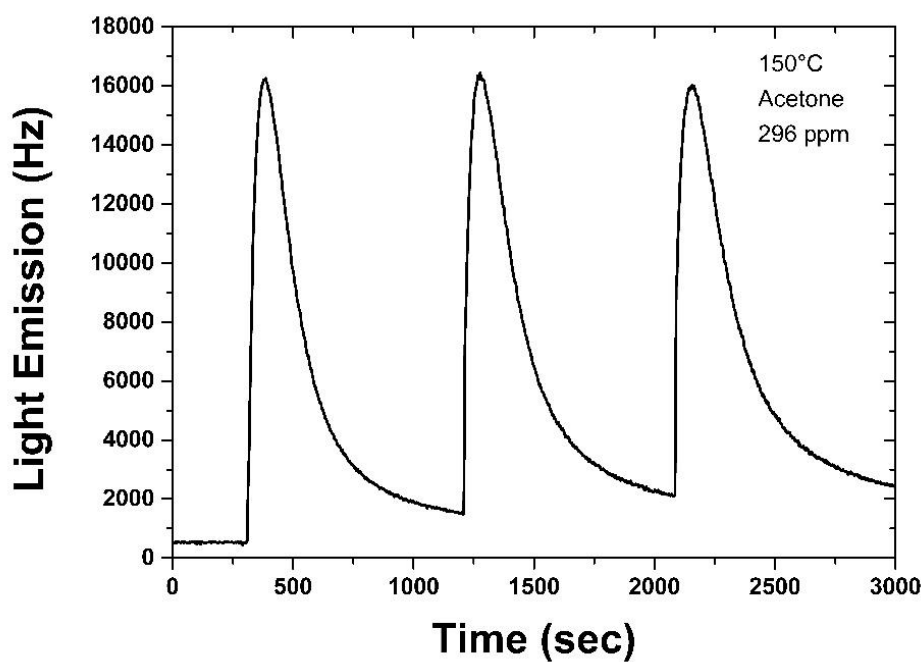


Fig. 33 ZrO_2 CTL signal when interacting with 296 ppm of acetone. This volatile was injected three times in the system, leading to the characteristic three peaks that we can observe above

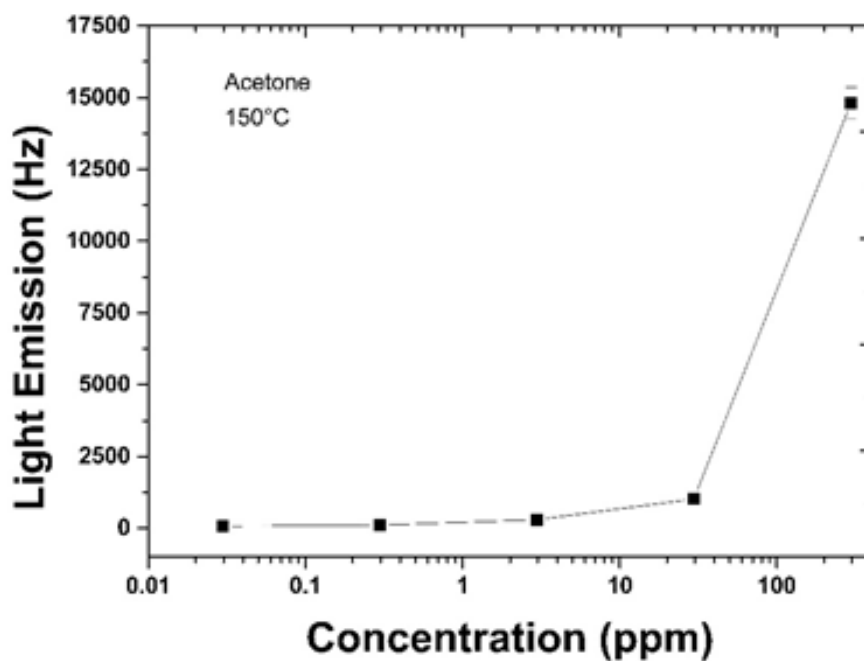


Fig. 34 Concentration dependence of the CTL from the zirconium oxide with a linear fit. The signal increases with the concentration rise.

The same pattern recurred for the higher temperature investigated. As an example, Fig. 35 shows the concentration dependence of the CTL response at the operating temperature of 300°C.

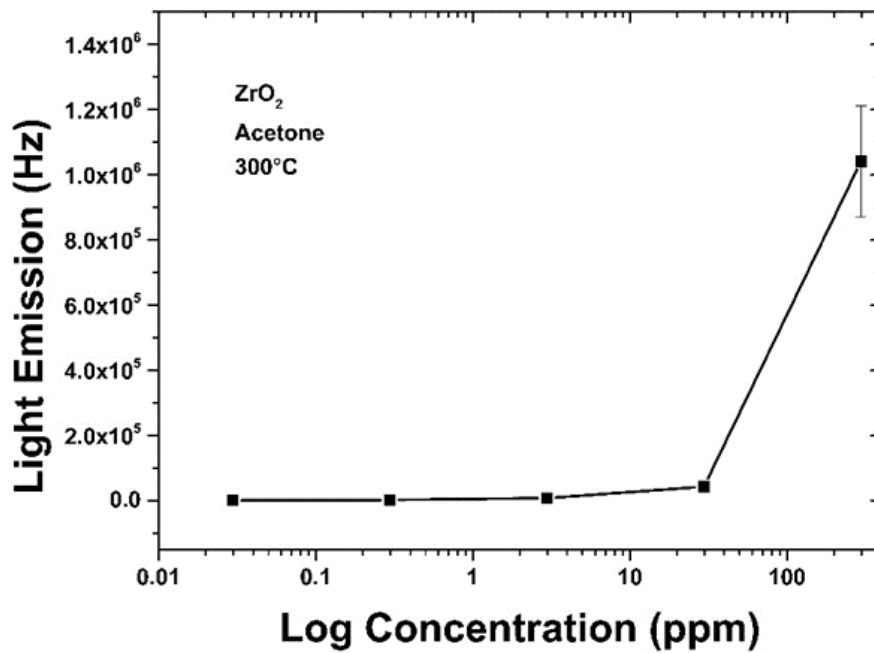


Fig. 35 Concentration dependence of the ZrO₂ light emission (acetone) and linear fit. The operating temperature, in this case, was 300°C

It is interesting to establish whether it is possible to identify a T_{MAX} for the light emission, which is to say, a temperature giving the best CTL response. Fig. 36 shows the light emission signal for acetone as a function of the temperature at the fixed value of the concentration of 296 ppm.

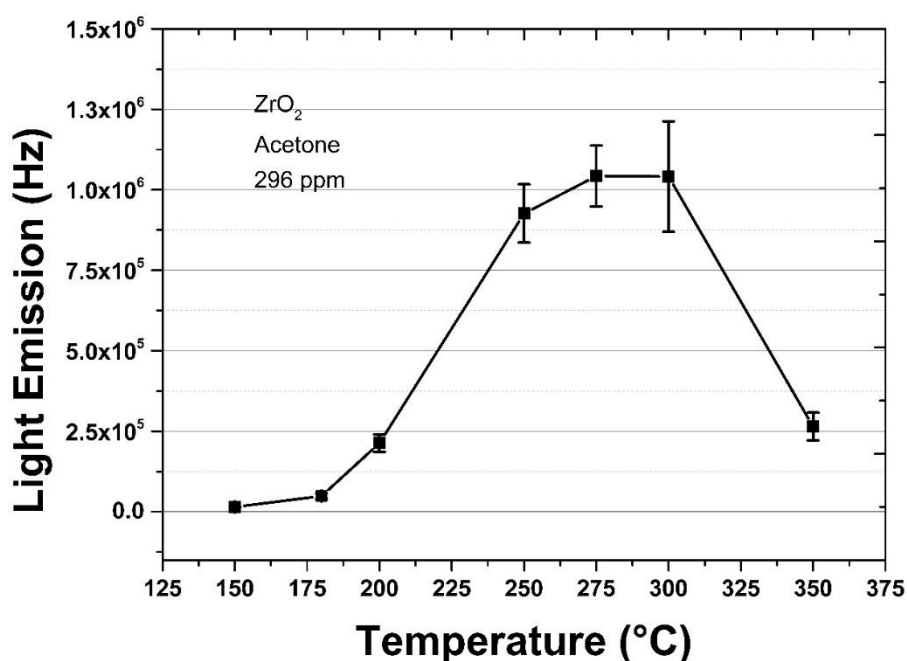


Fig. 36 Temperature dependence of the CTL response to acetone (296 ppm) for the undoped zirconium oxide. The best sensitivity is achieved in the range 275-300°C

From the above plot, it is possible to observe that the best sensor performances, in terms of response, increased with the increasing operating temperature, and reached a broad peak at a temperature range spanning 275-300°C and then decreased again at higher temperatures. Thus, the optimum CTL response is reached at 275°C. This is also the case when considering lower concentrations of acetone. In particular, Fig. 37 shows the light emission response as a function of the temperature at an acetone concentration of 2.96 ppm.

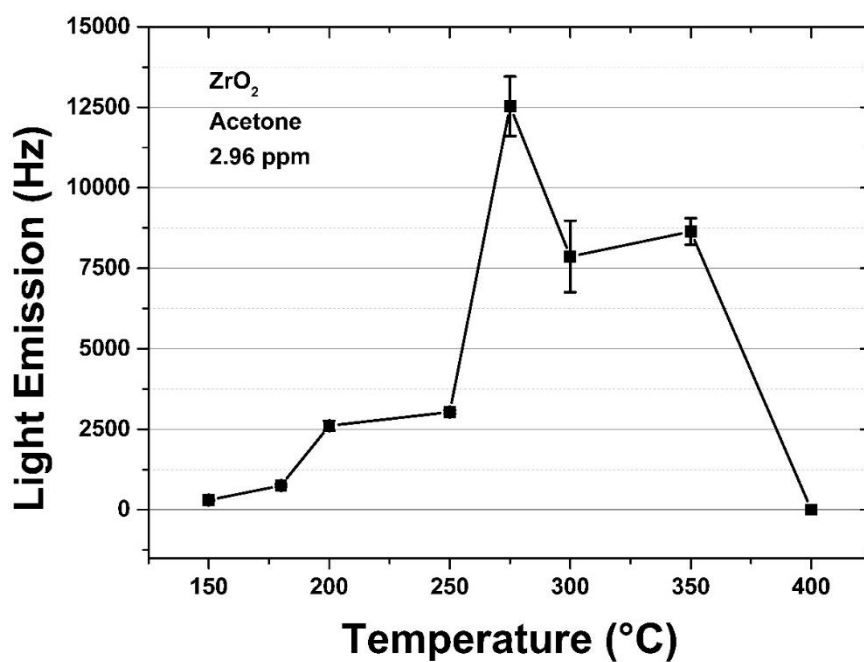


Fig. 37 In the case of lower concentrations (2.96 ppm), ZrO₂ showed the best cataluminescent response at 275°C

A similar behaviour was found for ethanol (58.7 ppm), which is reported in Fig. 38. Although for ethanol the T_{MAX} for the cataluminescent response at this concentration is lower 250°C.

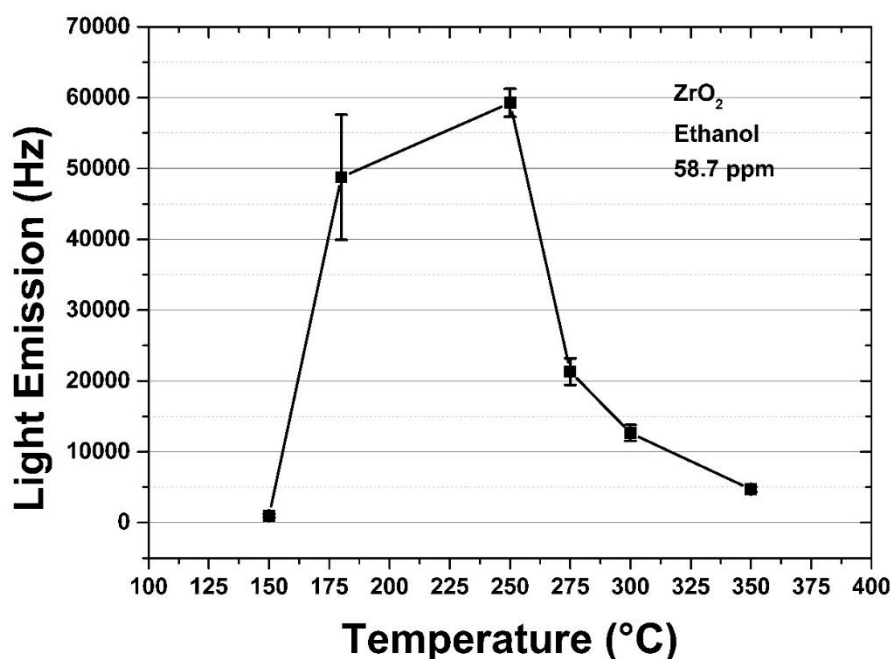


Fig. 38 CTL signal produced by the zirconium oxide sensor when exposed to ethanol (58.7 ppm) as a function of the temperature. The best response was at 250°C

A series of other compounds were tested against the ZrO₂ sensor. In particular, Fig. 39 shows the temperature dependence of the sensor response following the interaction with 2,4-dinitrotoluene (2,4-DNT). The concentration of this compound was 0.54 ppm. The reduction of response to zero after 275°C is likely to be a function of the BBR increasing and the low overall response to 2,4-DNT. The low response to 2,4-DNT is in part due to the lower concentrations used for the experiments due to the use of headspace concentrations which are limited by the low vapour pressure of 2,4-DNT.

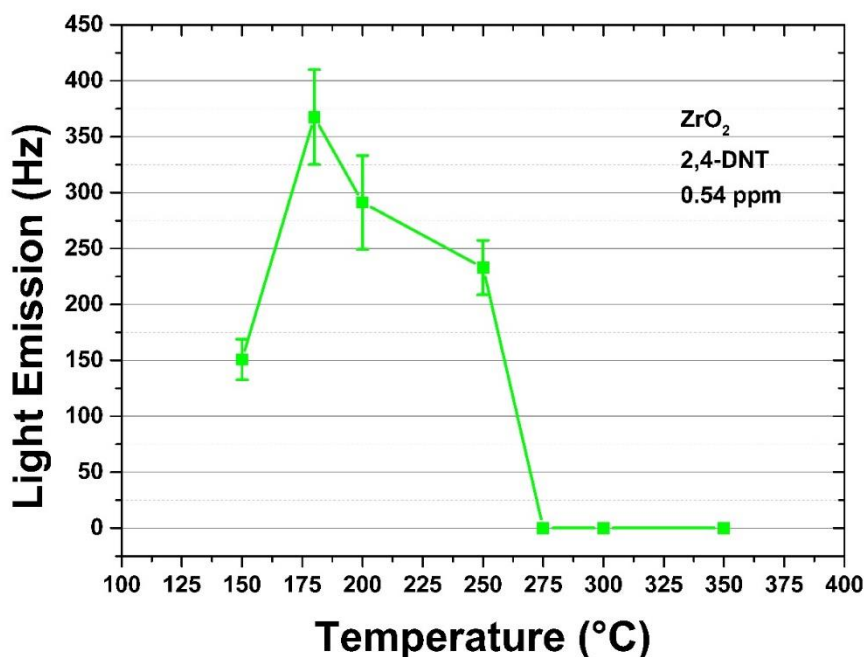


Fig. 39 Temperature profile of the light emission response to 2,4-dinitrotoluene (T_{MAX} at 175°C)

The temperature value giving the best performance in terms of CTL was observed at 175°C. Also, it is possible to affirm that explosives gave a lower CTL response in general if compared with the one from ethanol even when considering the differences in concentration. This characteristic is confirmed by Fig. 40, showing the light emission from comparable concentrations of 2,4-DNT (0.54 ppm, black trace) and ethanol (0.587 ppm, red trace). Fig. 41 shows the experiments conducted on another explosive compound, DMNB (2.76 ppm).

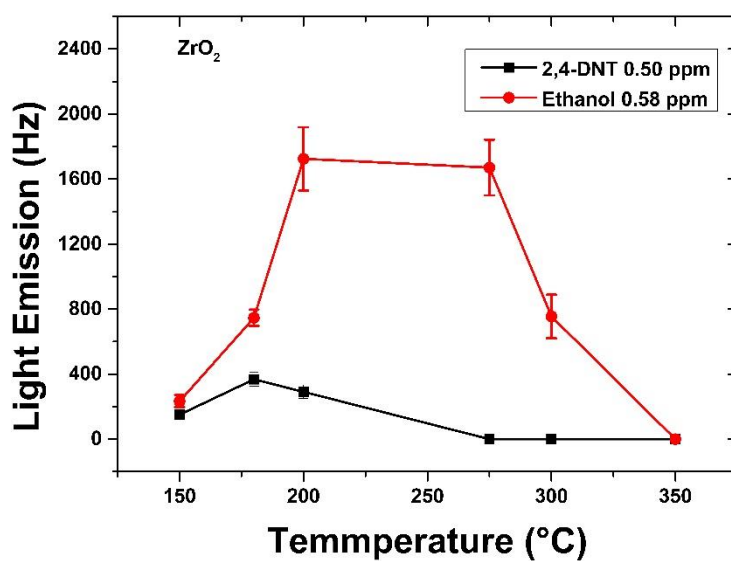


Fig. 40 Comparison between the CTL response to ethanol (red trace) and 2,4-dinitrotoluene (black trace), as a function of the operating temperature.

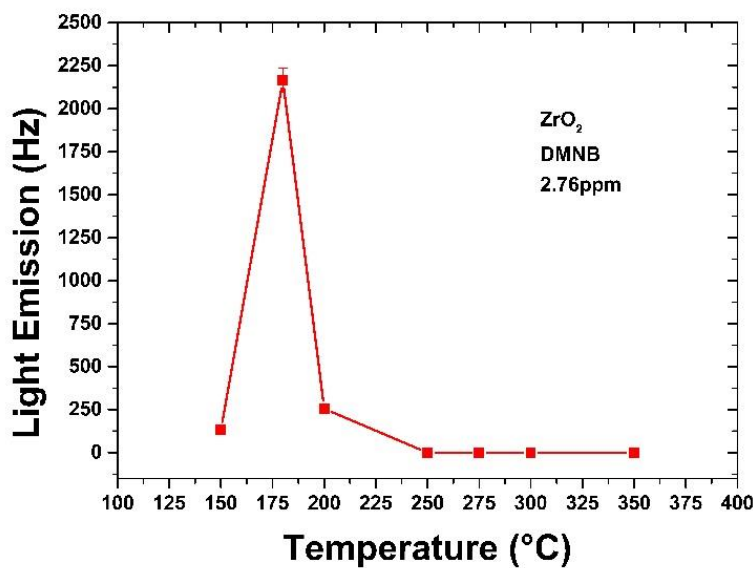


Fig. 41 Zirconium oxide response to 2,3-Dimethyl-2,3-dinitrobutane (DMNB) at different temperatures. The best performances corresponded to 180°C

Analogous with what was observed for 2,4-DNT, the T_{MAX} for DMNB occurred at 175°C. Nitroglycerine (0.63 ppm) was also tested, exhibiting a CTL response with temperature profile shown in Fig. 42.

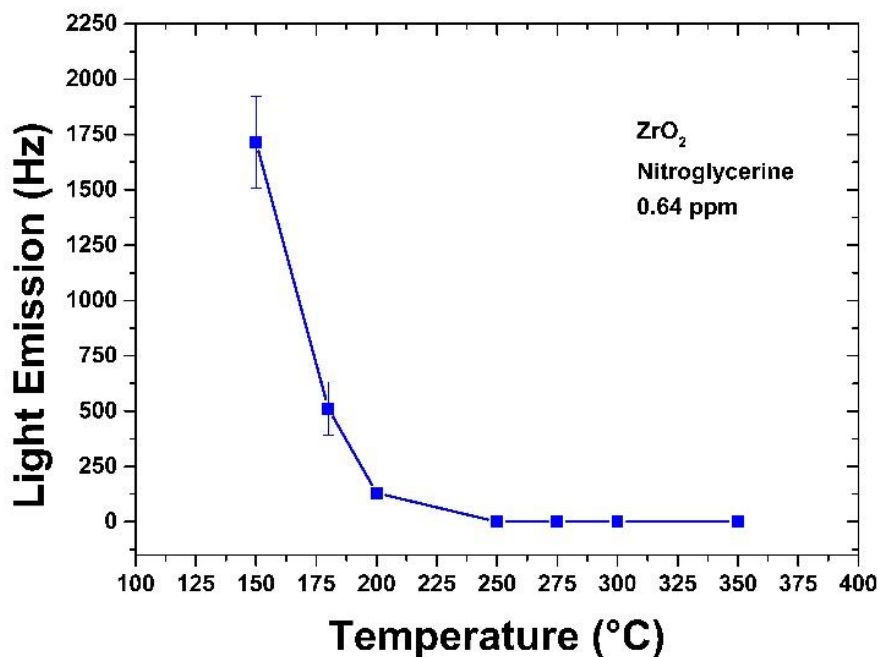


Fig. 42 ZrO_2 light emission response to nitroglycerine (NG) at all the temperature tested. The best performances corresponded to 150°C.

Interestingly, NG displayed the best response at the lowest temperature tested, which is to say at 150°C, while in conditions of higher operating temperature, the signal decreases. Again, this might be partly attributed to the increase in the BBR vs. the low overall response to the explosive linked compounds partly based on their low vapour pressure. It should be noted that testing to NG at lower temperatures may elucidate an actual T-max value.

Therefore, it is helpful to show (Fig. 43) an overall comparison of the CTL responses from different volatiles. The graph shows that the sensor did not produce any significant light when exposed to water headspace (blue trace) for all the temperatures tested. Regarding 5.87 ppm of ethanol, the light emission response increased alongside the temperature increase, reaching a peak at 250°C (which can

be identified as the T_{MAX}) and then decreasing for $T > 250^{\circ}C$. In the acetone case, an analogue pattern was observed (2.96 ppm, black trace), and the maximum response value corresponded with the $275^{\circ}C$.

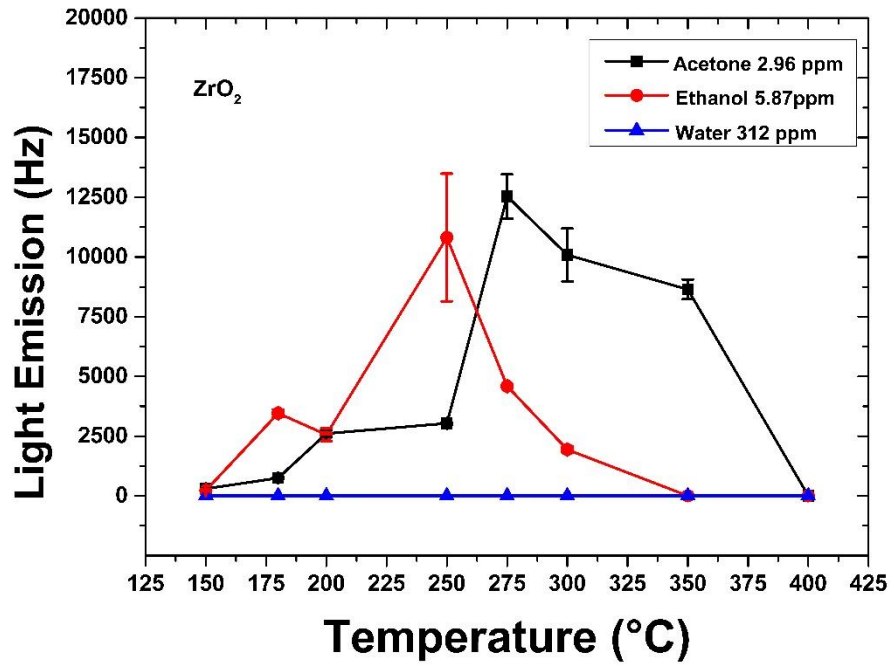


Fig. 43 Comparison of the undoped zirconium oxide response to acetone, ethanol and water as a function of the temperature.

3.5 Europium-doped zirconium oxide sensor ($\text{ZrO}_2:\text{Eu}^{3+}(5\%)$)

3.5.1 $\text{ZrO}_2:\text{Eu}^{3+}(5\%)$ - Resistance experiments

The concentration dependence of the resistance response was also observed for the europium-doped zirconium oxide. In particular, Fig. 44 shows the resistance response to acetone as a function of the volatile concentration (from 0.296 ppm to 296 ppm). The operating temperature to which the graph refers was 300°C.

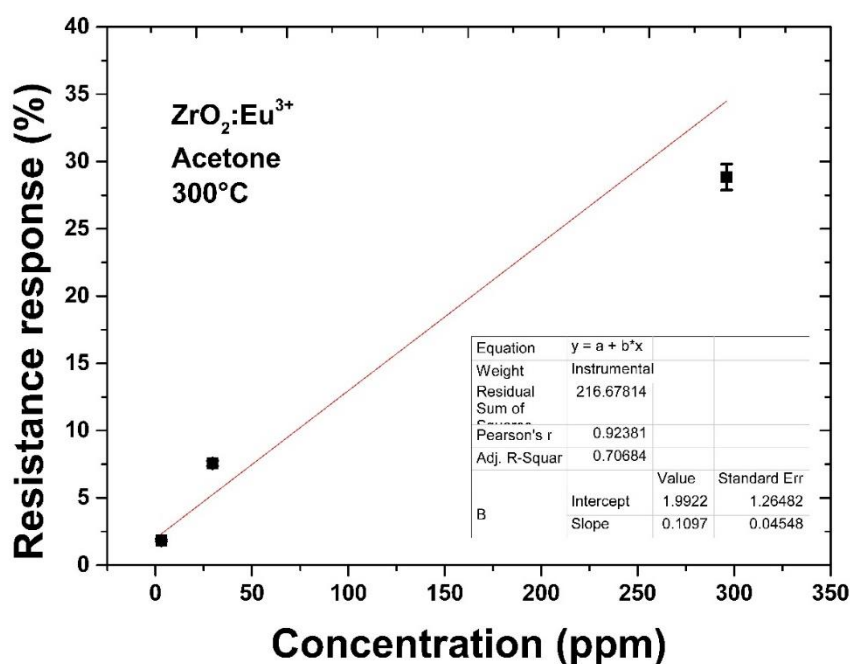


Fig. 44 Resistance dependence of acetone concentrations at 300°C. The concentration is reported in a logarithmic scale

The experimental design for the $\text{ZrO}_2:\text{Eu}^{3+}(5\%)$ was the same employed for the undoped-oxide. Nevertheless, the first aspect that we have to underline when considering the $\text{ZrO}_2:\text{Eu}^{3+}(5\%)$ sensor is the positive resistance response to the volatiles investigated, in line with the behaviour of a p-type material. For example, Fig. 45 shows three subsequent injections of acetone (296 ppm) at the operating temperature of 300°C. To be noticed that the interaction with acetone caused an increase

of the material resistance (p-type material). This behaviour is opposite to the response of the undoped ZrO₂ sensor.

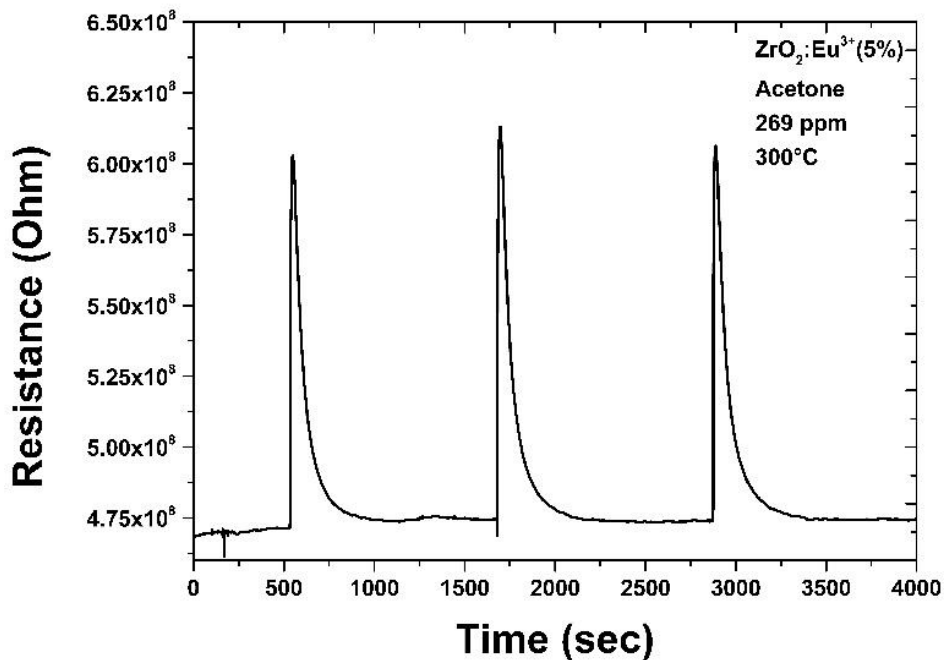


Fig. 45 ZrO₂:Eu³⁺ resistance following three subsequent injection of acetone (296 ppm, the highest concentration investigated). Operating temperature of 300°C.

As with the undoped sensor the doped sensor was tested at a range of temperatures. Therefore, it is possible to display the temperature profile of the resistance response for a given volatile concentration. Fig. 46 shows the temperature dependence of the sensor response when exposed to 29.6 ppm of acetone.

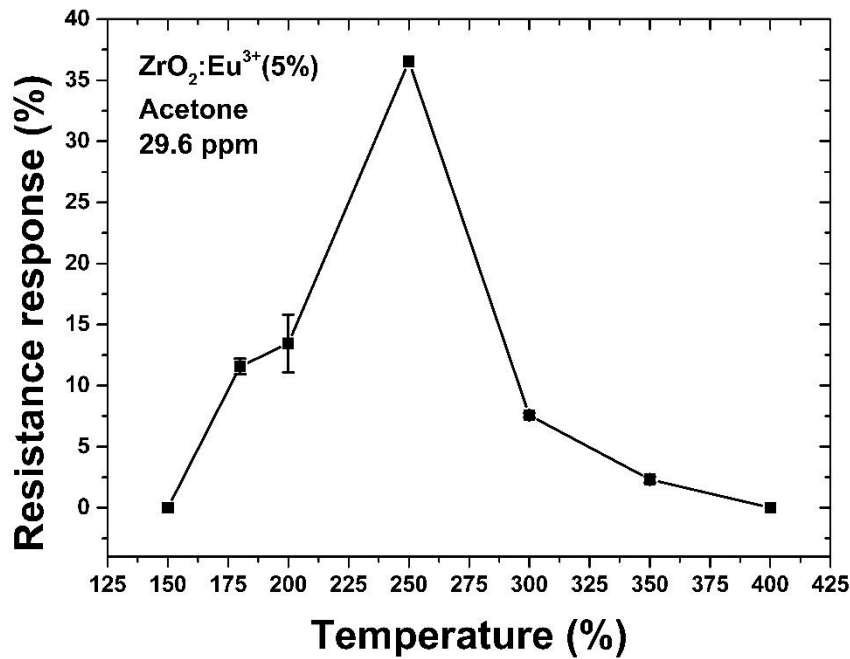


Fig. 46 Temperature dependence of the resistance response to acetone (29.6 ppm) in the europium-doped zirconium oxide case.

We can observe the expected pattern for the resistance experiment as a function of the temperature. The low increase of the signal at a temperature slightly above 100°C, the reaching of a T_{MAX} and the successive decrease for $T > T_{MAX}$. The T_{MAX} observed was 250°C for the doped sensor.

Ethanol was also tested, and Fig. 47 shows the raw data (resistance change as a function of time) relative to three injections of 58.7 ppm at the given temperature of 250°C. Fig. 48 describes the resistance response profile of the doped sensor when exposed to ethanol vapour over a range of temperatures

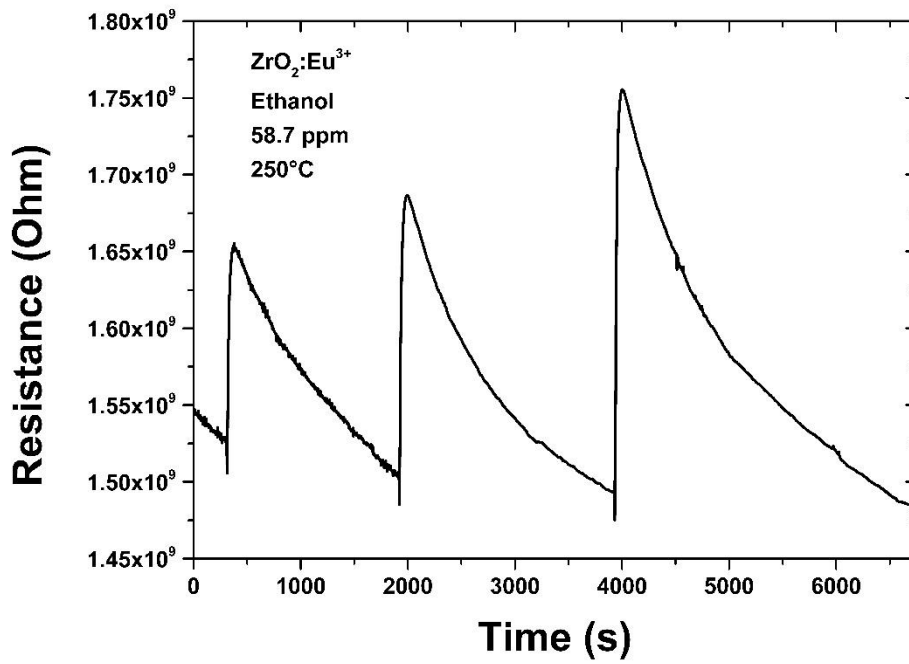


Fig. 47 Europium-doped ZrO_2 resistance response following three consecutive injections of ethanol (58.7 ppm).

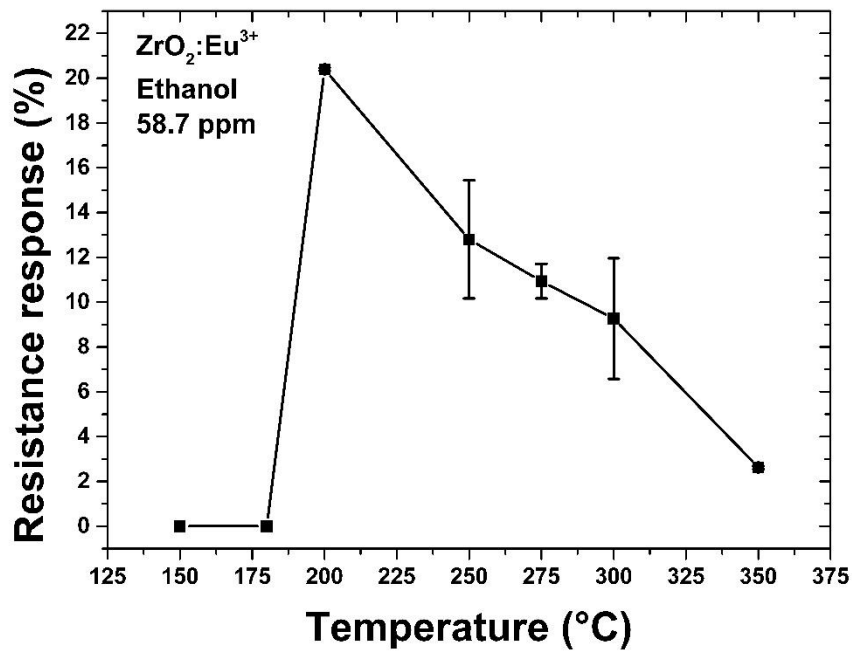


Fig. 48 $ZrO_2:Eu^{3+}$ (5%) Resistance response to ethanol (58.7 ppm) at different temperatures

In this case, the best sensor performance in terms of response to ethanol was reached at 200°C. It is interesting to compare the response for different volatiles. Specifically, Fig. 49 shows the response of the europium-doped zirconium oxide over the temperature range studied when exposed to acetone (29.6 ppm), ethanol (58.7 ppm), and water (31.2 ppm)

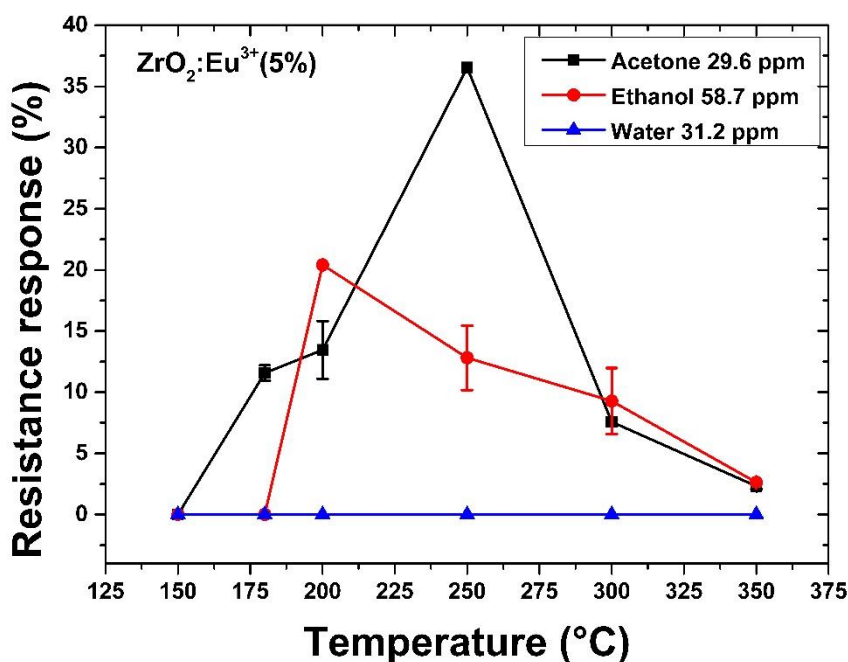


Fig. 49 Comparison of the resistance response displayed by the europium-doped zirconium oxide sensor at different temperatures

Acetone showed the best overall response in the sensor under investigation, except at a temperature of 200°C, which corresponds to the T_{MAX} for the ethanol response. The sensor did not give any significant response to water at any of the temperatures investigated.

3.5.2 $ZrO_2:Eu^{3+}(5\%)$ - Cataluminescence (CTL) experiments

This section contains the light emission experiments for the europium-doped zirconium oxide. As was observed for the resistance change, the light emission signal is dependent on the concentration. Fig. 50 shows the CTL response profile at various acetone concentrations, starting from 0.296 ppm up to 296 ppm, at the operating temperature of 250°C

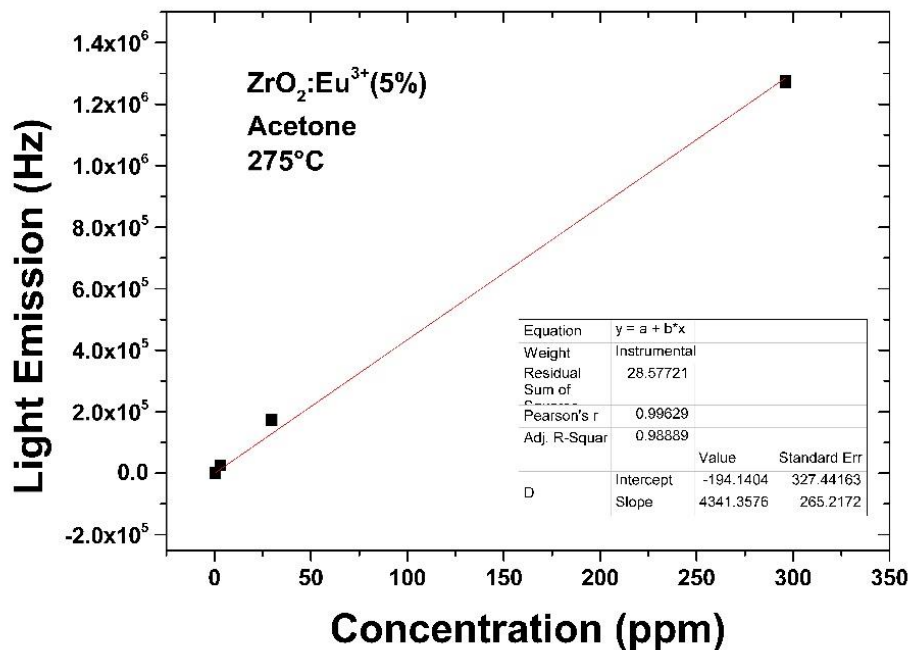


Fig. 50 Light emission as a function of the acetone concentration. The substrate temperature was 275°C

Analogous to the resistance, the light emission is repeated in the temperature range 150°C-400°C. As a matter of example, Fig. 51 reports the sensor response to three injections of acetone (296 ppm) at 300°C.

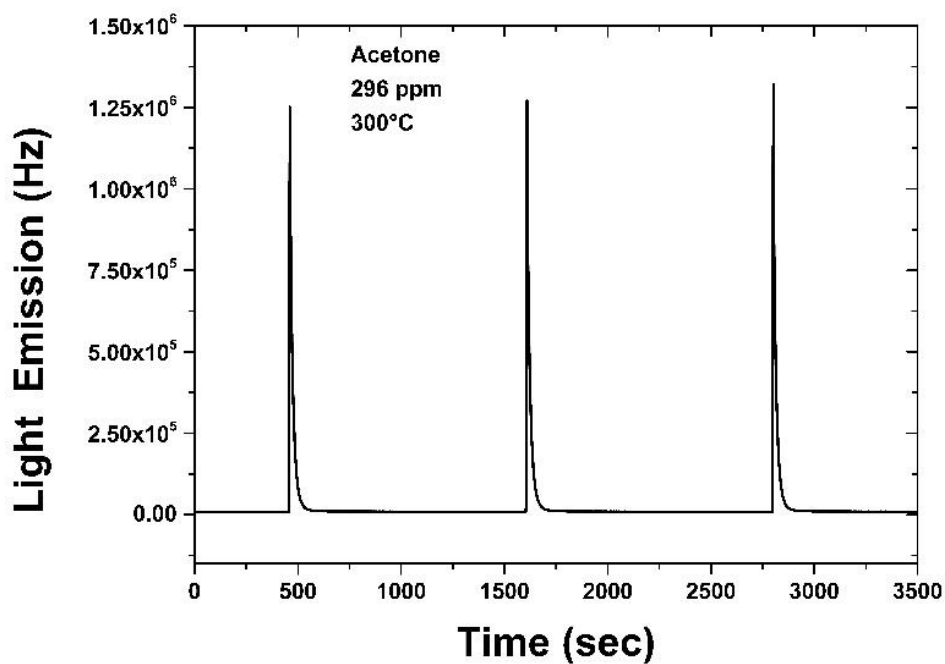


Fig. 51 ZrO₂:Eu³⁺(5%) response to three following injections of acetone (296 ppm) at 300°C. Note the good sensor performances under these conditions: sharp shape of the peak, meaning a good sensor sensitivity, a relatively fast response and recovery time

We can observe the high repeatability of the CTL signal. The signal dependence of the temperature is reported in Fig.52, showing the profile from acetone (29.6 ppm), ethanol (58.7 ppm), water (31.2 ppm).

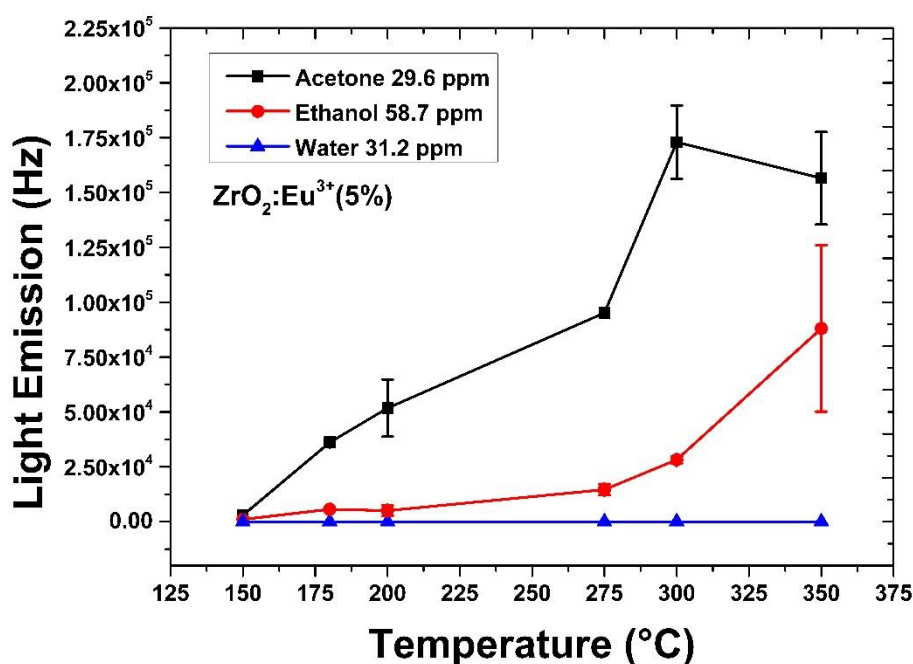


Fig. 52 ZrO₂:Eu³⁺(5%) light emission response to different volatiles at the temperature investigated. This sensor showed the best performances when exposed to acetone, especially at 300°C.

We can notice an overall better sensor response following the interaction with acetone, which showed the best response (T_{MAX}) at 300°C. Ethanol reached the best responses at 350°C although it is possible that T_{MAX} has not been identified in the temperature range studied. The sensor did not respond to water, as expected from previous CTL experiments. Also, the explosive linked compounds were tested with ZrO₂:Eu³⁺(5%). The CTL response for Nitroglycerine and 2,3-dimethyl-2,3-dinitrobutane against the temperature are reported in Fig. 53(a) and Fig. 53(b) respectively. Nitroglycerine showed the best response at a temperature of 300°C, while for DMNB the best response was at 350°C.

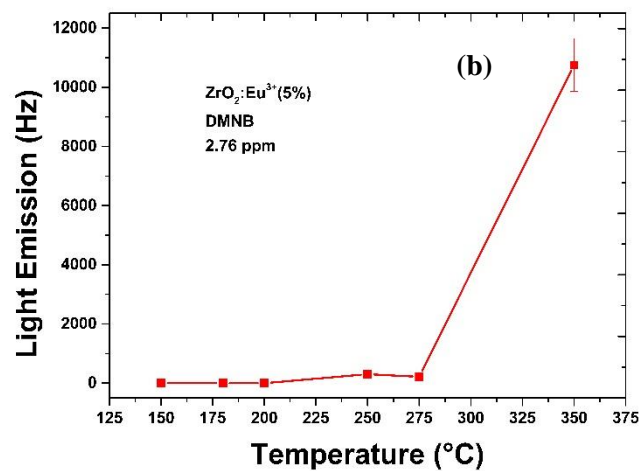
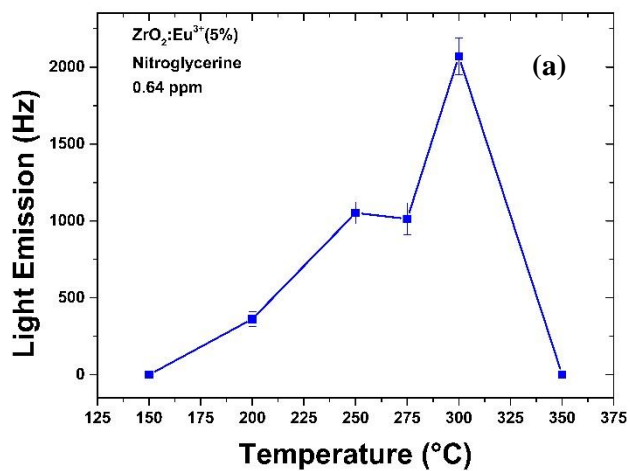


Fig. 53 ZrO₂:Eu³⁺ (5%) light emission response as a function of the operating temperature. In particular to (a) nitroglycerine and (b) 2,3-dimethyl-2,3-dinitrobutane

3.6 Tungsten oxide sensor (WO_3)

3.6.1 WO_3 - Resistance experiments

The tungsten oxide resistance response for acetone (29.6 ppm) at a sensor temperature of 350°C is shown in Fig. 54. As a well-known n-type semiconductor, tungsten oxide gave a decrease in the resistance due to the interaction with acetone.

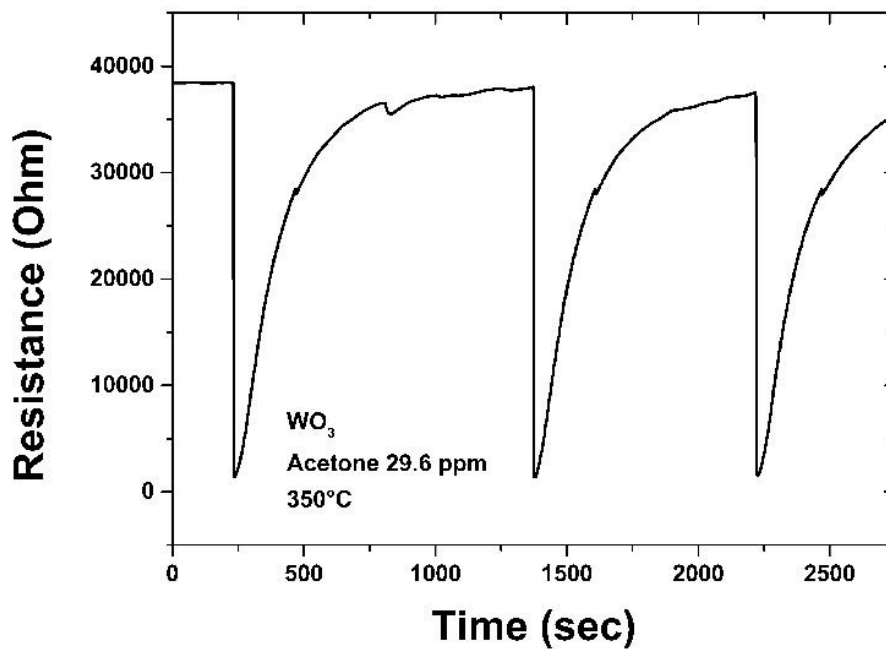


Fig. 54 WO_3 resistance response to acetone (29.6 ppm) at 350°C

The experiments were repeated in the temperature range 150°C - 400°C for the WO_3 sensor. The resistance profile as a function of the temperature is reported in Fig. 55 for acetone (29.6 ppm), ethanol (58.7 ppm), and water (31.2 ppm). The WO_3 sensor showed the best performances when exposed to acetone. The T_{MAX} to acetone was 350°C for the WO_3 sensor. The sensor response to ethanol as a function of the temperature, in this case, does not follow the expected bell-shaped pattern. This seems to be a not-expected behaviour, either when compared to the literature and the other experimental data present in this thesis work.

The WO_3 sensor showed a significant response for DMNB, as shown in Fig. 56. The sensor, in this case, reached its T_{MAX} at 275°C . This follows the trend observed previously of lower T_{MAX} values for explosive linked compounds. This means that the operating temperature can be selected to accentuate the response to target compounds vs. potential interferences.

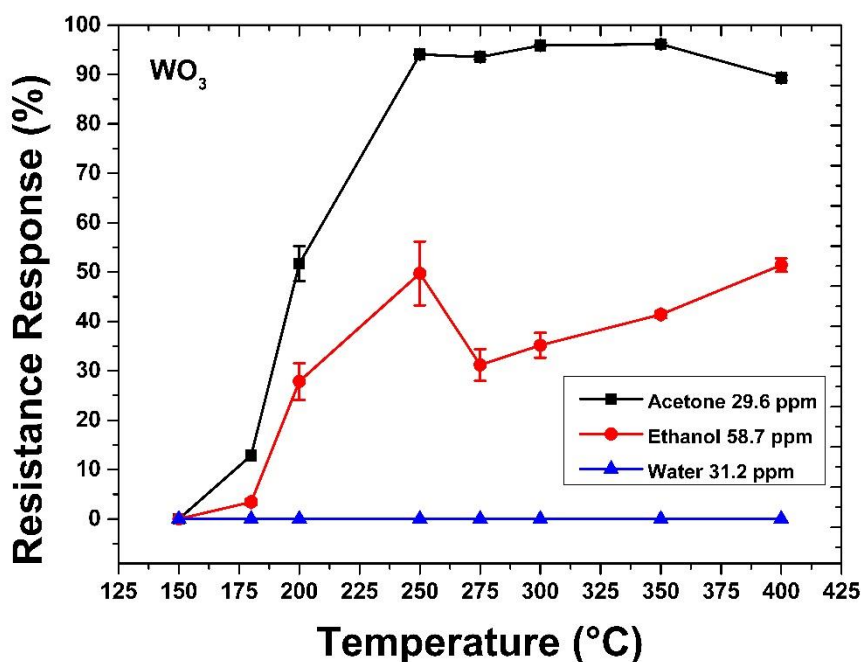


Fig. 55 Resistance response showed by the tungsten oxide sensor at different operating temperatures. The graph emphasises the comparatively large response to acetone (black trace in the graph) when compared with ethanol (red trace) and water (blue trace) to which the sensor did not respond

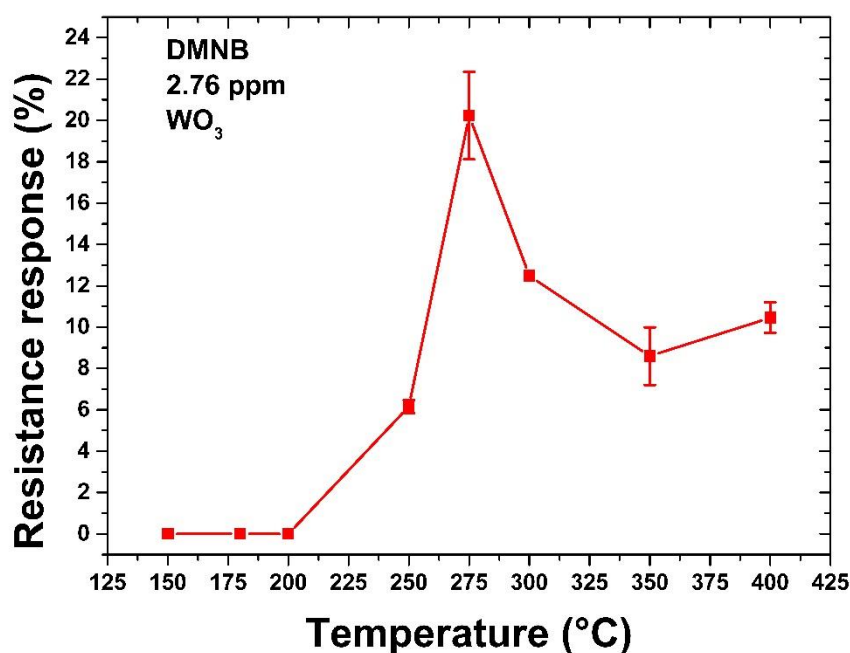


Fig. 56 WO_3 response to 2,3-dimethyl-2,3-dinitrobutane in terms of electrical conductivity. The best response is identifiable at 275°C

3.6.2 WO_3 - Cataluminescence (CTL) Experiments

It was possible to obtain CTL responses for the tungsten oxide sensor. As a matter of example, Fig. 57 shows the sensor response following three injections of 296 ppm of acetone at the operating temperature of 300°C. It should be noted that although there is a light emission response this is comparatively much lower than the CTL response for the zirconium-based sensors (doped and undoped). For example, at the operating temperature of 300°C, the light emission value (following the interaction with 296 ppm of acetone) for the ZrO_2 was 1.34×10^6 Hz, while for WO_3 was 2302.23 Hz. The light emission against temperature is reported in Fig. 58, for an acetone concentration of 296 ppm.

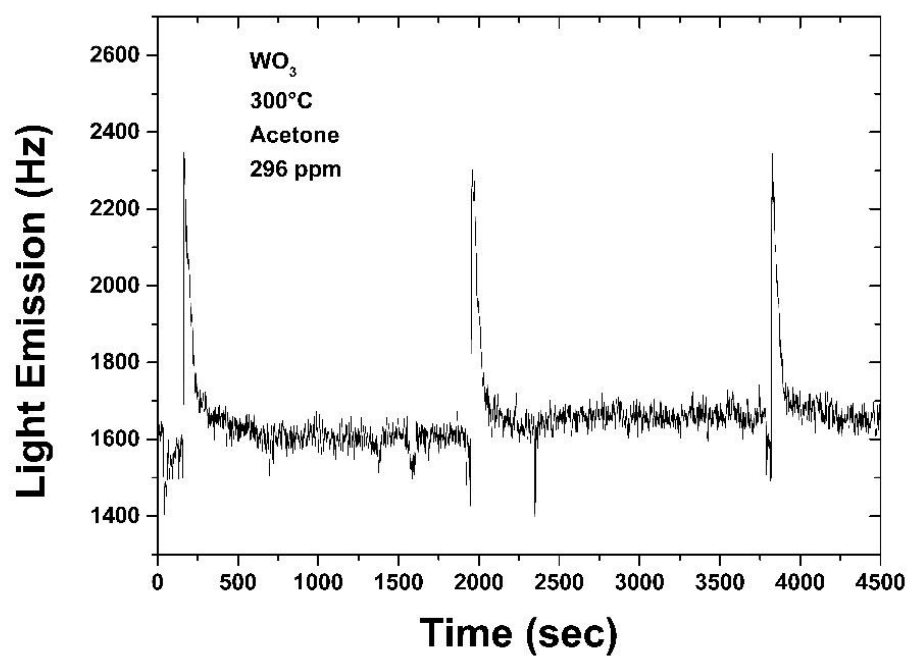


Fig. 57 Light emission produced by WO₃ when exposed to 296 ppm of acetone (three injections) at 300°C

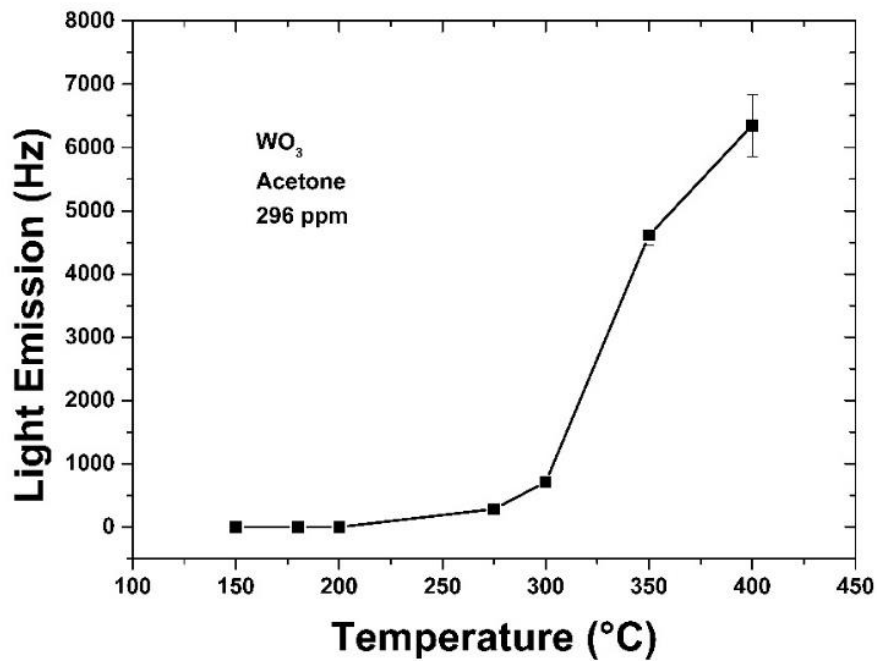


Fig. 58 Light emission showed by the tungsten oxide sensor at different temperatures.

The central aspect that we can underline is that, even at an acetone concentration of 296 ppm (the highest investigated in this project), it was possible to register the CTL only for $T > 250^{\circ}\text{C}$. Moreover, the T_{MAX} corresponded to 400°C although the sensor may not have reached T_{MAX} as this was the highest temperature studied. A complete profile of the sensor response as a function of the acetone concentration is reported in Fig. 59. In this case, the operating temperature was 350°C .

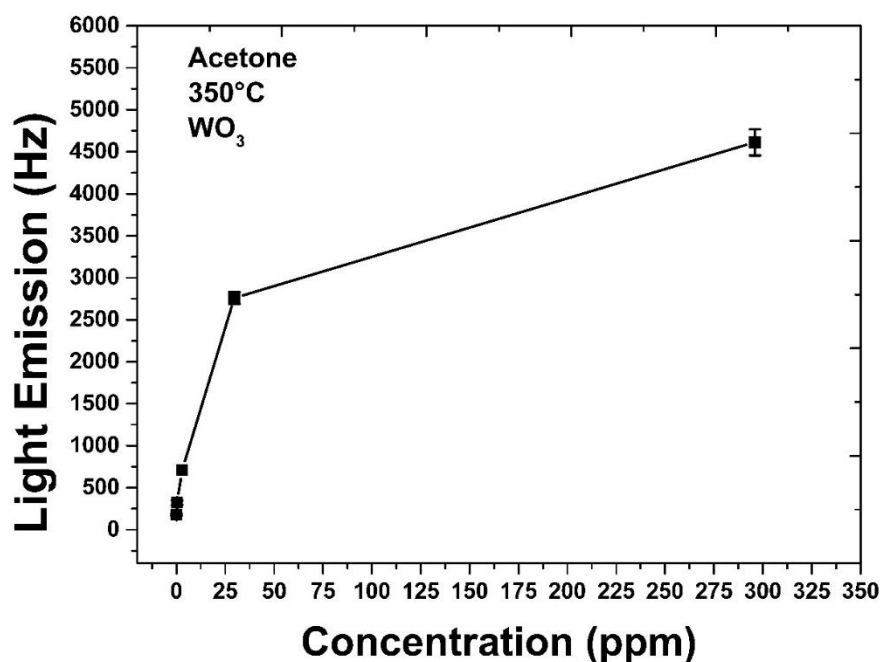


Fig. 59 Concentration dependence of the cataluminescence response in the case of the tungsten oxide sensor at the operating temperature of 350°C

The other volatile compounds and interferants were also tested. At a temperature of 400°C, the sensor responded to ethanol at the highest concentration tested (58.7 ppm). This response's intensity was 954.85 (± 38.44) Hz, and the response pattern is reported in Fig. 60. We can notice the significant background noise level due to the high black body radiation (BBR) at 400°C. Also, the CTL response for the tungsten oxide sensor is relatively low compared to zirconium-based sensors.

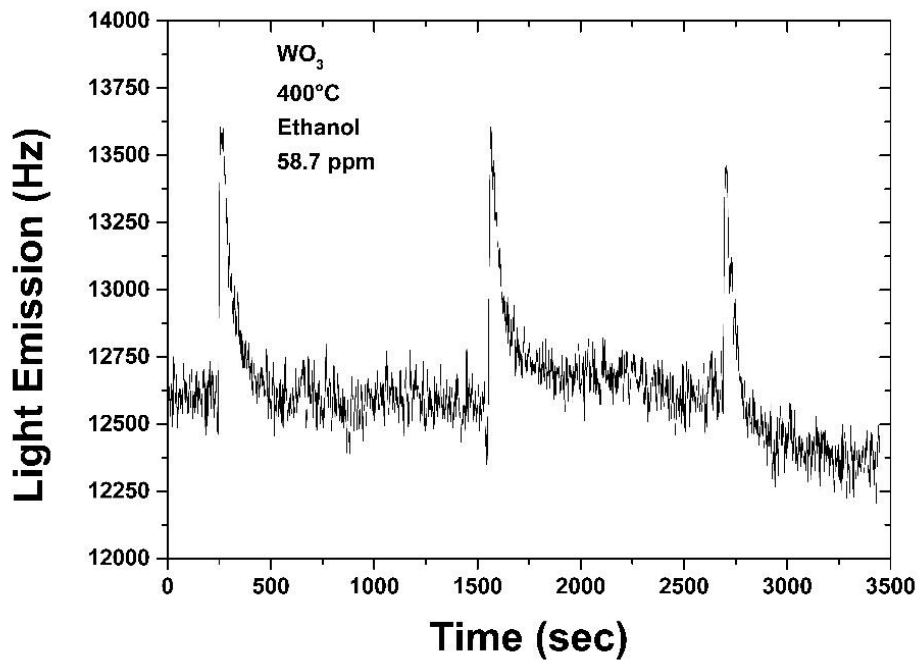


Fig. 60 Three injections of ethanol (58.7 ppm) at 400°C in the case of the WO_3 sensor

3.7 Zinc oxide sensor (ZnO)

3.7.1 ZnO - Temperature activated resistance experiments

The experiment fulfilled with the ZnO sensor activated by heating the material (temperature-activation) concerned three target compounds: acetone, hydrogen peroxide and triacetone triperoxide (TATP). The investigation also concerned a range of temperatures from 200°C to 300°C, whereby the temperature range is narrower than the other sensor tests.

It is possible to overview the zinc oxide sensor's behaviour following the interaction with the volatiles listed above by looking at the graph in Fig. 61.

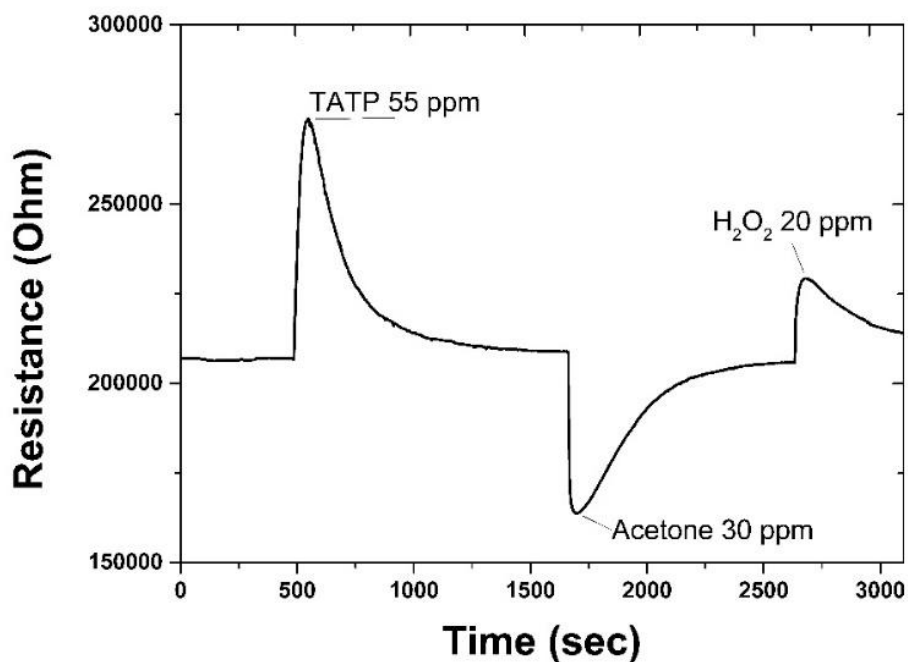


Fig. 61 Resistance signal (Ohms) of the zinc oxide sensor following injections of: TATP (55 ppm), causing an increase in resistance (positive response); acetone (29.6 ppm) which corresponded to a decrease of the resistance (negative response); hydrogen peroxide (20 ppm) which exhibited a positive response.

This experiment refers to an operating temperature of 250°C and, in essence, ZnO gave a positive response to TATP, a negative response to acetone and a positive response to hydrogen peroxide.

These trends are confirmed by the other experiments on the same target compounds at the different temperatures tested. This is desirable from a selectivity perspective: different volatiles' behaviour can theoretically distinguish among individual compounds. Fig. 62 shows the zinc oxide response when exposed to three following TATP injections (55 ppm) at an operating temperature of 250°C.

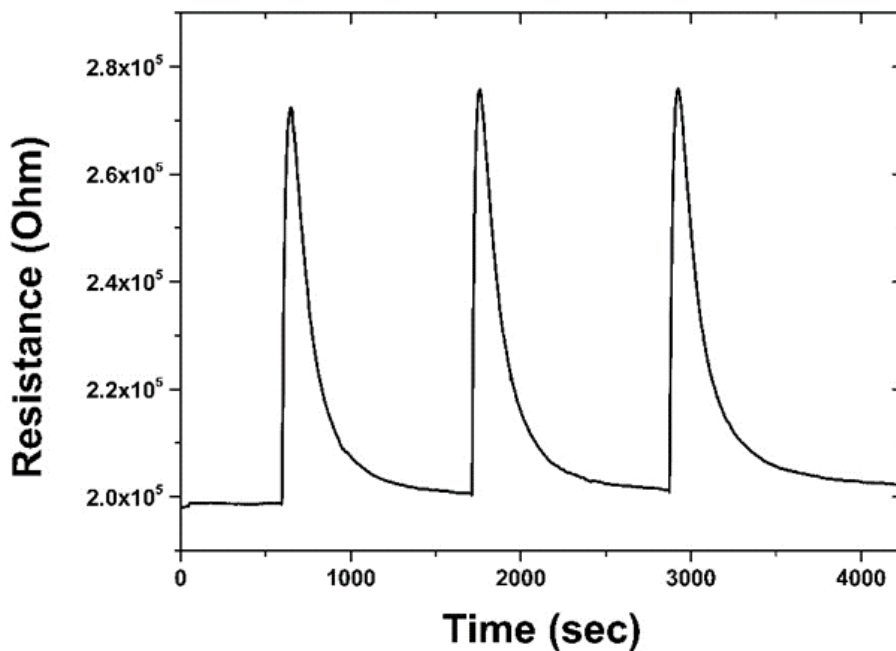


Fig. 62 Resistance response of the ZnO sensor following three injections of TATP (55 ppm) at 250°C

It is possible to observe that the sensor response decreases with decreasing concentration, as shown in Fig. 63, which reports the ZnO sensor response at different TATP concentrations. The operating temperature was again at 250°C.

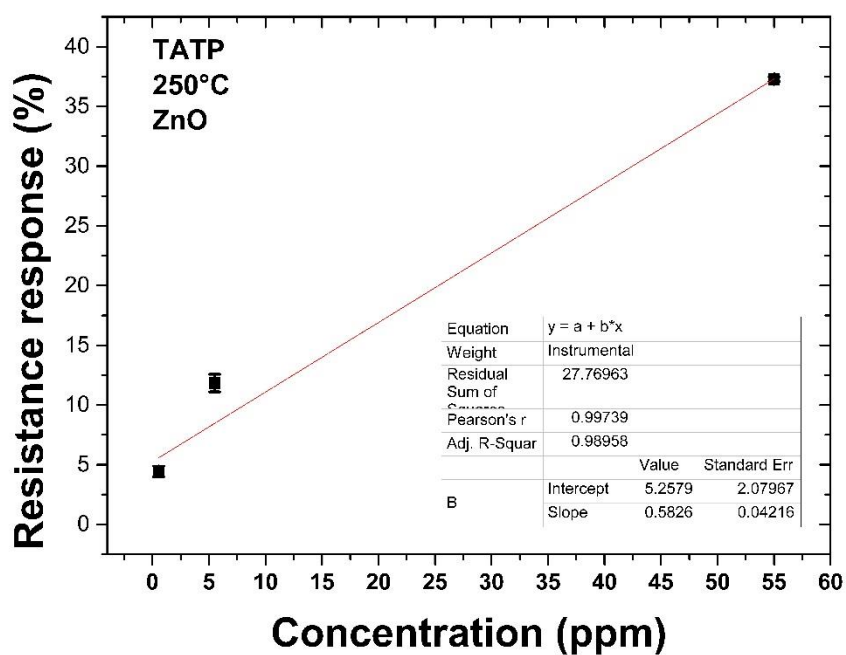


Fig. 63 Resistance response as a function of the concentration (triacetone triperoxide, sensor temperature = 250°C)

On the other hand, it is possible to observe a negative response when exposed to acetone: the electrical resistance decreases following this volatile interaction. A typical acetone (296 ppm) response in these conditions is shown in Fig. 64.

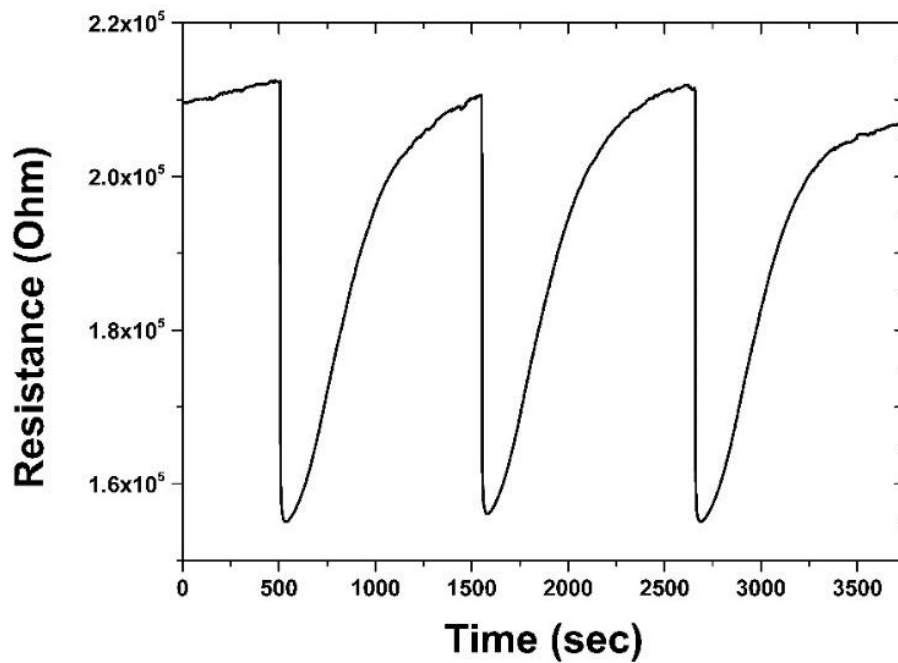


Fig. 64 ZnO response to acetone (negative signal); concentration of 296 ppm and operating temperature of 250°C

Different operating temperatures were tested, and the sensor showed an analogous behaviour at different temperatures. Similarly, to Fig 64, when exposed again to acetone but at 200°C, the sensor showed a negative response. This behaviour can be observed in Fig. 65 which shows three consecutive injections of acetone (296 ppm).

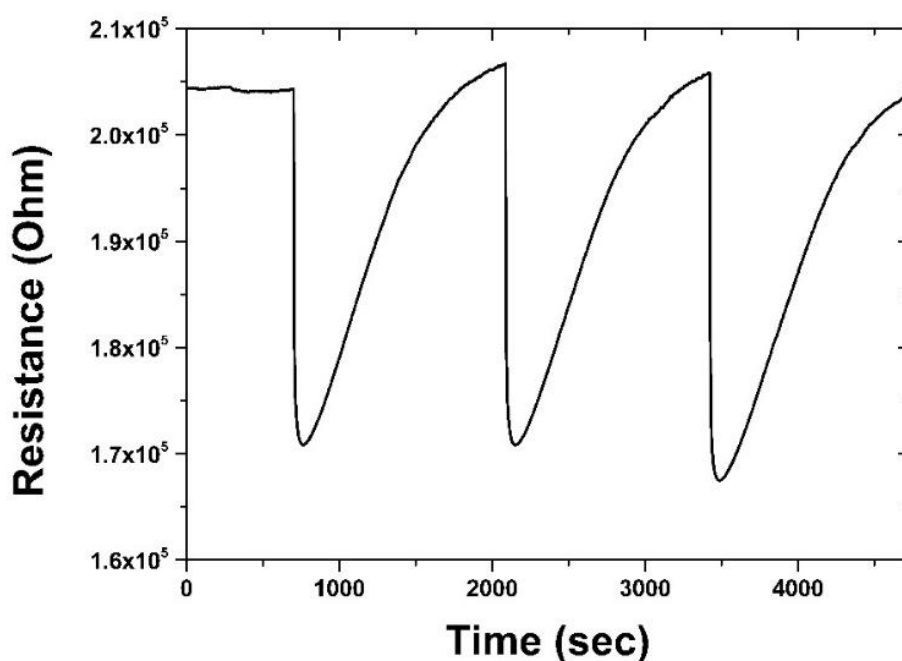


Fig. 65 ZnO response to 296 ppm of acetone at the operating temperature of 200°C

It is necessary to make some consideration also in terms of repeatability. With this in mind, the same experiment was performed after one month from the one reported in Fig 65. above (in the same conditions of activation temperature and target concentration). The result is shown in Fig. 66. The two plots do not present substantial differences in terms of magnitude of the resistance response. Nevertheless, there is a change in the baseline: from 2.05×10^5 Ohm in Fig.65 to 3.5×10^5 Ohm in Fig.66. Also, it is possible to observe a modification of the peaks shape, with the ones in Fig.66 slightly widened if compared with the peaks in Fig.65

Lower concentrations of acetone were tested to test the ZnO sensor in terms of sensitivity. Fig. 67, shows an overview of the resistance response as a function of the acetone concentration at 200°C.

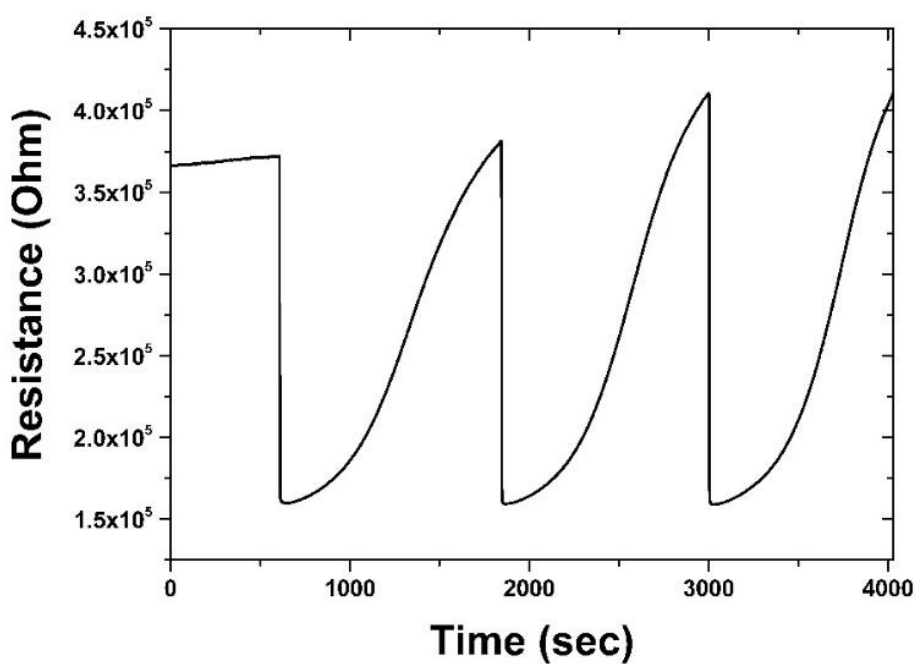


Fig. 66 ZnO responding to three following injections of acetone (296 ppm) at 200°C. The experiment was performed after one month from the one showed in Fig. 64.

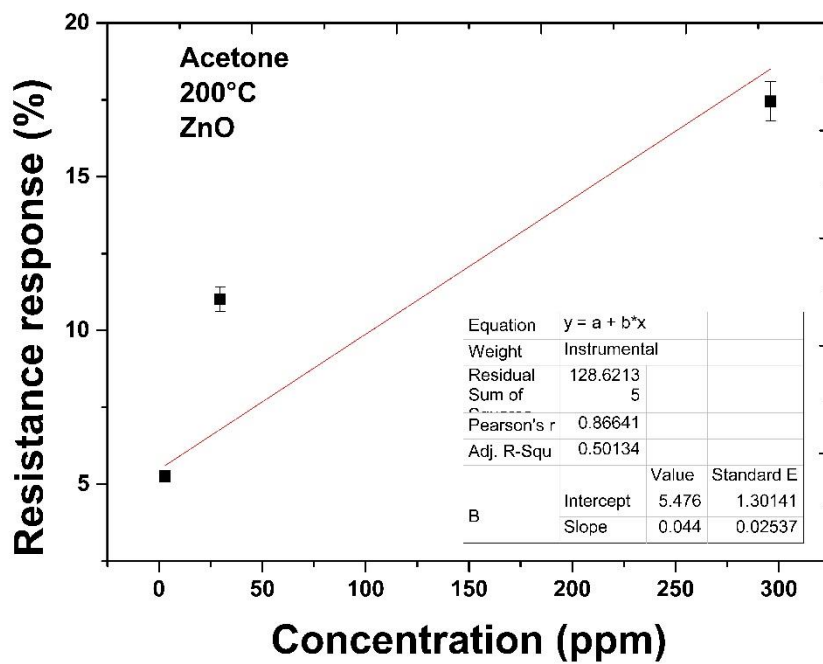


Fig. 67 Relative resistance response as a function of acetone concentration.

3.7.2 ZnO - UV-Light activated resistance experiments

The ZnO UV-activated sensor was tested with H₂O₂. In particular, the sensor sensitivity was investigated, and the response following the interaction of hydrogen peroxide is shown in Fig. 68. Different concentrations were injected, and the sensor showed a response down to levels of 2 ppb of volatile. The sensor selectivity was also tested: acetone (2960 ppm) and H₂O₂ (2 ppm) were injected, and Fig. 69 shows the sensor response. The sensor responded to hydrogen peroxide but not to acetone, even though the acetone concentration was one thousand times greater.

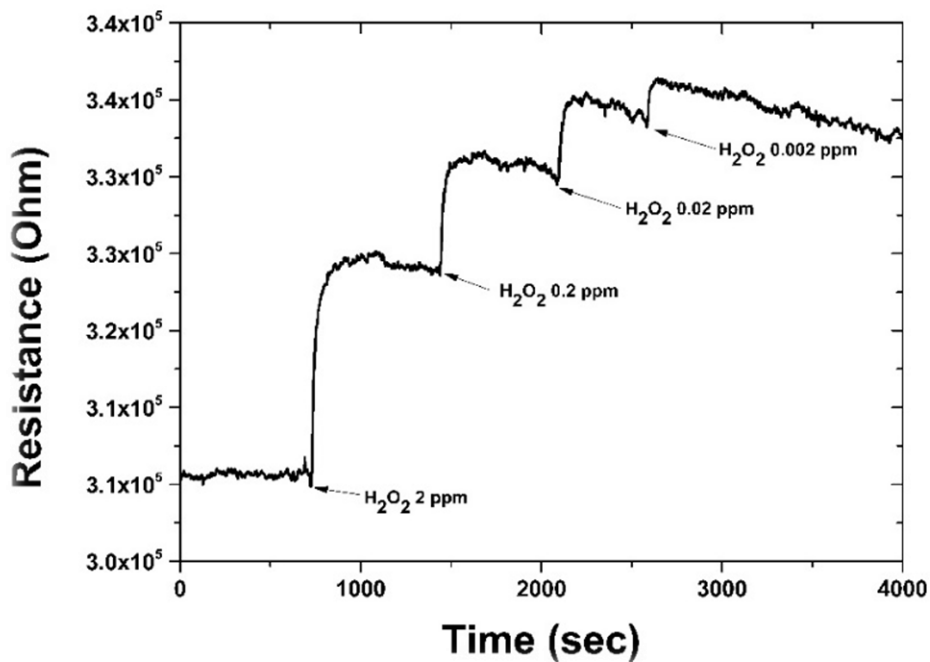


Fig. 68 Sensor sensitivity test in the case of the UV-activated ZnO sensor. The device responded to H₂O₂ in the range 2 ppb-2 ppm

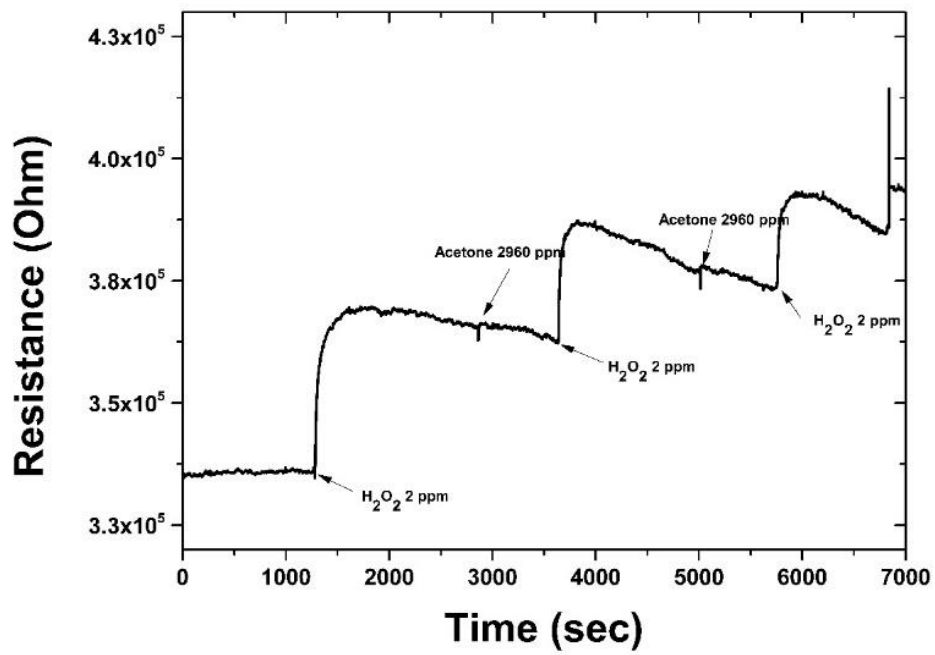


Fig. 69 Selectivity test on the UV-activated ZnO sensor. The data shows that the sensor responded selectively to hydrogen peroxide (2 ppm), and not to acetone, even at 2960 ppm

Chapter 4 – Discussion

4.1 Introduction

The hypothesis of this thesis work, underlined in the introduction, was the possibility to obtain better sensor performance, especially sensitivity and selectivity, combining more than one response from the same sensor substrate. Compared to the case when just one response mode is recorded, the dual-modality will allow detecting a lower concentration of a target compound (sensitivity) and distinguish better between more than one volatile (selectivity).

The best way to test the above hypothesis was to simultaneously record the light emission and the resistance from the same sensor during the interaction with a given volatile. As we saw in the results, different compounds were tested with three different main materials: ZrO_2 , $\text{ZrO}_2:\text{Eu}^{3+}(5\%)$, and WO_3 . We repeated the experiments for each of these materials for different activation temperatures. All this data-set allowed us to make the following considerations:

1. Which operating temperature grants (for each one of the materials tested) the higher response in terms of resistance and cataluminescence, for a given volatile compound.
2. For which material were registered the highest changes in term of resistance
3. Which material gave the higher light emission response, and in particular, if the rare earth metals doping increased the light emission production
4. In the best conditions examined above, whether it is advantageous or not to combine the resistance and the cataluminescence response

Against this background and given the experiments displayed in the *Results* part of the present research work, it is helpful to make several comparisons between the sensors investigated.

4.2. Resistance

Regarding the resistance experiments, the best temperature range varies significantly with the compound investigated, as expected. Therefore, this research work also aimed to map the sensors' response to a series of volatiles at different temperatures. For all the compounds analysed, the response profile obtained is in agreement with what is reported in previous literature [171].

1. The sensor shows a slight response for temperatures above 100°C.
2. The response increases with the temperature rise to a specific peak (T_{MAX}) value corresponding to the highest sensor sensitivity.
3. The slight decrease of the sensor response for $T > T_{MAX}$.

This aspect allowed establishing the best working conditions for each one of the materials investigated. In particular, ZrO_2 showed the best resistance response in the range 200-250°C.

As regard explosives compound, the T_{MAX} could be identified at 180°C, especially for 2,4-DNT and NG. In the range of conditions investigated, ZrO_2 did not give any change in its conductivity properties following the interaction with hydrogen peroxide and water.

The europium doping did not modify the sensing characteristic of zirconium oxide markedly in terms of resistance response intensity, with the best performances reached again in the range 200-250°C.

It is interesting to notice that the $ZrO_2:Eu^{3+}$ signal (an increase of the sensor resistance when exposed to reducing gases) was opposite to that of the undoped sensor. Zirconium oxide in the literature, is reported to have the possibility to behave as a p-type MOS [172,173]. In our case, this shift in the behaviour for the Europium-doped sensor could be explained by a structural modification. Previously, Ehrhart *et al.* reported the incorporation of large amounts of Eu^{3+} causes a modification in the ZrO_2 matrix [174]. Nevertheless, this feature requires further investigation, and it will be the subject of future work.

Tungsten oxide differed from the other sensors, showing a better response to the volatiles studied in the temperature range 275-350°C. The response of this sensor was a classical n-type behaviour

(resistance decreases following the interaction with a reducing gas), in the same way as the undoped zirconium oxide. The n-type conductivity for this material is widely reported [175–178]. We can also affirm that WO_3 showed a considerably better response in terms of resistance change than the zirconium-based sensors. This point is particularly evident by considering Fig.70, where the resistance response to different concentrations of acetone is reported for ZrO_2 (black trace), $\text{ZrO}_2:\text{Eu}^{3+}(5\%)$ (red trace) and WO_3 (blue trace). The operating temperature was 250°C , i.e. in the best working range identified.

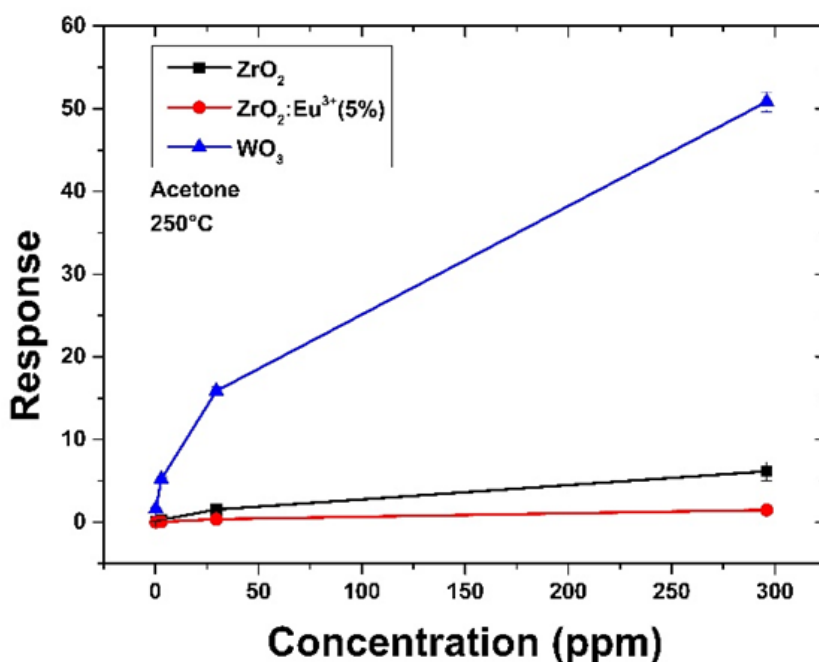


Fig. 70 Comparison between the resistance response from ZrO_2 , $\text{ZrO}_2:\text{Eu}^{3+}$ and WO_3 when exposed to different concentrations of acetone (0.296 ppm up to 296 ppm) at the operating temperature of 250°C . The graph emphasises the better performances showed by tungsten oxide if compared with the zirconium-based materials

For a given concentration of acetone, tungsten oxide gave a higher response than the zirconium-based sensors. On the other hand, the europium-doped zirconium oxide gave a lower response than the undoped one; this consideration can be underlined by considering Fig.71, reporting only the ZrO_2 and $ZrO_2:Eu^{3+}(5\%)$ response to acetone at $250^\circ C$.

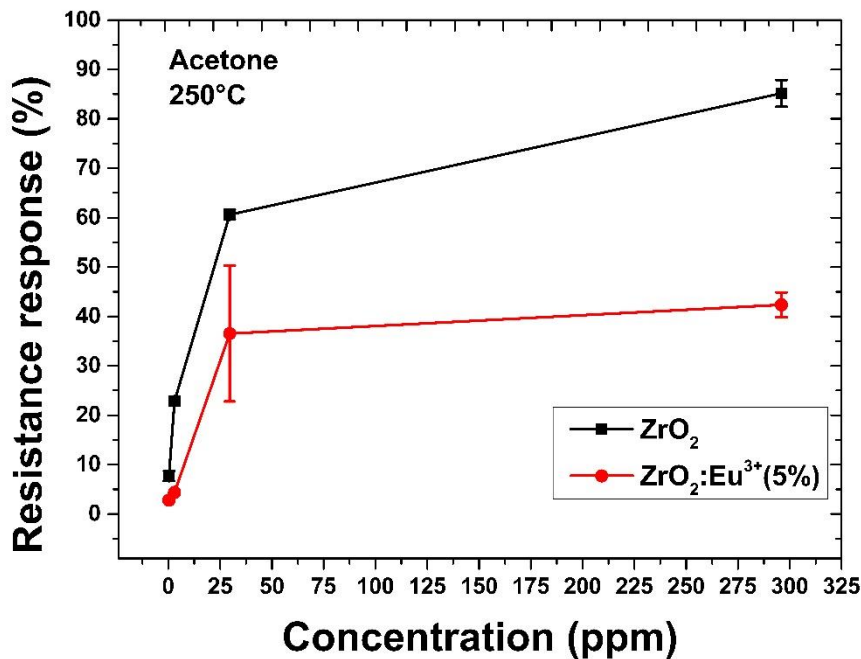


Fig. 71 Resistance response of the ZrO_2 and the $ZrO_2:Eu^{3+}$ sensor as a function of the acetone concentration at $250^\circ C$.

When considering the response to ethanol, the zirconium oxide gave the best response, as can be seen from Fig.72. The graphs reports the response at different temperatures to 58.7 ppm of ethanol by the zirconium oxide sensors (black trace in the graph), $ZrO_2:Eu^{3+}$ (reported in red), and WO_3 . The ethanol concentration investigated was 58.7 ppm

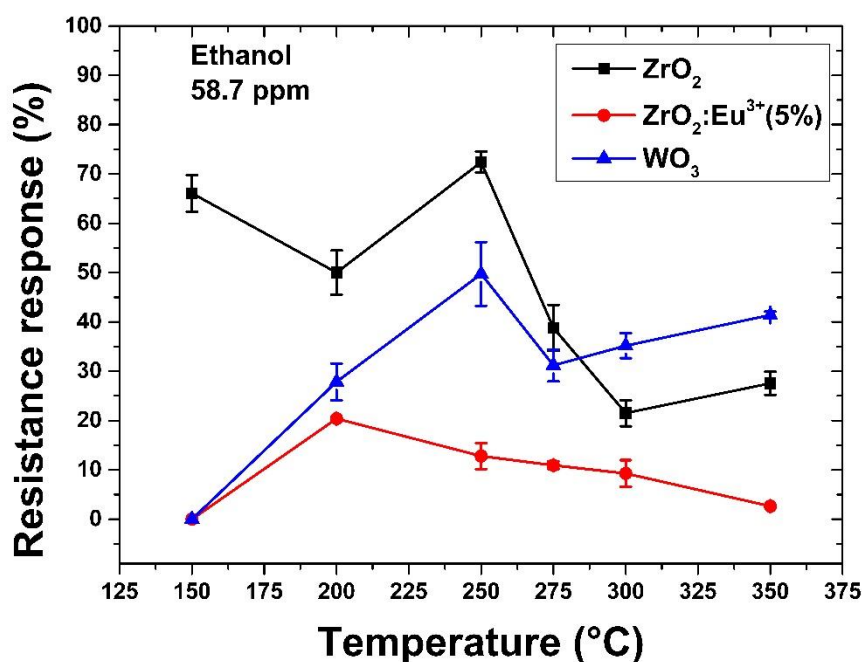


Fig. 72 Comparison of the response of ZrO₂, ZrO₂:Eu³⁺(5%) and WO₃ when exposed to ethanol (58.7 ppm) in the temperature range 150-350°C

For all the temperature values at which the sensors were tested, the ZrO₂:Eu³⁺(5%) gave the lowest response. In the range, 150-275°C, the undoped zirconium oxide performed better than tungsten oxide. There are not many studies on ZrO₂ regarding the ideal response conditions (in terms of temperature). A higher response consisting of a drop in the resistance (an increase in the number as well as mobility of charge carriers) for the range of temperatures 200-250°C has been recently reported in literature for a ZrO₂ sensor [82]. Nevertheless, other authors underlined higher operating temperatures (above 400°C) as ideal for ZrO₂ [144–146]. Also, the Tungsten oxide sensor showed a T_{max} at 250°C when exposed to ethanol. Nevertheless, for temperatures higher than 275°C the trend increased uleriorly. In literature, this material showed a better response at 300°C and 350°C. Other studies identified this as the ideal operating range for WO₃ [179–183]. A slightly higher response at 250°C could underline either the possibility to have a double value for T_{max} (not underlined in the previous literature) or a false trend.

4.3 Cataluminescence (CTL)

A comparison among the different sensors studied, analogous to the one made for the resistance, is also valuable for the CTL studies. In the first place, we observed that the light emission increased linearly with the concentration, as it is also reported in the previous literature [184]. We reported that europium doping was crucial in enhancing the light emission properties of the zirconium oxide sensor. This aspect can be observed in Fig.73, reporting the CTL from ZrO_2 (black trace), $\text{ZrO}_2:\text{Eu}^{3+}$ (5%) (red trace) and WO_3 (blue trace) as a function of the acetone concentration. The operating temperature was 275°C .

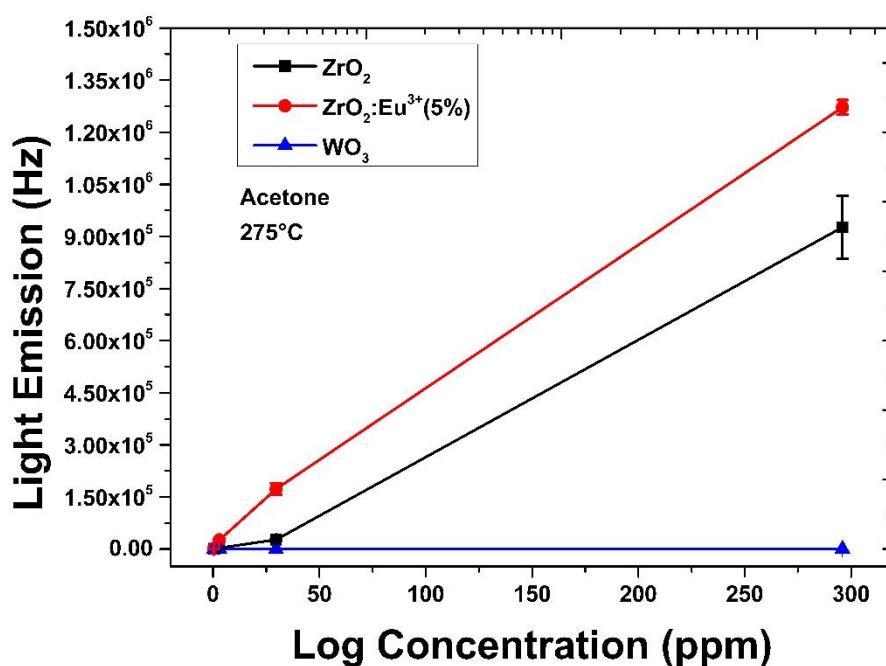


Fig. 73 CTL response of the three sensors of ZrO_2 , $\text{ZrO}_2:\text{Eu}^{3+}$ (5%) and WO_3 following the interaction with different concentrations of acetone (substrate temperature= 275°C)

At the temperature investigated, the tungsten oxide gave a far lower response. To our knowledge there are not comprehensive studies at the present moment on the CTL properties of pure WO_3 . Different nanostructures, such as Nano dots are employed for ultrasensitive electrochemiluminescence (ECL) sensing[185]. It is interesting to focus only on the zirconium-based materials and to report the light emission on a logarithmic scale as well as the acetone concentration. This way (Fig. 74), it is possible to underline better how the doping with Eu^{3+} (red trace) increased the light emission compared to the ZrO_2 case (black trace).

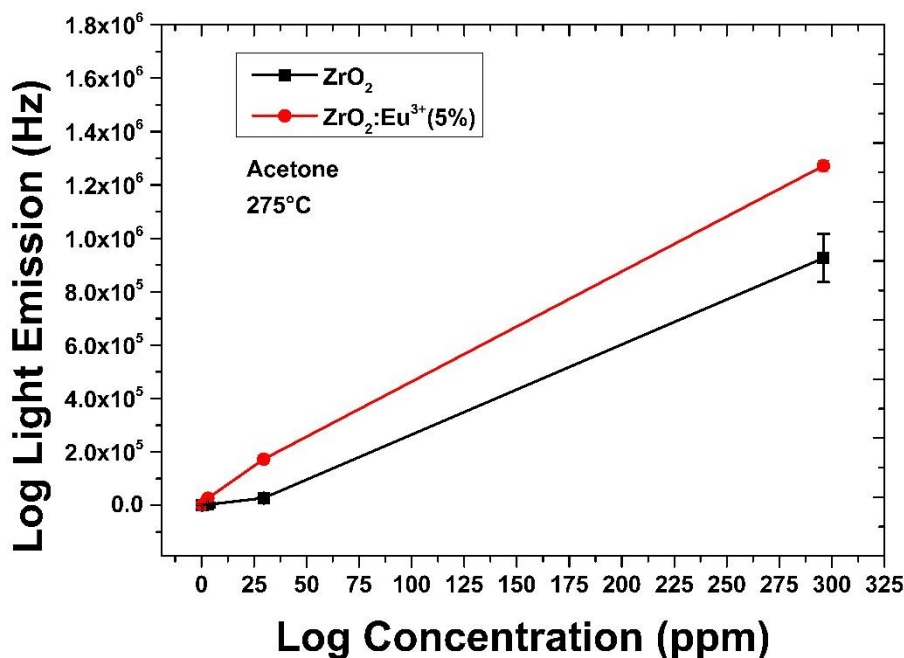


Fig. 74 Log of the CTL produced by the zirconium-based sensors when exposed to acetone (concentration on a Log scale, sensor temperature of 275°C)

These results are in line with what has been previously reported regarding the MOS doping with rare earth metals, which were found to enhance the light emission response when compared with the pure material [108,145,186,187].

In addition, we can notice that at the lowest concentration (0.296 ppm), the response from the two sensors is approximately zero. This may be related to the fact that the sensors reached the detection

limit. Regarding CTL sensors, other authors reported a detection limit slightly higher: Shi *et al.* reported a limit of 4 ppm [188], while the value reported by Tang *et al.* was of 0.7 ppm [189]. In the range of 3-30 ppm, the gap is more pronounced. Moreover, the signal appears to be similar at 296 ppm, representing probably a value close to the saturation for the sensor. This point can be justified by the depletion of adsorption sites on the material surface. Zhang *et al.* reported a saturation value of 550 ppm, for ethanol detection by a $\text{ZrO}_2:\text{Eu}^{3+}(5\%)$ sensor, slightly higher than the one herein reported.

A common aspect that can be underlined for the three materials studied in terms of light emission is that with the temperature increase, the CTL signal reaches a peak (identifiable in the range 200-275°C) and then decreases quantitatively. This diminution in the light emission emitted from the material corresponds to the well-known increase of black body radiation (BBR). The competing process of heat dissipation released as black body radiation was also underlined by Borgschulte *et al.* [190], and may represent a problem, considering that the europium doping, even if it increased the material's CTL production, shifted the best sensor performance to higher temperatures. Therefore, selective wavelength filtering can represent a possible solution.

4.4. Dual-modality

The experiments carried out during this research project showed the possibility to increase the selectivity of detection through multi-modal sensing. This point was the central hypothesis of the present thesis work. First it should be noted that for each material tested we obtained a multimodal response i.e. each sensor gave a concurrent cataluminescence and resistance response. This was true when exposed to an appropriate concentration of a target volatile at a specific operating temperature. However, it should be noted that the absence of a cataluminescent response could also be used in a minimal sensor array to differentiate VOC type or concentration. It should also be noted that where

materials have opposite p-type and n-type resistance-based responses but the same cataluminiscent based responses this could be utilised to enhance selectivity.

One of the main advantages of the dual modality sensor is the possibility to identify a single target volatile through two different sensor parameters measured in parallel. It is, in fact, possible to calculate a ratio between the light emission and the resistance (*Equation 8*). This ratio will be well-defined for a given compound at a certain temperature. For example, let us take the europium-doped zirconium oxide, which showed the best light emission characteristics. Fig. 75 reports the ratio between the light emission and the resistance response at different temperatures.

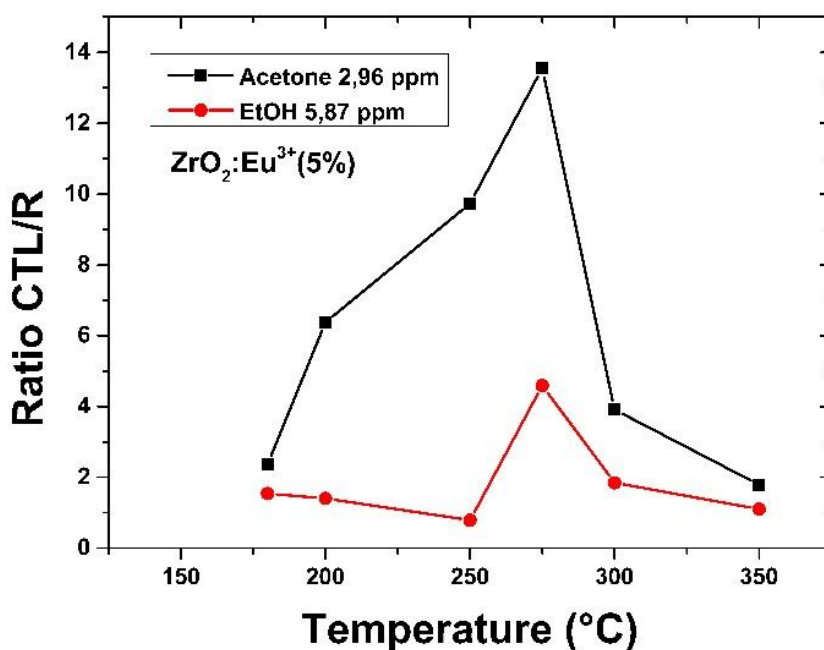


Fig. 75 Dual-modality response (ratio light emission/resistance) of the $ZrO_2:Eu^{3+}(5\%)$ sensor respectively to acetone (29.6 ppm) and ethanol (58.7 ppm)

The graph refers to comparable concentrations of acetone (2.96 ppm) and ethanol (5.87 ppm). Thus, we can underline the massive difference in the CTL/resistance ratio. On a practical level, this feature could guarantee a lower possibility to have a false positive in the presence of both acetone (i.e. the target) and ethanol (the interferant). This graph also makes it possible to establish at which operating

temperature the ratio is maximised. Consequently, it is more convenient to set the sensor at that specific value to ensure the best performance. In this case, the best range was 250-300°C.

In fact, at 275°C, both acetone (2.96 ppm) and ethanol (5.87 ppm) gave a similar resistance response, as shown in Fig. 76. Combining the resistance signal with the cataluminescence one, allows then to detect selectively acetone, in the case it is the target compound (as it is possible to see in Fig. 75).

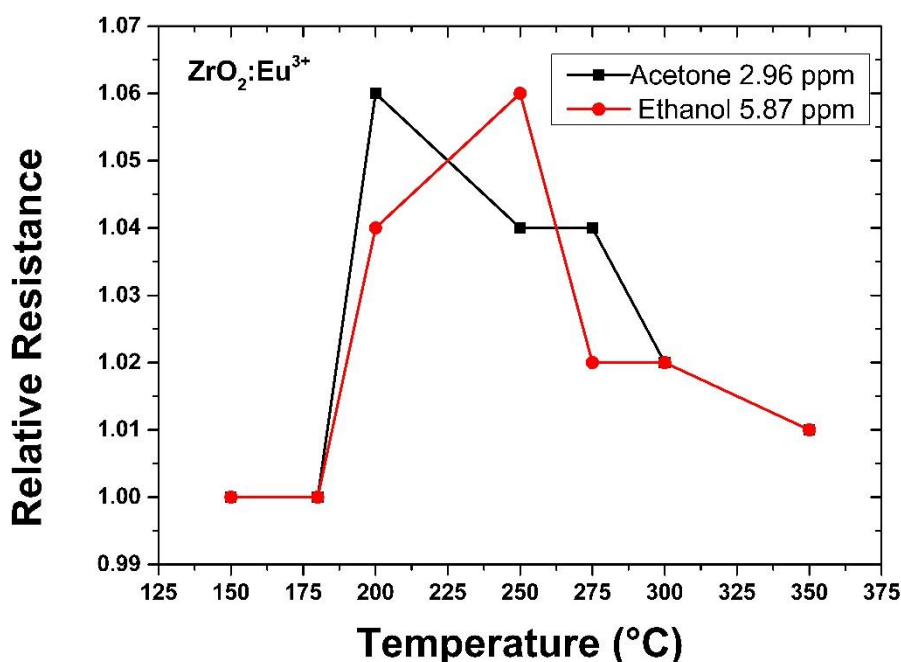


Fig. 76 Comparison between the relative resistance response for acetone (2.96 ppm, black trace) and ethanol (5.87 ppm, red trace). At each one of the temperatures reported, the resistance signal of the two compounds is relatively similar.

Another possibility is to have two or more sensors operating at different temperatures and use the response ratios to calculate the concentration of a binary mixture of volatiles. Having multimodal sensors may allow the design of a minimal sensor array with fewer sensors than conventional heated metal oxide sensors or cataluminescent sensors alone.

Another promising outcome from the results is applying dual-modality sensing for explosive detection, for example, ZrO_2 in the operating temperature range 150-250°C. Fig. 77 summarises the

resistance response % (a), the cataluminescence (b), and the ratio CTL/resistance response % (c) of the zirconium oxide when exposed to 2,4-dinitrotoluene (0.54 ppm), DMNB (2.76 ppm), EGDN (0.63 ppm), and Nitroglycerine (0.63 ppm). The temperature was set at 180°C. As regards the resistance response (77.a), DMNB and 2,4-DNT gave a relatively similar response (-20% and -30%, respectively). A better distinction between DMNB and 2,4-DNT could consequently be obtained, considering their light emission response (77.b) and calculating a ratio (77.c). Their ratio is, in fact, -107 for DMNB and -12 for 2,4-DNT.

Analogously, the ZrO₂ sensor gave a comparable light emission response following the interaction with 2,4 DNT (367 Hz) and nitroglycerine (511 Hz). Taking into consideration the resistance response for 2,4 DNT (-30%) and nitroglycerine (23%) can improve the selectivity between these molecules. In this case, in fact, the two compounds also gave a resistance response of different signs, allowing us to calculate a ratio CTL/resistance of -12 for the 2,4-DNT and 21 for the nitroglycerine.

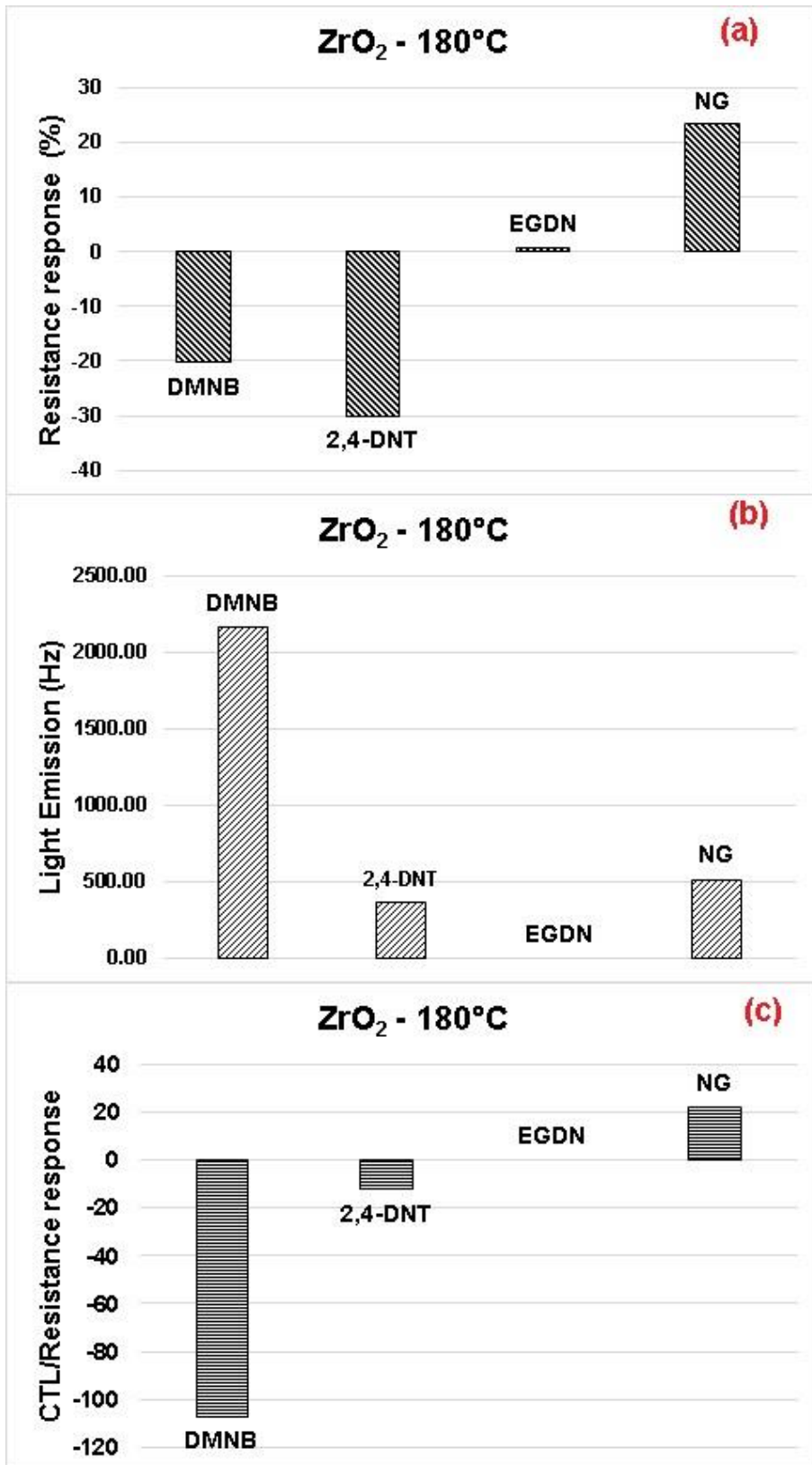


Fig. 77 Resistance response % (a), cataluminescence (b) and ratio CTL/resistance (c) for the ZrO₂ sensor (180°C operating temperature) when exposed to four different explosive compounds: 2,3-dimethyl-2,3-dinitrobutane, 2,4-dinitrotoluene, ethylene glycol dinitrate, and nitroglycerine.

Chapter 5 - Conclusion

The thesis behind this research work was to combine resistance and cataluminescence measurements simultaneously on a single heated metal oxide sensor. Effectively, the cataluminescence and resistance measurements can be combined to enhance the sensors' selectivity to various targets compared to the single-mode sensors. The roadmap to test this proposition was to screen the resistance and the light emission response of several sensing materials: ZrO_2 , $\text{ZrO}_2:\text{Eu}^{3+}$, WO_3 and ZnO . These experiments and the following data processing showed that it is possible to create a sensor system with increased selectivity using dual-modality. Thus, it is possible to distinguish between different targets that, even if they gave a similar response under one of the sensing modalities, could provide a different response to the other sensing modality. It is possible to exploit dual modality for enhanced sensitivity to a target's presence as one of the modalities could be optimised for sensitivity to that target. In particular, the europium-doped zirconia sensor has shown a better response in terms of CTL even at a relatively low operating temperature, whilst the resistance response is similar to that of the undoped zirconia. The WO_3 sensor exhibited the best resistance response even with low concentrations of the target compounds but gave limited light emission, which was only detected at high target concentrations. Therefore, it may be considered unsuitable as a multimodal sensor. This thesis work represents the first study on the electrical resistance combined with the cataluminescence signal. Part of the results have been recently published as a peer-reviewed journal paper [159], while the concepts and ideas were previously patented [158].

Chapter 6 Future Work

The outcomes from this thesis project were promising from the viewpoint of exploiting dual-modality sensing to detect volatile compounds. Nevertheless, this work can be considered the first step, and further steps can be undertaken and are detailed below. Firstly, there are a series of materials that have been synthesised but are yet to be fully characterised and tested: $\text{ZrO}_2:\text{Y}^{3+}$, $\text{ZrO}_2:\text{Tb}^{3+}$ and $\text{ZrO}_2:\text{Er}^{3+}$. In fact, an exciting perspective is the possible light emission characteristics of these materials, given the presence of a rare earth metal and, consequently, the possibility to have the production of enhanced cataluminescence in addition to electrical resistance changes. The aim is to produce sensors that have different levels of resistance and cataluminescent response and selectivity to certain specific target molecules. In addition, it is possible to synthesise new analogue materials which have shown the potential to produce luminescence and be employed in sensing applications. An example is $\text{TiO}_2:\text{Sm}^{3+}$ [146]. Additionally, the zinc oxide sensor in this work was not characterised in terms of cataluminescence response, but all materials tested so far have given some cataluminescent response e.g. tungsten oxide.

Secondly, further experiments have to be conducted on the materials presented in this thesis. The experiments were undertaken in laboratory air to mimic real life conditions for detecting explosives in the field. Consequently, a general improvement in response and stability could be achieved by repeating the screening herein presented using a compressed dry synthetic air cylinder. The sensor response could be characterised at a range of controlled humidities to ascertain the sensor performance under a range of environmental conditions.

In addition, better vapour generation and to run tests with certified gas standards and a mass flow controller are other possible steps in the achievement of better repeatability of the results. Further experiments to test the volatile concentration via SIFT-MS for those molecules that are unlikely to have gas standards are also required.

As regards the cataluminescence experiment, the results underlined that at higher temperatures, the sensor sensitivity is limited by increased black body radiation (BBR). An enhanced BBR filtering could make it possible to register cataluminescence at higher temperatures.

An area left unexplored throughout this MPhil is the possibility of combining sensors into arrays. This option is promising since different sensors can give different responses to a given volatile compound. In addition, each one of the sensors in the array can be set at a different temperature. What can be produced this way is a fingerprint of the compound, increasing the selectivity of the sensing system considerably.

Finally, another fascinating horizon is the employment of dual-modality sensor devices in real-life applications. This aspect can be achieved by projecting and building prototypes for detecting volatiles in the field. Furthermore, the interfacing of the sensor systems with separative methods (i.e. GC columns) paves the way to several applications in areas like disease-related compounds detection (i.e. volatiles from human breath) or explosive detection in public places. A dual-modality sensor can be advantageous in combination with a GC equipment. In fact, the multimodal sensor is usually employed to detect low molecular weight molecules not detectable with the gas chromatographer itself. The fast response and recovery kinetics of the cataluminescent sensors may lend themselves to being interfaced with a GC where other sensors with slower recovery kinetics are not able to resolve all the peaks.

References

- [1] C.K. Ho, A. Robinson, D.R. Miller, M.J. Davis, Overview of Sensors and Needs for Environmental Monitoring, *Sensors*. 5 (2005) 4–37.
- [2] A. Mirzaei, S.G. Leonardi, G. Neri, Detection of hazardous volatile organic compounds (VOCs) by metal oxide nanostructures-based gas sensors: A review, *Ceramics International*. (2016). <https://doi.org/10.1016/j.ceramint.2016.06.145>.
- [3] K.M. Tripathi, T.Y. Kim, D. Losic, T.T. Tung, Recent advances in engineered graphene and composites for detection of volatile organic compounds (VOCs) and non-invasive diseases diagnosis, *Carbon N Y*. 110 (2016) 97–129. <https://doi.org/10.1016/j.carbon.2016.08.040>.
- [4] N. Drabińska, C. Flynn, N. Ratcliffe, I. Belluomo, A. Myridakis, O. Gould, M. Fois, A. Smart, T. Devine, B.D.L. Costello, A literature survey of all volatiles from healthy human breath and bodily fluids: The human volatilome, *Journal of Breath Research*. 15 (2021). <https://doi.org/10.1088/1752-7163/abf1d0>.
- [5] A. Ulanowska, T. Kowalkowski, E. Trawińska, B. Buszewski, The application of statistical methods using VOCs to identify patients with lung cancer, *Journal of Breath Research*. 5 (2011) 046008. <https://doi.org/10.1088/1752-7155/5/4/046008>.
- [6] S. Giannoukos, B. Brkić, Brkić, S. Taylor, A. Marshall, G.F. Verbeck, Chemical Sniffing Instrumentation for Security Applications, (2016). <https://doi.org/10.1021/acs.chemrev.6b00065>.
- [7] S. Giannoukos, A. Agapiou, S. Taylor, Advances in chemical sensing technologies for VOCs in breath for security/threat assessment, illicit drug detection, and human trafficking activity, *Journal of Breath Research*. 12 (2018). <https://doi.org/10.1088/1752-7163/aa95dd>.
- [8] G. Gregis, J.B. Sanchez, I. Bezverkhyy, W. Guy, F. Berger, V. Fierro, J.P. Bellat, A. Celzard, Detection and quantification of lung cancer biomarkers by a micro-analytical device using a single metal oxide-based gas sensor, *Sensors and Actuators, B: Chemical*. 255 (2018) 391–400. <https://doi.org/10.1016/j.snb.2017.08.056>.
- [9] T. Bruderer, T. Gaisl, M.T. Gaugg, N. Nowak, B. Streckenbach, S. Mü, A. Moeller, M. Kohler, R. Zenobi, On-Line Analysis of Exhaled Breath Focus Review, (2019). <https://doi.org/10.1021/acs.chemrev.9b00005>.
- [10] A.T. Güntner, S. Abegg, K. Königstein, P.A. Gerber, A. Schmidt-Trucksäss, S.E. Pratsinis, Breath sensors for health monitoring, *ACS Sensors*. 4 (2019) 268–280. <https://doi.org/10.1021/acssensors.8b00937>.
- [11] A.A. Vasiliev, A.E. Varfolomeev, I.A. Volkov, N.P. Simonenko, P. V Arsenov, I.S. Vlasov, V. V Ivanov, A. V Pislyakov, A.S. Lagutin, I.E. Jahatspanian, T. Maeder, Reducing Humidity Response of Gas Sensors for Medical Applications: Use of Spark Discharge Synthesis of Metal Oxide Nanoparticles, (2018). <https://doi.org/10.3390/s18082600>.
- [12] D. Gutmacher, U. Hofer, J. Wöllenstein, Gas sensor technologies for fire detection, *Sensors and Actuators B*. 175 (2012) 40–45. <https://doi.org/10.1016/j.snb.2011.11.053>.
- [13] K. Ihokura, J. Watson, The stannic oxide gas sensor: Principles and applications, CRC Press, 2017. <https://doi.org/10.1201/9780203735893>.
- [14] K. Bunpang, A. Wisitsoraat, A. Tuantranont, S. Singkammo, S. Phanichphant, C. Liewhiran, Highly selective and sensitive CH₄ gas sensors based on flame-spray-made Cr-doped SnO₂ particulate films, (2019). <https://doi.org/10.1016/j.snb.2019.04.049>.

- [15] L. Li, Z. Wang, T. Wang, J. Gong, Highly sensitive non-enzymatic MP sensor based on electrospun copper oxide-doped zirconium oxide composite microfibers, (2019). <https://doi.org/10.1016/j.jelechem.2019.05.053>.
- [16] S.R. Gawali, V.L. Patil, V.G. Deonikar, S.S. Patil, D.R. Patil, P.S. Patil, J. Pant, Ce doped NiO nanoparticles as selective NO₂ gas sensor, (2017). <https://doi.org/10.1016/j.jpccs.2017.11.005>.
- [17] A. Ponzoni, C. Baratto, N. Cattabiani, M. Falasconi, V. Galstyan, E. Nunez-Carmona, F. Rigoni, V. Sberveglieri, G. Zambotti, D. Zappa, Metal Oxide Gas Sensors, a Survey of Selectivity Issues Addressed at the SENSOR Lab, Brescia (Italy), (2017). <https://doi.org/10.3390/s17040714>.
- [18] M. Tonezzer, S.C. Izidoro, J.P.A. Moraes, L. Dang, Improved Gas Selectivity Based on Carbon Modified SnO₂ Nanowires, *Nanowires*. *Front. Mater.* 6 (2019) 277. <https://doi.org/10.3389/fmats.2019.00277>.
- [19] B.P.J. de Lacy Costello, R.J. Ewen, N.M. Ratcliffe, M. Richards, Highly sensitive room temperature sensors based on the UV-LED activation of zinc oxide nanoparticles, *Sensors and Actuators, B: Chemical*. (2008). <https://doi.org/10.1016/j.snb.2008.06.055>.
- [20] M.S. Kamal, S.A. Razzak, M.M. Hossain, Catalytic oxidation of volatile organic compounds (VOCs) - A review, *Atmospheric Environment*. (2016). <https://doi.org/10.1016/j.atmosenv.2016.05.031>.
- [21] R. Koppmann, *Volatile Organic Compounds in the Atmosphere*, 2007. <https://doi.org/10.1002/9780470988657>.
- [22] M.W. Holdgate, *A (biological)perspective of environmental pollution., A (Biological)Perspective of Environmental Pollution*. (1979).
- [23] J. Colls, Gaseous air pollutants, in: *Air Pollution*, 2010. https://doi.org/10.4324/9780203476024_chapter_1.
- [24] R. Pal, K.H. Kim, Y.J. Hong, E.C. Jeon, The pollution status of atmospheric carbonyls in a highly industrialized area, *Journal of Hazardous Materials*. (2008). <https://doi.org/10.1016/j.jhazmat.2007.09.068>.
- [25] D.A. Sarigiannis, S.P. Karakitsios, A. Gotti, I.L. Liakos, A. Katsoyiannis, Exposure to major volatile organic compounds and carbonyls in European indoor environments and associated health risk, *Environment International*. (2011). <https://doi.org/10.1016/j.envint.2011.01.005>.
- [26] U. Schlink, M. Rehwagen, M. Damm, M. Richter, M. Borte, O. Herbarth, Seasonal cycle of indoor-VOCs: comparison of apartments and cities, *Atmospheric Environment*. 38 (2004) 1181–1190. <https://doi.org/https://doi.org/10.1016/j.atmosenv.2003.11.003>.
- [27] J.E. Colman Lerner, M. de los A. Gutierrez, D. Mellado, D. Giuliani, L. Massolo, E.Y. Sanchez, A. Porta, Characterization and cancer risk assessment of VOCs in home and school environments in gran La Plata, Argentina, *Environmental Science and Pollution Research*. (2018). <https://doi.org/10.1007/s11356-018-1265-2>.
- [28] T. Salthammer, S. Mentese, R. Marutzky, Formaldehyde in the indoor environment, *Chemical Reviews*. (2010). <https://doi.org/10.1021/cr800399g>.
- [29] A.J. Venn, M. Cooper, M. Antoniak, C. Laughlin, J. Britton, S.A. Lewis, Effects of volatile organic compounds, damp, and other environmental exposures in the home on wheezing illness in children, *Thorax*. (2003). <https://doi.org/10.1136/thorax.58.11.955>.
- [30] M.E. Andersen, H.J. Clewell, E. Bermudez, G.A. Willson, R.S. Thomas, Genomic signatures and dose-dependent transitions in nasal epithelial responses to inhaled formaldehyde in the rat, *Toxicological Sciences*. (2008). <https://doi.org/10.1093/toxsci/kfn097>.

- [31] J.M. Daisey, A.T. Hodgson, W.J. Fisk, M.J. Mendell, J. Ten Brinke, Volatile organic compounds in twelve California office buildings: Classes, concentrations and sources, *Atmospheric Environment*. (1994). [https://doi.org/10.1016/1352-2310\(94\)00200-5](https://doi.org/10.1016/1352-2310(94)00200-5).
- [32] A.C. Heeley-Hill, S.K. Grange, M.W. Ward, A.C. Lewis, N. Owen, C. Jordan, G. Hodgson, G. Adamson, Frequency of use of household products containing VOCs and indoor atmospheric concentrations in homes, *Environmental Science: Processes & Impacts*. 23 (2021) 699–713. <https://doi.org/10.1039/D0EM00504E>.
- [33] A. Báez, H. Padilla, R. García, M.D.C. Torres, I. Rosas, R. Belmont, Carbonyl levels in indoor and outdoor air in Mexico City and Xalapa, Mexico, *Science of the Total Environment*. (2003). [https://doi.org/10.1016/S0048-9697\(02\)00344-3](https://doi.org/10.1016/S0048-9697(02)00344-3).
- [34] B. De Lacy Costello, A. Amann, H. Al-Kateb, C. Flynn, W. Filipiak, T. Khalid, D. Osborne, N.M. Ratcliffe, A review of the volatiles from the healthy human body, *Journal of Breath Research*. (2014). <https://doi.org/10.1088/1752-7155/8/1/014001>.
- [35] M. Righettoni, A. Tricoli, S. Gass, A. Schmid, A. Amann, S.E. Pratsinis, Breath acetone monitoring by portable Si:WO₃ gas sensors, *Analytica Chimica Acta*. (2012). <https://doi.org/10.1016/j.aca.2012.06.002>.
- [36] V. Saasa, T. Malwela, M. Beukes, M. Mokgotho, C.-P. Liu, B. Mwakikunga, Sensing Technologies for Detection of Acetone in Human Breath for Diabetes Diagnosis and Monitoring, *Diagnostics*. (2018). <https://doi.org/10.3390/diagnostics8010012>.
- [37] R. Kalidoss, S. Umaphathy, R. Anandan, V. Ganesh, Y. Sivalingam, Comparative Study on the Preparation and Gas Sensing Properties of Reduced Graphene Oxide/SnO₂ Binary Nanocomposite for Detection of Acetone in Exhaled Breath, *Analytical Chemistry*. (2019). <https://doi.org/10.1021/acs.analchem.8b05670>.
- [38] M. Masikini, M. Chowdhury, O. Nemraoui, Review—Metal Oxides: Application in Exhaled Breath Acetone Chemiresistive Sensors, *Journal of The Electrochemical Society*. (2020). <https://doi.org/10.1149/1945-7111/ab64bc>.
- [39] D. Wang, F. Zhang, A. Prabhakar, X. Qin, E.S. Forzani, N. Tao, Colorimetric Sensor for Online Accurate Detection of Breath Acetone, *ACS Sensors*. (2020). <https://doi.org/10.1021/acssensors.0c02025>.
- [40] R.L. Siegel, K.D. Miller, A. Jemal, *Cancer statistics, 2018*, CA: A Cancer Journal for Clinicians. (2018). <https://doi.org/10.3322/caac.21442>.
- [41] V.A. Moyer, Screening for prostate cancer: U.S. preventive services task force recommendation statement, *Annals of Internal Medicine*. (2012). <https://doi.org/10.7326/0003-4819-157-2-201207170-00459>.
- [42] Q. Gao, X. Su, M.H. Annabi, B.R. Schreiter, T. Prince, A. Ackerman, S. Morgas, V. Mata, H. Williams, W.Y. Lee, Application of Urinary Volatile Organic Compounds (VOCs) for the Diagnosis of Prostate Cancer, *Clinical Genitourinary Cancer*. (2019). <https://doi.org/10.1016/j.clgc.2019.02.003>.
- [43] S. Sethi, R. Nanda, T. Chakraborty, Clinical application of volatile organic compound analysis for detecting infectious diseases, *Clinical Microbiology Reviews*. 26 (2013) 462–475. <https://doi.org/10.1128/CMR.00020-13>.
- [44] J. Dummer, M. Storer, M. Swanney, M. McEwan, A. Scott-Thomas, S. Bhandari, S. Chambers, R. Dweik, M. Epton, Analysis of biogenic volatile organic compounds in human health and disease, *TrAC - Trends in Analytical Chemistry*. 30 (2011) 960–967. <https://doi.org/10.1016/j.trac.2011.03.011>.

- [45] W.M. Ahmed, O. Lawal, T.M. Nijsen, R. Goodacre, S.J. Fowler, Exhaled Volatile Organic Compounds of Infection: A Systematic Review, *ACS Infectious Diseases*. 3 (2017) 695–710. <https://doi.org/10.1021/acsinfecdis.7b00088>.
- [46] D.G. Burke, B. Halpern, D. Malegan, E. McCairns, D. Danks, P. Schlesinger, B. Wilken, Profiles of urinary volatiles from metabolic disorders characterized by unusual odors., *Clinical Chemistry*. 29 (1983) 1834–1838. <https://doi.org/10.1093/clinchem/29.10.1834>.
- [47] Y. Rosenblatt, P. Phan, P. Desandre, L. Lobon, C. Hsu, Diagnostic odor recognition, *Acad Emerg Med*. 7 (2000) 1168—1169.
- [48] S. Esfahani, A. Wicaksono, E. Mozdiak, R.P. Arasaradnam, J.A. Covington, Non-invasive diagnosis of diabetes by volatile organic compounds in urine using FAIMs and FOX4000 electronic nose, *Biosensors (Basel)*. 8 (2018). <https://doi.org/10.3390/bios8040121>.
- [49] T. Wang, S. Zhang, Q. Yu, S. Wang, P. Sun, H. Lu, F. Liu, X. Yan, G. Lu, Novel Self-Assembly Route Assisted Ultra-Fast Trace Volatile Organic Compounds Gas Sensing Based on Three-Dimensional Opal Microspheres Composites for Diabetes Diagnosis, *ACS Applied Materials & Interfaces*. 10 (2018) 32913–32921. <https://doi.org/10.1021/acsami.8b13010>.
- [50] I.A. Ratiu, T. Ligor, V. Bocos-Bintintan, C.A. Mayhew, B. Buszewski, Volatile Organic Compounds in Exhaled Breath as Fingerprints of Lung Cancer, Asthma and COPD, *Journal of Clinical Medicine*. 10 (2021). <https://doi.org/10.3390/jcm10010032>.
- [51] M. Koureas, P. Kirgou, G. Amoutzias, C. Hadjichristodoulou, K. Gourgoulianis, A. Tsakalof, Target Analysis of Volatile Organic Compounds in Exhaled Breath for Lung Cancer Discrimination from Other Pulmonary Diseases and Healthy Persons, *Metabolites*. 10 (2020). <https://doi.org/10.3390/metabo10080317>.
- [52] E. Janssens, J.P. van Meerbeeck, K. Lamote, Volatile organic compounds in human matrices as lung cancer biomarkers: a systematic review, *Critical Reviews in Oncology/Hematology*. 153 (2020) 103037. <https://doi.org/10.1016/j.critrevonc.2020.103037>.
- [53] X. Chen, K.G. Muhammad, C. Madeeha, W. Fu, L. Xu, Y. Hu, J. Liu, K. Ying, L. Chen, G.O. Yurievna, Calculated indices of volatile organic compounds (VOCs) in exhalation for lung cancer screening and early detection, *Lung Cancer*. 154 (2021) 197–205. <https://doi.org/10.1016/j.lungcan.2021.02.006>.
- [54] K.E. van Keulen, M.E. Jansen, R.W.M. Schrauwen, J.J. Kolkman, P.D. Siersema, Volatile organic compounds in breath can serve as a non-invasive diagnostic biomarker for the detection of advanced adenomas and colorectal cancer, *Alimentary Pharmacology & Therapeutics*. 51 (2020) 334–346. <https://doi.org/10.1111/apt.15622>.
- [55] W. Zhou, J. Tao, J. Li, S. Tao, Volatile organic compounds analysis as a potential novel screening tool for colorectal cancer, *Medicine*. 99 (2020) e20937. <https://doi.org/10.1097/MD.00000000000020937>.
- [56] S. De Silva, A Review of “Cutting the Fuse: The Explosion of Global Suicide Terrorism and How to Stop It,” *Studies in Conflict & Terrorism*. (2011). <https://doi.org/10.1080/1057610x.2011.611934>.
- [57] Y. Geng, M.A. Ali, A.J. Clulow, S. Fan, P.L. Burn, I.R. Gentle, P. Meredith, P.E. Shaw, Unambiguous detection of nitrated explosive vapours by fluorescence quenching of dendrimer films, *Nature Communications*. (2015). <https://doi.org/10.1038/ncomms9240>.
- [58] B. Gole, W. Song, M. Lackinger, P.S. Mukherjee, Explosives sensing by using electron-rich supramolecular polymers: Role of intermolecular hydrogen bonding in significant enhancement of sensitivity, *Chemistry - A European Journal*. (2014). <https://doi.org/10.1002/chem.201403345>.

- [59] N. Dey, S.K. Samanta, S. Bhattacharya, Selective and efficient detection of nitro-aromatic explosives in multiple media including water, micelles, organogel, and solid support, *ACS Applied Materials and Interfaces*. (2013). <https://doi.org/10.1021/am401608q>.
- [60] W. Huang, E. Smarsly, J. Han, M. Bender, K. Seehafer, I. Wacker, R.R. Schröder, U.H.F. Bunz, Truxene-based hyperbranched conjugated polymers: Fluorescent micelles detect explosives in water, *ACS Applied Materials and Interfaces*. (2017). <https://doi.org/10.1021/acsami.6b12419>.
- [61] H. Nie, G. Sun, M. Zhang, M. Baumgarten, K. Müllen, Fluorescent conjugated polycarbazoles for explosives detection: Side chain effects on TNT sensor sensitivity, *Journal of Materials Chemistry*. (2012). <https://doi.org/10.1039/c1jm14691b>.
- [62] Y. Long, H. Chen, H. Wang, Z. Peng, Y. Yang, G. Zhang, N. Li, F. Liu, J. Pei, Highly sensitive detection of nitroaromatic explosives using an electrospun nanofibrous sensor based on a novel fluorescent conjugated polymer, *Analytica Chimica Acta*. (2012). <https://doi.org/10.1016/j.aca.2012.07.028>.
- [63] F. Chu, G. Tsiminis, N.A. Spooner, T.M. Monro, Explosives detection by fluorescence quenching of conjugated polymers in suspended core optical fibers, *Sensors and Actuators, B: Chemical*. (2014). <https://doi.org/10.1016/j.snb.2014.03.031>.
- [64] P.A. Pella, Generator for Producing Trace Vapor Concentrations of 2,4,6-Trinitrotoluene, 2,4-Dinitrotoluene, and Ethylene Glycol Dinitrate for Calibrating Explosives Vapor Detectors, *Analytical Chemistry*. (1976). <https://doi.org/10.1021/ac50005a054>.
- [65] D.E.G. Jones, R.A. Augsten, K.K. Feng, Detection agents for explosives, *Journal of Thermal Analysis and Calorimetry*. (1995). <https://doi.org/10.1007/BF02636273>.
- [66] S. Khan, D. Newport, S. Le Calvé, Development of a Toluene detector based on deep UV absorption spectrophotometry using glass and aluminum capillary Tube Gas Cells with a LED source, *Micromachines (Basel)*. (2019). <https://doi.org/10.3390/mi10030193>.
- [67] M. Woollam, M. Teli, P. Angarita-Rivera, S. Liu, A.P. Siegel, H. Yokota, M. Agarwal, Detection of Volatile Organic Compounds (VOCs) in Urine via Gas Chromatography-Mass Spectrometry QTOF to Differentiate Between Localized and Metastatic Models of Breast Cancer, *Scientific Reports*. (2019). <https://doi.org/10.1038/s41598-019-38920-0>.
- [68] I.A. Ratiu, V. Bocos-Bintintan, A. Patrut, V.H. Moll, M. Turner, C.L.P. Thomas, Discrimination of bacteria by rapid sensing their metabolic volatiles using an aspiration-type ion mobility spectrometer (a-IMS) and gas chromatography-mass spectrometry GC-MS, *Analytica Chimica Acta*. (2017). <https://doi.org/10.1016/j.aca.2017.06.031>.
- [69] V.-M. Dospinescu, A. Tiele, J. Covington, Sniffing Out Urinary Tract Infection—Diagnosis Based on Volatile Organic Compounds and Smell Profile, *Biosensors (Basel)*. 10 (2020) 83. <https://doi.org/10.3390/bios10080083>.
- [70] V.S. Langford, I. Graves, M.J. McEwan, Rapid monitoring of volatile organic compounds: A comparison between gas chromatography/mass spectrometry and selected ion flow tube mass spectrometry, *Rapid Communications in Mass Spectrometry*. (2014). <https://doi.org/10.1002/rcm.6747>.
- [71] T. Majchrzak, W. Wojnowski, M. Lubinska-Szczygeł, A. Różańska, J. Namieśnik, T. Dymerski, PTR-MS and GC-MS as complementary techniques for analysis of volatiles: A tutorial review, *Analytica Chimica Acta*. (2018). <https://doi.org/10.1016/j.aca.2018.06.056>.
- [72] A. Dey, Semiconductor metal oxide gas sensors: A review, *Materials Science and Engineering B: Solid-State Materials for Advanced Technology*. (2018). <https://doi.org/10.1016/j.mseb.2017.12.036>.

- [73] X. Zhou, Y. Wang, J. Wang, Z. Xie, X. Wu, N. Han, Y. Chen, Amplifying the Signal of Metal Oxide Gas Sensors for Low Concentration Gas Detection, *IEEE Sensors Journal*. 17 (2017) 2841–2847. <https://doi.org/10.1109/JSEN.2017.2678985>.
- [74] R. Jaaniso, O.K. Tan, *Semiconductor gas sensors*, 2019. <https://doi.org/10.1016/C2017-0-00001-0>.
- [75] J.S. Wilson, *Sensor Technology Handbook*, 2005. <https://doi.org/10.1016/B978-0-7506-7729-5.X5040-X>.
- [76] R.M. White, A Sensor Classification Scheme, *IEEE Transactions on Ultrasonics, Ferroelectrics, and Frequency Control*. (1987). <https://doi.org/10.1109/T-UFFC.1987.26922>.
- [77] A. Hulanicki, S. Glab, F. Ingman, Chemical sensors definitions and classification, *Pure and Applied Chemistry*. (1991). <https://doi.org/10.1351/pac199163091247>.
- [78] W. Wang, Introductory Chapter: What is Chemical Sensor?, in: *Progresses in Chemical Sensor*, InTech, 2016. <https://doi.org/10.5772/64626>.
- [79] G. Sumana, M. Das, S. Srivastava, B.D. Malhotra, A novel urea biosensor based on zirconia, *Thin Solid Films*. 519 (2010) 1187–1191. <https://doi.org/10.1016/j.tsf.2010.08.067>.
- [80] A. Husain, S. Ahmad, F. Mohammad, Thermally stable and highly sensitive ethene gas sensor based on polythiophene/zirconium oxide nanocomposites, *Materials Today Communications*. 20 (2019) 100574. <https://doi.org/10.1016/j.mtcomm.2019.100574>.
- [81] G. Eranna, *Metal Oxide Nanostructures as Gas Sensing Devices*, 2011.
- [82] G.B. Shelke, Gas Sensing Performance of Pure and Modified Nanostructured Screen Printed Zirconia Thick Films, 8 (2019) 198–202.
- [83] S.B. Deshmukh, Comparative studies and gas sensing performance of bulk ZrO₂ thick and nanostructured ZrO₂ thin films, (2019).
- [84] S. Mahajan, S. Jagtap, Metal-oxide semiconductors for carbon monoxide (CO) gas sensing: A review, *Applied Materials Today*. 18 (2020) 100483. <https://doi.org/https://doi.org/10.1016/j.apmt.2019.100483>.
- [85] J. Antônio Pinheiro Lobo, J. Rodrigues dos Santos, O. Vital de Oliveira, E. Longo da Silva, J. Divino dos Santos, Theoretical study of greenhouse gases on the zirconium oxide nanotube surface, *Chemical Physics Letters*. 745 (2020) 137236. <https://doi.org/10.1016/j.cplett.2020.137236>.
- [86] S. Zhou, M. Hu, X. Huang, N. Zhou, Z. Zhang, M. Wang, Y. Liu, L. He, Electrospun zirconium oxide embedded in graphene-like nanofiber for aptamer-based impedimetric bioassay toward osteopontin determination, *Microchimica Acta*. 187 (2020) 219. <https://doi.org/10.1007/s00604-020-4187-x>.
- [87] M.H. Boratto, M. Congiu, S.B.O. dos Santos, L.V.A. Scalvi, Annealing temperature influence on sol-gel processed zirconium oxide thin films for electronic applications, *Ceramics International*. 44 (2018) 10790–10796. <https://doi.org/https://doi.org/10.1016/j.ceramint.2018.03.117>.
- [88] M.T. Soo, N. Prastomo, A. Matsuda, G. Kawamura, H. Muto, A.F.M. Noor, Z. Lockman, K.Y. Cheong, Elaboration and characterization of sol-gel derived ZrO₂ thin films treated with hot water, *Applied Surface Science*. 258 (2012) 5250–5258. <https://doi.org/10.1016/j.apsusc.2012.02.008>.
- [89] A. Ortiz, J.C. Alonso, E. Haro-Poniatowski, Spray deposition and characterization of zirconium-oxide thin films, *Journal of Electronic Materials*. 34 (2005) 150–155. <https://doi.org/10.1007/s11664-005-0226-y>.
- [90] M. Rawat, A. Das, D.K. Shukla, P. Rajput, A. Chettah, D.M. Phase, R.C. Ramola, F. Singh, Micro-Raman and electronic structure study on kinetics of electronic excitations induced monoclinic-to-

tetragonal phase transition in zirconium oxide films, *RSC Advances*. 6 (2016) 104425–104432. <https://doi.org/10.1039/C6RA14199D>.

- [91] L. Kumari, W. Li, D. Wang, Monoclinic zirconium oxide nanostructures synthesized by a hydrothermal route, *Nanotechnology*. 19 (2008) 195602. <https://doi.org/10.1088/0957-4484/19/19/195602>.
- [92] M.A. Mohammed, Structural, Optical, Electrical and Gas Sensor Properties of ZrO₂ Thin Films prepared by Sol-Gel Technique, *NeuroQuantology*. 18 (2020) 22–27. <https://doi.org/10.14704/nq.2020.18.3.NQ20146>.
- [93] S. Zhuiykov, *Electrochemistry of Zirconia Gas Sensors*, CRC Press, 2007. <https://doi.org/10.1201/9781420047622>.
- [94] W.C. Maskell, Progress in the development of zirconia gas sensors, *Solid State Ionics*. 134 (2000) 43–50. [https://doi.org/https://doi.org/10.1016/S0167-2738\(00\)00712-8](https://doi.org/https://doi.org/10.1016/S0167-2738(00)00712-8).
- [95] I.L.V. Rosa, F.A. Tavares, A.P. de Moura, I.M. Pinatti, L.F. da Silva, M.S. Li, E. Longo, Luminescent and gas sensor properties of the ZrO₂:Hhpa:Eu³⁺ Hybrid Compound, *Journal of Luminescence*. 197 (2018) 38–46. <https://doi.org/10.1016/j.jlumin.2017.12.046>.
- [96] C. Zhu, A. Liu, G. Liu, G. Jiang, Y. Meng, E. Fortunato, R. Martins, F. Shan, Low-temperature, nontoxic water-induced high-k zirconium oxide dielectrics for low-voltage, high-performance oxide thin-film transistors, *Journal of Materials Chemistry C*. 4 (2016) 10715–10721. <https://doi.org/10.1039/C6TC02607A>.
- [97] L. Chen, Y. Liu, Y. Li, Preparation and characterization of ZrO₂:Eu³⁺ phosphors, *Journal of Alloys and Compounds*. 381 (2004) 266–271. <https://doi.org/https://doi.org/10.1016/j.jallcom.2004.03.102>.
- [98] M.A. Navarra, C. Abbati, B. Scrosati, Properties and fuel cell performance of a Nafion-based, sulfated zirconia-added, composite membrane, *Journal of Power Sources*. 183 (2008) 109–113. <https://doi.org/https://doi.org/10.1016/j.jpowsour.2008.04.033>.
- [99] J. Seth, P. Dubey, V.R. Chaudhari, B.L. V. Prasad, Preparation of metal oxide supported catalysts and their utilization for understanding the effect of a support on the catalytic activity, *New Journal of Chemistry*. 42 (2018) 402–410. <https://doi.org/10.1039/C7NJ03753H>.
- [100] H.K. Yueh, B. Cox, Luminescence properties of zirconium oxide films, *Journal of Nuclear Materials*. 323 (2003) 57–67. <https://doi.org/https://doi.org/10.1016/j.jnucmat.2003.08.025>.
- [101] S. V Nikiforov, V.S. Kortov, M.G. Kazantseva, K.A. Petrovykh, Luminescent properties of monoclinic zirconium oxide, *Journal of Luminescence*. 166 (2015) 111–116. <https://doi.org/https://doi.org/10.1016/j.jlumin.2015.05.021>.
- [102] T. V. Perevalov, D. V. Gulyaev, V.S. Aliev, K.S. Zhuravlev, V.A. Gritsenko, A.P. Yelisseyev, The origin of 2.7 eV blue luminescence band in zirconium oxide, *Journal of Applied Physics*. 116 (2014) 244109. <https://doi.org/10.1063/1.4905105>.
- [103] Y. Chu, Q. Zhang, Y. Li, Z. Xu, W. Long, A cataluminescence sensor for propionaldehyde based on the use of nanosized zirconium dioxide, *Microchimica Acta*. (2014). <https://doi.org/10.1007/s00604-014-1220-y>.
- [104] F. Teng, Y. Zhu, G. He, G. Gao, D.D. Meng, Cataluminescence and Catalysis Properties of CO Oxidation Over Porous Network of ZrO₂ Nanorods Synthesized by a Bio-Template, *The Open Catalysis Journal*. 2 (2009) 86–91. <https://doi.org/10.2174/1876214X00902010086>.
- [105] A. Patra, C.S. Friend, R. Kapoor, P.N. Prasad, Upconversion in Er³⁺:ZrO₂ Nanocrystals, *The Journal of Physical Chemistry B*. 106 (2002) 1909–1912. <https://doi.org/10.1021/jp013576z>.

- [106] E. De la Rosa-Cruz, L.A. Diaz-Torres, P. Salas, R.A. Rodríguez, G.A. Kumar, M.A. Meneses, J.F. Mosiño, J.M. Hernández, O. Barbosa-García, Luminescent properties and energy transfer in ZrO₂:Sm³⁺ nanocrystals, *Journal of Applied Physics*. 94 (2003) 3509–3515. <https://doi.org/10.1063/1.1599960>.
- [107] G. Cabello, L. Lillo, C. Caro, G.E. Buono-Core, B. Chornik, M.A. Soto, Structure and optical characterization of photochemically prepared ZrO₂ thin films doped with erbium and europium, *Journal of Non-Crystalline Solids*. 354 (2008) 3919–3928. <https://doi.org/https://doi.org/10.1016/j.jnoncrysol.2008.05.029>.
- [108] Z. Zhang, K. Xu, W.R.G. Baeyens, X. Zhang, An energy-transfer cataluminescence reaction on nanosized catalysts and its application to chemical sensors, *Analytica Chimica Acta*. (2005). <https://doi.org/10.1016/j.aca.2004.12.025>.
- [109] J. Zhou, R. Lei, H. Wang, Y. Hua, D. Li, Q. Yang, D. Deng, S. Xu, A new generation of dual-mode optical thermometry based on ZrO₂:Eu³⁺ nanocrystals, *Nanophotonics*. 8 (2019) 2347–2358. <https://doi.org/doi:10.1515/nanoph-2019-0359>.
- [110] S. Manjunatha, R. Hari Krishna, T. Thomas, B.S. Panigrahi, M.S. Dharmaparakash, Moss-Burstein effect in stable, cubic ZrO₂: Eu³⁺ nanophosphors derived from rapid microwave-assisted solution-combustion technique, *Materials Research Bulletin*. 98 (2018) 139–147. <https://doi.org/https://doi.org/10.1016/j.materresbull.2017.10.006>.
- [111] V.K. Singh, S. Tripathi, M.K. Mishra, R. Tiwari, V. Dubey, N. Tiwari, Optical Studies of Erbium and Ytterbium Doped Gd₂Zr₂O₇ Phosphor for Display and Optical Communication Applications, *J. Display Technol.* 12 (2016) 1224–1228.
- [112] H. Guzmán, M.A. Farkhondehfal, K.R. Tolod, S. Hernández, N. Russo, Chapter 11 - Photo/electrocatalytic hydrogen exploitation for CO₂ reduction toward solar fuels production, in: F. Calise, M.D. D'Accadia, M. Santarelli, A. Lanzini, D. Ferrero (Eds.), *Solar Hydrogen Production*, Academic Press, 2019: pp. 365–418. <https://doi.org/https://doi.org/10.1016/B978-0-12-814853-2.00011-4>.
- [113] H. Yu, Z. Song, Q. Liu, X. Ji, J. Liu, S. Xu, H. Kan, B. Zhang, J. Liu, J. Jiang, L. Miao, H. Liu, Colloidal synthesis of tungsten oxide quantum dots for sensitive and selective H₂S gas detection, *Sensors and Actuators B: Chemical*. 248 (2017) 1029–1036. <https://doi.org/10.1016/j.snb.2017.03.044>.
- [114] W. Zhang, Y. Fan, T. Yuan, B. Lu, Y. Liu, Z. Li, G. Li, Z. Cheng, J. Xu, Ultrafine Tungsten Oxide Nanowires: Synthesis and Highly Selective Acetone Sensing and Mechanism Analysis, *ACS Applied Materials & Interfaces*. 12 (2020) 3755–3763. <https://doi.org/10.1021/acsami.9b19706>.
- [115] S. Ramanavičius, M. Petrulevičienė, J. Juodkazytė, A. Grigucevičienė, A. Ramanavičius, Selectivity of Tungsten Oxide Synthesized by Sol-Gel Method Towards Some Volatile Organic Compounds and Gaseous Materials in a Broad Range of Temperatures, *Materials*. 13 (2020) 523. <https://doi.org/10.3390/ma13030523>.
- [116] X.-L. Li, T.-J. Lou, X.-M. Sun, Y.-D. Li, Highly Sensitive WO₃ Hollow-Sphere Gas Sensors, *Inorganic Chemistry*. 43 (2004) 5442–5449. <https://doi.org/10.1021/ic049522w>.
- [117] Y. Yao, M. Yin, J. Yan, S. (Frank) Liu, P-type sub-tungsten-oxide based urchin-like nanostructure for superior room temperature alcohol sensor, *Applied Surface Science*. 441 (2018) 277–284. <https://doi.org/10.1016/j.apsusc.2018.02.004>.
- [118] S. Vallejos, T. Stoycheva, P. Umek, C. Navio, R. Snyders, C. Bittencourt, E. Llobet, C. Blackman, S. Moniz, X. Correig, Au nanoparticle-functionalised WO₃ nanoneedles and their application in high

sensitivity gas sensor devices, *Chem. Commun.* 47 (2011) 565–567.
<https://doi.org/10.1039/C0CC02398A>.

- [119] Z.L. Wang, Zinc oxide nanostructures: growth, properties and applications, 16 (2004) R829--R858.
<https://doi.org/10.1088/0953-8984/16/25/r01>.
- [120] G.S. Zeedan, K.A.A. EL-Razik, A.M. Allam, A.M. Abdalhamed, H.A.A. Zeina, Evaluations of Potential Antiviral Effects of Green Zinc Oxide and Silver Nanoparticles against Bovine Herpesvirus-1, *Advances in Animal and Veterinary Sciences*. 8 (2020).
<https://doi.org/10.17582/journal.aavs/2020/8.4.433.443>.
- [121] J. Liu, X. Feng, L. Wei, L. Chen, B. Song, L. Shao, The toxicology of ion-shedding zinc oxide nanoparticles, *Critical Reviews in Toxicology*. 46 (2016) 348–384.
<https://doi.org/10.3109/10408444.2015.1137864>.
- [122] L. He, Y. Liu, A. Mustapha, M. Lin, Antifungal activity of zinc oxide nanoparticles against *Botrytis cinerea* and *Penicillium expansum*, *Microbiological Research*. 166 (2011) 207–215.
<https://doi.org/10.1016/j.micres.2010.03.003>.
- [123] J.G. Claus F. Klingshirn, Andreas Waag, Axel Hoffmann, *Zinc Oxide: From Fundamental Properties Towards Novel Applications*, 2010.
- [124] M. Que, C. Lin, J. Sun, L. Chen, X. Sun, Y. Sun, Progress in ZnO Nanosensors, *Sensors*. 21 (2021).
<https://doi.org/10.3390/s21165502>.
- [125] R. Kumar, O. Al-Dossary, G. Kumar, A. Umar, Zinc Oxide Nanostructures for NO₂ Gas–Sensor Applications: A Review, *Nano-Micro Letters*. 7 (2015) 97–120. <https://doi.org/10.1007/s40820-014-0023-3>.
- [126] Q.A. Drmash, I. Olanrewaju Alade, M. Qamar, S. Akbar, Zinc Oxide-Based Acetone Gas Sensors for Breath Analysis: A Review, *Chemistry – An Asian Journal*. 16 (2021) 1519–1538.
<https://doi.org/10.1002/asia.202100303>.
- [127] Y. Tu, C. Kyle, H. Luo, D.-W. Zhang, A. Das, J. Briscoe, S. Dunn, M.-M. Titirici, S. Krause, Ammonia Gas Sensor Response of a Vertical Zinc Oxide Nanorod-Gold Junction Diode at Room Temperature, *ACS Sensors*. 5 (2020) 3568–3575. <https://doi.org/10.1021/acssensors.0c01769>.
- [128] V. Myndrul, E. Coy, M. Bechelany, I. Iatsunskyi, Photoluminescence label-free immunosensor for the detection of Aflatoxin B1 using polyacrylonitrile/zinc oxide nanofibers, *Materials Science and Engineering: C*. 118 (2021) 111401. <https://doi.org/https://doi.org/10.1016/j.msec.2020.111401>.
- [129] G. Biasotto, M.G.A. Ranieri, C.R. Foschini, A.Z. Simões, E. Longo, M.A. Zaghete, Gas sensor applications of zinc oxide thin film grown by the polymeric precursor method, *Ceramics International*. 40 (2014) 14991–14996. <https://doi.org/10.1016/j.ceramint.2014.06.099>.
- [130] D. Polese, I. Lucarini, A. Convertino, F. Maita, G. Fortunato, L. Maiolo, Room temperature gas sensors based on laser-annealed ZnO nanostructures for gaseous pollutants detection, in: *2019 IEEE SENSORS*, 2019: pp. 1–4. <https://doi.org/10.1109/SENSORS43011.2019.8956909>.
- [131] P.R. Solanki, A. Kaushik, V. V Agrawal, B.D. Malhotra, Nanostructured metal oxide-based biosensors, *NPG Asia Materials*. 3 (2011) 17–24. <https://doi.org/10.1038/asiamat.2010.137>.
- [132] Y.F. Sun, S.B. Liu, F.L. Meng, J.Y. Liu, Z. Jin, L.T. Kong, J.H. Liu, Metal oxide nanostructures and their gas sensing properties: A review, *Sensors*. (2012). <https://doi.org/10.3390/s120302610>.
- [133] O.S. Kwon, J.-Y. Hong, S.J. Park, Y. Jang, J. Jang, Resistive Gas Sensors Based on Precisely Size-Controlled Polypyrrole Nanoparticles: Effects of Particle Size and Deposition Method, *The Journal of Physical Chemistry C*. 114 (2010) 18874–18879. <https://doi.org/10.1021/jp1083086>.

- [134] A.R. Barron, *Physical Methods in Chemistry and Nano Science*, Rice University, 2015.
- [135] M. Batzill, U. Diebold, The surface and materials science of tin oxide, *Progress in Surface Science*. 79 (2005) 47–154. <https://doi.org/10.1016/j.progsurf.2005.09.002>.
- [136] H.J. Kim, J.H. Lee, Highly sensitive and selective gas sensors using p-type oxide semiconductors: Overview, *Sensors and Actuators, B: Chemical*. 192 (2014) 607–627. <https://doi.org/10.1016/j.snb.2013.11.005>.
- [137] H.-R. Kim, A. Haensch, I.-D. Kim, N. Barsan, U. Weimar, J.-H. Lee, The Role of NiO Doping in Reducing the Impact of Humidity on the Performance of SnO₂-Based Gas Sensors: Synthesis Strategies, and Phenomenological and Spectroscopic Studies, *Advanced Functional Materials*. 21 (2011) 4456–4463. <https://doi.org/10.1002/adfm.201101154>.
- [138] M.V. Nikolic, V. Milovanovic, Z.Z. Vasiljevic, Z. Stamenkovic, *Semiconductor Gas Sensors: Materials, Technology, Design, and Application*, *Sensors*. 20 (2020) 6694. <https://doi.org/10.3390/s20226694>.
- [139] M. Hübner, C.E. Simion, A. Tomescu-Stănoiu, S. Pokhrel, N. Bârsan, U. Weimar, Influence of humidity on CO sensing with p-type CuO thick film gas sensors, *Sensors and Actuators B: Chemical*. 153 (2011) 347–353. <https://doi.org/10.1016/j.snb.2010.10.046>.
- [140] T. Seiyama, A. Kato, K. Fujiishi, M. Nagatani, A New Detector for Gaseous Components Using Semiconductive Thin Films, *Analytical Chemistry*. (1962). <https://doi.org/10.1021/ac60191a001>.
- [141] Z. Fu, G. Li, Y. Hu, [The Progress on Cataluminescence-Based Analytical System]., *Guang Pu Xue Yu Guang Pu Fen Xi*. 35 (2015) 2450–2456.
- [142] M. Breyse, B. Claudel, L. Faure, M. Guenin, R.J.J. Williams, T. Wolkenstein, Chemiluminescence during the catalysis of carbon monoxide oxidation on a thoria surface, *Journal of Catalysis*. (1976). [https://doi.org/10.1016/0021-9517\(76\)90129-9](https://doi.org/10.1016/0021-9517(76)90129-9).
- [143] J. Hu, L. Zhang, Y. Lv, Recent advances in cataluminescence gas sensor: Materials and methodologies, *Applied Spectroscopy Reviews*. (2019). <https://doi.org/10.1080/05704928.2018.1464932>.
- [144] S. Wang, Z. Yuan, L. Zhang, Y. Lin, C. Lu, Recent advances in cataluminescence-based optical sensing systems, *Analyst*. (2017). <https://doi.org/10.1039/c7an00091j>.
- [145] M. Nakagawa, N. Yamashita, Cataluminescence-Based Gas Sensors, in: *Frontiers in Chemical Sensors*, 2005. https://doi.org/10.1007/5346_003.
- [146] V. Kiisk, R. Jaaniso, Rare earth-doped oxide materials for photoluminescence-based gas sensors, in: *Semiconductor Gas Sensors*, 2019. <https://doi.org/10.1016/B978-0-08-102559-8.00009-4>.
- [147] R. Zhang, X. Cao, Y. Liu, X. Chang, Development of a Simple Cataluminescence Sensor System for Detecting and Discriminating Volatile Organic Compounds at Different Concentrations, *Analytical Chemistry*. 85 (2013) 3802–3806. <https://doi.org/10.1021/ac400208k>.
- [148] L. Zhang, H. Song, Y. Su, Y. Lv, Advances in nanomaterial-assisted cataluminescence and its sensing applications, *TrAC Trends in Analytical Chemistry*. 67 (2015) 107–127. <https://doi.org/10.1016/j.trac.2015.01.008>.
- [149] X. Huang, Z. Huang, L. Zhang, R. Liu, Y. Lv, Highly efficient cataluminescence gas sensor for acetone vapor based on UIO-66 metal-organic frameworks as preconcentrator, *Sensors and Actuators B: Chemical*. 312 (2020) 127952. <https://doi.org/https://doi.org/10.1016/j.snb.2020.127952>.

- [150] A. Mirzaei, H.W. Kim, S.S. Kim, G. Neri, Nanostructured Semiconducting Metal Oxide Gas Sensors for Acetaldehyde Detection, *Chemosensors*. 7 (2019) 56. <https://doi.org/10.3390/chemosensors7040056>.
- [151] K. Zhou, X. Ji, N. Zhang, X. Zhang, On-line monitoring of formaldehyde in air by cataluminescence-based gas sensor, *Sensors and Actuators B: Chemical*. 119 (2006) 392–397. <https://doi.org/https://doi.org/10.1016/j.snb.2005.12.038>.
- [152] J. Hu, L. Zhang, H. Song, J. Hu, Y. Lv, Ratiometric Cataluminescence for Rapid Recognition of Volatile Organic Compounds Based on Energy Transfer Process, *Analytical Chemistry*. 91 (2019) 4860–4867. <https://doi.org/10.1021/acs.analchem.9b00592>.
- [153] L. Li, Y. Yang, D. Deng, H. Song, Y. Lv, Photocatalysis enhanced cataluminescence gas sensor for carbon monoxide based on perylenetetracarboxylic diimide, *Sensors and Actuators B: Chemical*. 315 (2020) 128080. <https://doi.org/https://doi.org/10.1016/j.snb.2020.128080>.
- [154] X. Huang, S. Yan, D. Deng, L. Zhang, R. Liu, Y. Lv, Novel Strategy for Engineering the Metal-Oxide@MOF Core@Shell Architecture and Its Applications in Cataluminescence Sensing, *ACS Applied Materials & Interfaces*. 13 (2021) 3471–3480. <https://doi.org/10.1021/acsami.0c20799>.
- [155] Y. Bian, L. Li, H. Song, Y. Su, Y. Lv, Porous boron nitride: A novel metal-free cataluminescence material for high performance H₂S sensing, *Sensors and Actuators B: Chemical*. 332 (2021) 129512. <https://doi.org/10.1016/j.snb.2021.129512>.
- [156] D. Wong, O. Abuzalat, J. Ko, J. Lee, S. Kim, S.S. Park, Intense Pulsed Light-Treated Near-Field Electrospun Nanofiber on a Quartz Tuning Fork for Multimodal Gas Sensors, *ACS Applied Materials & Interfaces*. 12 (2020) 24308–24318. <https://doi.org/10.1021/acsami.0c02263>.
- [157] M. Bouvet, J.-M. Suisse, T. Sizun, A. Kumar, G. Barochi, B. De Fonseca, J. Rossignol, The multimodal detection as a tool for molecular material-based gas sensing, *Sensors and Actuators B: Chemical*. 187 (2013) 204–208. <https://doi.org/https://doi.org/10.1016/j.snb.2012.10.083>.
- [158] F. Invention, *Sensors for Volatile Compounds*, (2014) 1–27.
- [159] M. Fois, T. Cox, N. Ratcliffe, B. de Lacy Costello, Rare Earth Doped Metal Oxide Sensor for the Multimodal Detection of Volatile Organic Compounds (VOCs), *Sensors and Actuators B: Chemical*. (2020). <https://doi.org/10.1016/j.snb.2020.129264>.
- [160] P. Narkhede, R. Walambe, S. Mandaokar, P. Chandel, K. Kotecha, G. Ghinea, Gas detection and identification using multimodal artificial intelligence based sensor fusion, *Applied System Innovation*. 4 (2021) 1–14. <https://doi.org/10.3390/asi4010003>.
- [161] H. Gong, J.Q. Hu, J.H. Wang, C.H. Ong, F.R. Zhu, Nano-crystalline Cu-doped ZnO thin film gas sensor for CO, *Sensors and Actuators B: Chemical*. 115 (2006) 247–251. <https://doi.org/10.1016/j.snb.2005.09.008>.
- [162] M. Fleischer, S. Kornely, T. Weh, J. Frank, H. Meixner, Selective gas detection with high-temperature operated metal oxides using catalytic filters, *Sensors and Actuators B: Chemical*. 69 (2000) 205–210. [https://doi.org/https://doi.org/10.1016/S0925-4005\(00\)00513-X](https://doi.org/https://doi.org/10.1016/S0925-4005(00)00513-X).
- [163] C.O. Park, S.A. Akbar, J. Hwang, Selective gas detection with catalytic filter, *Materials Chemistry and Physics*. 75 (2002) 56–60. [https://doi.org/https://doi.org/10.1016/S0254-0584\(02\)00030-5](https://doi.org/https://doi.org/10.1016/S0254-0584(02)00030-5).
- [164] J. Lee, Y. Jung, S.-H. Sung, G. Lee, J. Kim, J. Seong, Y.-S. Shim, S.C. Jun, S. Jeon, High-performance gas sensor array for indoor air quality monitoring: the role of Au nanoparticles on WO₃, SnO₂, and NiO-based gas sensors, *Journal of Materials Chemistry A*. 9 (2021) 1159–1167. <https://doi.org/10.1039/D0TA08743B>.

- [165] H. Song, Q. Li, Y. Zhang, CNT-based sensor array for selective and steady detection of SO₂ and NO, *Materials Research Bulletin*. 124 (2020) 110772. <https://doi.org/https://doi.org/10.1016/j.materresbull.2020.110772>.
- [166] G.S. Kim, Y. Park, J. Shin, Y.G. Song, C.-Y. Kang, Metal Oxide Nanorods-Based Sensor Array for Selective Detection of Biomarker Gases, *Sensors*. 21 (2021). <https://doi.org/10.3390/s21051922>.
- [167] S. Sagadevan, J. Podder, I. Das, Hydrothermal synthesis of zirconium oxide nanoparticles and its characterization, *Journal of Materials Science: Materials in Electronics*. 27 (2016) 5622–5627. <https://doi.org/10.1007/s10854-016-4469-6>.
- [168] A.K. Arora, P. Kumar, Prebiotic studies on the interaction of zirconia nanoparticles and ribose nucleotides and their role in chemical evolution, *International Journal of Astrobiology*. 20 (2021) 142–149. <https://doi.org/10.1017/S1473550421000033>.
- [169] M.R.H. Siddiqui, A.I. Al-Wassil, A.M. Al-Otaibi, R.M. Mahfouz, Effects of precursor on the morphology and size of ZrO₂ nanoparticles, synthesized by sol-gel method in non-aqueous medium, *Materials Research*. 15 (2012) 986–989. <https://doi.org/10.1590/S1516-14392012005000128>.
- [170] Y. Hui, B. Zou, S. Liu, S. Zhao, J. Xu, Y. Zhao, X. Fan, L. Zhu, Y. Wang, X. Cao, Effects of Eu³⁺-doping and annealing on structure and fluorescence of zirconia phosphors, *Ceramics International*. (2015). <https://doi.org/10.1016/j.ceramint.2014.10.091>.
- [171] S. Ahlers, G. Müller, T. Doll, A rate equation approach to the gas sensitivity of thin film metal oxide materials, *Sensors and Actuators, B: Chemical*. (2005). <https://doi.org/10.1016/j.snb.2004.11.020>.
- [172] A.S. Keiteb, E. Saion, A. Zakaria, N. Soltani, Structural and Optical Properties of Zirconia Nanoparticles by Thermal Treatment Synthesis, *Journal of Nanomaterials*. 2016 (2016) 1–6. <https://doi.org/10.1155/2016/1913609>.
- [173] A.K. Singh, U.T. Nakate, Microwave Synthesis, Characterization, and Photoluminescence Properties of Nanocrystalline Zirconia, *The Scientific World Journal*. 2014 (2014) 1–7. <https://doi.org/10.1155/2014/349457>.
- [174] G. Ehrhart, M. Bouazaoui, B. Capoen, V. Ferreiro, R. Mahiou, O. Robbe, S. Turrell, Effects of rare-earth concentration and heat-treatment on the structural and luminescence properties of europium-doped zirconia sol-gel planar waveguides, *Opt Mater (Amst)*. 29 (2007) 1723–1730. <https://doi.org/10.1016/j.optmat.2006.09.006>.
- [175] M. Ahmadi, M. Guinel, Large-Scale Synthesis of Tungsten Oxide (WO₃) Nanoleaves, Nanoparticles and Nanoflakes, *Microscopy and Microanalysis*. 19 (2013) 1580–1581. <https://doi.org/10.1017/S1431927613009896>.
- [176] S.-J. Wang, M.-C. Wang, S.-F. Chen, Y.-H. Li, T.-S. Shen, H.-Y. Bor, C.-N. Wei, Electrical and Physical Characteristics of WO₃/Ag/WO₃ Sandwich Structure Fabricated with Magnetic-Control Sputtering Metrology †, *Sensors*. 18 (2018) 2803. <https://doi.org/10.3390/s18092803>.
- [177] C.-M. Wu, S. Naseem, M.-H. Chou, J.-H. Wang, Y.-Q. Jian, Recent Advances in Tungsten-Oxide-Based Materials and Their Applications, *Frontiers in Materials*. 6 (2019). <https://doi.org/10.3389/fmats.2019.00049>.
- [178] Z. Hai, Z. Wei, C. Xue, H. Xu, F. Verpoort, Nanostructured tungsten oxide thin film devices: from optoelectronics and ionics to iontronics, *Journal of Materials Chemistry C*. 7 (2019) 12968–12990. <https://doi.org/10.1039/C9TC04489B>.

- [179] J. Kaur, K. Anand, K. Anand, R.C. Singh, WO₃ nanolamellae/reduced graphene oxide nanocomposites for highly sensitive and selective acetone sensing, *Journal of Materials Science*. 53 (2018) 12894–12907. <https://doi.org/10.1007/s10853-018-2558-z>.
- [180] N. Vuong, D. Kim, H. Kim, Porous Au-embedded WO₃ Nanowire Structure for Efficient Detection of CH₄ and H₂S, *Scientific Reports*. 5 (2015). <https://doi.org/10.1038/srep11040>.
- [181] K. He, Z. Jin, X. Chu, W. Bi, W. Wang, C. Wang, S. Liu, Fast response–recovery time toward acetone by a sensor prepared with Pd doped WO₃ nanosheets, *RSC Advances*. 9 (2019) 28439–28450. <https://doi.org/10.1039/C9RA04429A>.
- [182] Y. Sun, L. Chen, Y.Z. Wang, Z. Zhao, P. Li, W. Zhang, Y. Leprince-Wang, J. Hu, Synthesis of MoO₃/WO₃ composite nanostructures for highly sensitive ethanol and acetone detection, *Journal of Materials Science*. 52 (2016) 1561–1572.
- [183] J. Xiao, Y. Che, B. Lv, M.-C. Benedicte, G. Feng, T. Sun, C. Song, Synthesis of WO₃ Nanorods and Their Excellent Ethanol Gas-Sensing Performance, *Materials Research*. 24 (2021). <https://doi.org/10.1590/1980-5373-mr-2020-0434>.
- [184] Y. Chu, Q. Zhang, Y. Li, Z. Xu, W. Long, A cataluminescence sensor for propionaldehyde based on the use of nanosized zirconium dioxide, *Microchimica Acta*. 181 (2014) 1125–1132. <https://doi.org/10.1007/s00604-014-1220-y>.
- [185] H. Peng, P. Liu, W. Wu, W. Chen, X. Meng, X. Lin, A. Liu, Facile electrochemiluminescence sensing platform based on water-soluble tungsten oxide quantum dots for ultrasensitive detection of dopamine released by cells, *Analytica Chimica Acta*. 1065 (2019) 21–28. <https://doi.org/10.1016/j.aca.2019.03.044>.
- [186] F. Tang, C. Guo, J. Chen, X. Zhang, S. Zhang, X. Wang, Cataluminescence-based sensors: principle, instrument and application, *Luminescence*. 30 (2015) 919–939. <https://doi.org/10.1002/bio.2702>.
- [187] Z. Long, H. Ren, Y. Yang, J. Ouyang, N. Na, Recent development and application of cataluminescence-based sensors, *Analytical and Bioanalytical Chemistry*. 408 (2016) 2839–2859. <https://doi.org/10.1007/s00216-015-9210-4>.
- [188] G. Shi, Y. He, Y. Zhang, B. Yin, F. Ali, Detection and determination of harmful gases in confined spaces for the Internet of Things based on cataluminescence sensor, *Sensors and Actuators B: Chemical*. 296 (2019) 126686. <https://doi.org/10.1016/j.snb.2019.126686>.
- [189] H. Tang, Y. Li, C. Zheng, J. Ye, X. Hou, Y. Lv, An ethanol sensor based on cataluminescence on ZnO nanoparticles, *Talanta*. 72 (2007) 1593–1597. <https://doi.org/10.1016/j.talanta.2007.01.035>.
- [190] A. Borgschulte, O. Sambalova, E. Billeter, A. Sterzi, J. Niggli, B. Welte, A. Heel, R. Holzner, Cataluminescence in Er-Substituted Perovskites, *Advanced Science*. 8 (2021) 2101764. <https://doi.org/10.1002/advs.202101764>.

Index of Figures

<i>Fig. 1 Possible classification of chemical sensors. The materials herein presented are semiconductor gas sensors</i>	15
<i>Fig. 2 Both in n-type (a) and p-type (b) semiconductors nanoparticles, the interaction with oxygen brings to a core-shell configuration</i>	21
<i>Fig. 3 Schematic diagram of the basic principle of CTL as modelled by Hu et al., 2019 [143]</i>	25
<i>Fig. 4 The metal oxide nanopowder synthesised: from left to right $ZrO_2:Eu^{3+}$, $ZrO_2:Y^{3+}$, $ZrO_2:Tb^{3+}$ and $ZrO_2:Er^{3+}$</i>	29
<i>Fig. 5 Sensor uncoated: it is possible to observe the gold wires and the interdigitated electrodes (a). The sensor used during the experiments; it was drop-coated with ZrO_2 nanopowder (b).</i>	34
<i>Fig. 6 Schematic representation of the sensors substrate: details of the ceramic substrate and the interdigitated gold electrodes(a), the platinum resistance heater(b), the sensor system (c)</i>	35
<i>Fig. 7 Schematic representation of the temperature-activated sensor system</i>	36
<i>Fig. 8 Diagram of the UV-activated resistance sensor</i>	37
<i>Fig. 9 X-Ray Diffraction (XRD) pattern of the undoped zirconium oxide</i>	39
<i>Fig. 10 XRD pattern of the undoped zirconium oxide and relative phase attribution fitting. The blue trace refers to the experimental data, while the red trace corresponds with the library diffraction pattern.</i>	40
<i>Fig. 11 X-Ray Diffraction (XRD) pattern of the $ZrO_2:Eu^{3+}$ (5%)</i>	40
<i>Fig. 12 XRD pattern of the $ZrO_2:Eu^{3+}$ (5%) and relative tetragonal phase attribution. The blue trace refers to the experimental data, while the red trace corresponds with the library pattern</i>	41
<i>Fig. 13 Transmission Electron Microscopy (TEM) image for ZrO_2</i>	42
<i>Fig. 14 Transmission Electron Microscopy (TEM) images for $ZrO_2:Eu^{3+}$ (5%)</i>	42
<i>Fig. 15 Scanning Electron Microscopy (SEM) images for the ZrO_2 nanoparticles</i>	43
<i>Fig. 16 Scanning Electron Microscopy (SEM) images for $ZrO_2:Eu^{3+}$ (5%) nanoparticles</i>	44
<i>Fig. 17 EDX spectrum for undoped ZrO_2 material. The peak positions for zirconium and oxygen are marked.</i>	45
<i>Fig. 18 EDX spectrum for $ZrO_2:Eu^{3+}$ (5%). The peak positions for zirconium, oxygen, and europium are marked</i>	45
<i>Fig. 19 Raman spectrum of the undoped ZrO_2 nanoparticles (upper trace) and $ZrO_2:Eu^{3+}$ nanoparticles (lower trace).</i>	46
<i>Fig. 20 Photoluminescence and cataluminescence spectra at 450°C: (a) cataluminescence from undoped ZrO_2 for acetone at 2 parts per thousand (ppth). The blue dotted line indicates the calculated form of black body radiation (BBR). (b) cataluminescence from $ZrO_2:Eu^{3+}$ for acetone at 2 ppth and (c) photoluminescence from $ZrO_2:Eu^{3+}$ with 532 nm excitation.</i>	47
<i>Fig. 21 Different dilution levels, starting from acetone's headspace concentration, were registered by selected ion flow tube (SIFT) mass spectrometry</i>	48

<i>Fig. 22 Theoretical acetone concentration as a function of the concentration measured by SIFT-MS when using the glass syringe-dilution method.</i>	49
<i>Fig. 23 Increase of the background (black body radiation) as a function of the temperature</i>	51
<i>Fig. 24 Dual-modality profile for the ZrO₂:Eu³⁺ (5%) at the operating temperature of 300°C, following three subsequent injections of acetone (296 ppm), It is possible to notice the high repeatability of the resistance (black trace) and CTL (red trace) responses. Both responses occur simultaneously (multimodal response) but with different kinetics.</i>	52
<i>Fig. 25 Zirconium oxide resistance response to acetone (296 ppm). Temperature set to 150°C</i>	54
<i>Fig. 26 Zirconium oxide response to acetone, for a concentration of 29.6 ppm and a sensor temperature of 150°C</i>	54
<i>Fig. 27 ZrO₂ response to three injections of acetone (296 ppm). In this case, the operating temperature was set at 300°C</i>	55
<i>Fig. 28 The resistance response showed a great dependence to the temperature. The resistance behaviour as a function of the operating temperature showed that the best sensor performances, in terms of sensitivity, corresponded with 200°C. The graph refers to 296 ppm of acetone.</i>	56
<i>Fig. 29 Temperature dependence of the ZrO₂ response following the interaction with acetone. In this case, the concentration was lower (2.96 ppm).</i>	57
<i>Fig. 30 ZrO₂ response to 58.7 ppm at the different operating temperatures at which the sensor was tested</i> ..	58
<i>Fig. 31 Comparison of the temperature dependence of the sensor response when tested to acetone, ethanol, and water.</i>	59
<i>Fig. 32 Zirconium oxide response to some explosive linked compounds at different operating temperatures. ZrO₂ showed the best response to 2,4-DNT at 180°C</i>	60
<i>Fig. 33 ZrO₂ CTL signal when interacting with 296 ppm of acetone. This volatile was injected three times in the system, leading to the characteristic three peaks that we can observe above</i>	61
<i>Fig. 34 Concentration dependence of the CTL from the zirconium oxide with a linear fit. The signal increases with the concentration rise.</i>	61
<i>Fig. 35 Concentration dependence of the ZrO₂ light emission (acetone) and linear fit. The operating temperature, in this case, was 300°C</i>	62
<i>Fig. 36 Temperature dependence of the CTL response to acetone (296 ppm) for the undoped zirconium oxide. The best sensitivity is achieved in the range 275-300°C</i>	63
<i>Fig. 37 In the case of lower concentrations (2.96 ppm), ZrO₂ showed the best cataluminescent response at 275°C</i>	64
<i>Fig. 38 CTL signal produced by the zirconium oxide sensor when exposed to ethanol (58.7 ppm) as a function of the temperature. The best response was at 250°C</i>	65
<i>Fig. 39 Temperature profile of the light emission response to 2,4-dinitrotoluene (T_{MAX} at 175°C)</i>	66
<i>Fig. 40 Comparison between the CTL response to ethanol (red trace) and 2,4-dinitrotoluene (black trace), as a function of the operating temperature.</i>	67

Fig. 41 Zirconium oxide response to 2,3-Dimethyl-2,3-dinitrobutane (DMNB) at different temperatures. The best performances corresponded to 180°C	67
Fig. 42 ZrO ₂ light emission response to nitroglycerine (NG) at all the temperature tested. The best performances corresponded to 150°C.....	68
Fig. 43 Comparison of the undoped zirconium oxide response to acetone, ethanol and water as a function of the temperature.....	69
Fig. 44 Resistance dependence of acetone concentrations at 300°C. The concentration is reported in a logarithmic scale	70
Fig. 45 ZrO ₂ :Eu ³⁺ resistance following three subsequent injection of acetone (296 ppm, the highest concentration investigated). Operating temperature of 300°C.	71
Fig. 46 Temperature dependence of the resistance response to acetone (29.6 ppm) in the europium-doped zirconium oxide case.	72
Fig. 47 Europium-doped ZrO ₂ resistance response following three consecutive injections of ethanol (58.7 ppm).....	73
Fig. 48 ZrO ₂ :Eu ³⁺ (5%) Resistance response to ethanol (58.7 ppm) at different temperatures.....	73
Fig. 49 Comparison of the resistance response displayed by the europium-doped zirconium oxide sensor at different temperatures	74
Fig. 50 Light emission as a function of the acetone concentration. The substrate temperature was 275°C....	75
Fig. 51 ZrO ₂ :Eu ³⁺ (5%) response to three following injections of acetone (296 ppm) at 300°C. Note the good sensor performances under these conditions: sharp shape of the peak, meaning a good sensor sensitivity, a relatively fast response and recovery time.....	76
Fig. 52 ZrO ₂ :Eu ³⁺ (5%) light emission response to different volatiles at the temperature investigated. This sensor showed the best performances when exposed to acetone, especially at 300°C.....	77
Fig. 53 ZrO ₂ :Eu ³⁺ (5%) light emission response as a function of the operating temperature. In particular to (a) nitroglycerine and (b) 2,3-dimethyl-2,3-dinitrobutane	78
Fig. 54 WO ₃ resistance response to acetone (29.6 ppm) at 350°C	79
Fig. 55 Resistance response showed by the tungsten oxide sensor at different operating temperatures. The graph emphasises the comparatively large response to acetone (black trace in the graph) when compared with ethanol (red trace) and water (blue trace) to which the sensor did not respond	80
Fig. 56 WO ₃ response to 2,3-dimethyl-2,3-dinitrobutane in terms of electrical conductivity. The best response is identifiable at 275°C.....	81
Fig. 57 Light emission produced by WO ₃ when exposed to 296 ppm of acetone (three injections) at 300°C.	82
Fig. 58 Light emission showed by the tungsten oxide sensor at different temperatures.	83
Fig. 59 Concentration dependence of the cataluminescence response in the case of the tungsten oxide sensor at the operating temperature of 350°C.....	84
Fig. 60 Three injections of ethanol (58.7 ppm) at 400°C in the case of the WO ₃ sensor	85

<i>Fig. 61 Resistance signal (Ohms) of the zinc oxide sensor following injections of: TATP (55 ppm), causing an increase in resistance (positive response); acetone (29.6 ppm) which corresponded to a decrease of the resistance (negative response); hydrogen peroxide (20 ppm) which exhibited a positive response.</i>	86
<i>Fig. 62 Resistance response of the ZnO sensor following three injections of TATP (55 ppm) at 250°C.....</i>	87
<i>Fig. 63 Resistance response as a function of the concentration (triacetone triperoxide, sensor temperature = 250°C)</i>	88
<i>Fig. 64 ZnO response to acetone (negative signal); concentration of 296 ppm and operating temperature of 250°C.....</i>	89
<i>Fig. 65 ZnO response to 296 ppm of acetone at the operating temperature of 200°C.....</i>	90
<i>Fig. 66 ZnO responding to three following injections of acetone (296 ppm) at 200°C. The experiment was performed after one month from the one showed in Fig. 64.</i>	91
<i>Fig. 67 Relative resistance response as a function of acetone concentration.</i>	91
<i>Fig. 68 Sensor sensitivity test in the case of the UV-activated ZnO sensor. The device responded to H₂O₂ in the range 2 ppb-2 ppm.....</i>	92
<i>Fig. 69 Selectivity test on the UV-activated ZnO sensor. The data shows that the sensor responded selectively to hydrogen peroxide (2 ppm), and not to acetone, even at 2960 ppm.....</i>	93
<i>Fig. 70 Comparison between the resistance response from ZrO₂, ZrO₂:Eu³⁺ and WO₃ when exposed to different concentrations of acetone (0.296 ppm up to 296 ppm) at the operating temperature of 250°C. The graph emphasises the better performances showed by tungsten oxide if compared with the zirconium-based materials</i>	96
<i>Fig. 71 Resistance response of the ZrO₂ and the ZrO₂:Eu³⁺ sensor as a function of the acetone concentration at 250°C.....</i>	97
<i>Fig. 72 Comparison of the response of ZrO₂, ZrO₂:Eu³⁺(5%) and WO₃ when exposed to ethanol (58.7 ppm) in the temperature range 150-350°C.....</i>	98
<i>Fig. 73 CTL response of the three sensors of ZrO₂, ZrO₂:Eu³⁺(5%) and WO₃ following the interaction with different concentrations of acetone (substrate temperature= 275°C).....</i>	99
<i>Fig. 74 Log of the CTL produced by the zirconium-based sensors when exposed to acetone (concentration on a Log scale, sensor temperature of 275°C)</i>	100
<i>Fig. 75 Dual-modality response (ratio light emission(resistance) of the ZrO₂:Eu³⁺(5%) sensor respectively to acetone (29.6 ppm) and ethanol (58.7 ppm).....</i>	102
<i>Fig. 76 Comparison between the relative resistance response for acetone (2.96 ppm, black trace) and ethanol (5.87 ppm, red trace). At each one of the temperatures reported, the resistance signal of the two compounds is relatively similar.</i>	103
<i>Fig. 77 Resistance response % (a), cataluminescence (b) and ratio CTL/resistance (c) for the ZrO₂ sensor (180°C operating temperature) when exposed to four different explosive compounds: 2,3-dimethyl-2,3-dinitrobutane, 2,4-dinitrotoluene, ethylene glycol dinitrate, and nitroglycerine.</i>	105

